U-Pb Geochronology of Paleosol and Vertebrate Fossil Bone Carbonate Cements by LA-ICP-MS: New Strategies for Dating the Terrestrial Record in Deep Time

By

LUIS ERICK AGUIRRE PALAFOX

DISSERTATION

Submitted in partial satisfaction of the requirements for the degree of

DOCTOR OF PHILOSOPHY

in

Earth and Planetary Sciences

in the

OFFICE OF GRADUATE STUDIES

of the

UNIVERSITY OF CALIFORNIA

DAVIS

Approved:

Isabel P. Montañez, Chair

Noah M. McLean

Kari Cooper

Committee in Charge

2025

Table of Contents

Acknowledgments

First and foremost, I would like to express my profound gratitude to my advisers, Isabel Montañez and Noah McLean. Your solid guidance, expertise, and encouragement have been instrumental in shaping not only this dissertation but also my growth as a scientist. Your patience and dedication have been invaluable throughout this journey, and I am truly fortunate to have had the opportunity to be your PhD student and learn from you.

I am also incredibly grateful to my parents, Carmen and Luis, and their endless love and support that have been the groundwork of my success since I can remember. You are my OG rocks and I cannot thank you enough for being there for me when I needed you the most. To the rest of my family, including Miriam, Patricia, Osmar, Osmar Jr., Rosalva and Osiris, thank you for your encouragement and sincere understanding throughout this journey. Your faith in me has been a constant source of strength that has fueled me through life and also through this PhD.

To my "Rocks", including Scott Carpenter, Tim Duenas, Gene Gorman, Mary Kaiser, Walter Alvarez and Rafael Vazquez—your belief in me, even during the most challenging moments, has kept me grounded and motivated. The making of this dissertation could have not been possible without you in my life and for teaching me invaluable life lessons that have shaped the person I am today.

To my friends, my "Pebbles", including Steven, Fiona, Audrey, Grayson (Kuntur), Irene, Alejandro, Ryan and Hunter, thank you for your unwavering support, for lifting my spirits when I needed it most, and for reminding me to take breaks and enjoy life once in a while during this process. Your companionship and kindness have made this journey so much more enjoyable and tolerable. You kept me mentally sane and brought so much happiness when I needed it.

Lastly, to my amazing and beloved cat, Keroberos—your quiet presence, comforting loud purrs, and occasional interruptions at my keyboard or sleeping on my lap during long nights working at my desk have been a comforting source of inspiration, solace and reason to keep going. Thank you for being my loyal companion through countless late nights, early mornings and many, many, many times I was ready to give up.

This dissertation is as much a product of all your support as it is of my own efforts, and I am eternally grateful to each and every one of you.

Abstract

Dating terrestrial sedimentary successions is often challenging due to limited cosmopolitan species and the scarcity or absence of datable volcanic deposits, hindering our ability to more precisely correlate proxy records among sedimentary successions across all paleo-latitudes. Laser ablation inductively coupled mass spectrometry (LA-ICP-MS) U-Pb geochronology provides a powerful, inexpensive, and fast tool to date previously overlooked materials in the terrestrial record. In this dissertation, I examine the U-Pb systematics and potential for dating of calcite cements precipitated within carbonate nodules in paleosols (fossil soils) from the late Triassic Ischigualasto Fm (Argentina) and the early Permian Eastern Shelf of the Midland Basin (U.S.A), and within bone and fracture porosity in vertebrate fossil bones (Ischigualasto Fm). Based on petrographic analyses and cathodoluminescence imaging, a cement micro-stratigraphy (paragenesis) for each studied sample was developed that guided LA-ICP-MS analysis and age interpretation. The U-Pb isotopic data indicates that syn-depositional and early burial cements approximate the timing of calcite precipitation in the vadose zone and into the shallow phreatic zone, respectively. All U-Pb carbonate ages for the studied samples are in stratigraphic order and agree with higher-precision ages of volcanic deposits intercalated within the succession and regional biostratigraphic constraints. U-Pb carbonate ages from the Eastern Shelf succession suggest that the regional Wolfcampian-Leonardian Boundary (WLB) has an approximate age of 287 Ma and likely lies in the middle to upper Waggoner Ranch Fm, and that another proposed WLB lower in the stratigraphy defines a separate boundary that predates the WLB by ~5 Ma. The 290.8 ± 4.3 Ma for this pre-WLB is still significant as it aligns with global environmental perturbations at the close of the Sakmarian international stage linked with an abrupt rise in paleo-CO_2 that marks the beginning of the demise of the Late Paleozoic Ice Age. The first indirect U-Pb

carbonate ages for vertebrate fossil bones including basal dinosaurs Eoraptor and Herrerasaurus from the Ischigualasto Fm are presented, marking a step towards a more robust interrogation of the origin of the rapid emergence and diversification of early dinosaurs and environmental perturbations in southern Pangea during the Late Triassic.

Introduction

Performing modern integrative geology requires a robust footing in absolute time. Temporal control in the marine record benefits from biostratigraphy constrained by primarily cosmopolitan species and the potential for robust astrochronology, as well as the high preservation of dateable volcanic ashes. In terrestrial depositional settings the situation is typically very different. Limited geographically widespread species and lower preservation potential of volcanic ashes in the terrestrial realm make assembling an age model difficult. This is a monumental setback that hinders our ability to correlate with precision proxy records within and among depositional basins at the local, regional, and global scale, in turn, limiting the interrogation of interactions and feedbacks between paleo-processes during critical periods of our planet's history. To overcome this issue, either new radiometric dating techniques or refined existing approaches must be applied to previously overlooked materials readily found in terrestrial sedimentary successions.

The high throughput of laser ablation inductively coupled plasma mass spectrometry (LA-ICP-MS), its relative low expense, high-spatial resolution, and minimal sample preparation have fueled a revolution in U-Pb geochronology of zircons, and recent advances demonstrate the potential for carbonate dating at ~2%–10% precision (e.g., Roberts et al., 2020; Gulbranson et al., 2022; Montano et al., 2022; Rasbury et al., 2023). Over the past decade, interest in LA-ICP-MS U-Pb carbonate geochronology has grown substantially driven by studies that introduced fast and accurate methods for dating carbonates (e.g., Drost et al., 2018), albeit with lower precision than single zircon ID-TIMS U-Pb dating (Drost et al., 2018; Roberts et al., 2020), access to a well-calibrated series of reference carbonate standards (Guillong et al., 2020; Hill et al., 2016; Nuriel et al., 2021; Roberts et al., 2017) and new field and laboratory strategies that increase the potential for accurate U-Pb carbonate dating of carbonates precipitated within certain environments and

conditions (e.g., lacustrine, pedogenic, vein-fill, speleothem; Roberts et al., 2020; Roberts and Holdsworth, 2020; Montano et al., 2021, 2022; Rasbury et al., 2023; Rochin-Bañaga et al., 2024). However, the accurate interpretation of a given carbonate age must be examined in its geologic and paragenetic context, which requires careful petrographic characterization of the generations of carbonate precipitates prior to U-Pb dating.

In this dissertation, I investigate the potential of LA-ICP-MS U-Pb dating of calcite cements precipitated within carbonate nodules from paleosols in the late Triassic Ischigualasto Fm (northwest Argentina) and the early Permian Eastern Shelf succession of the Midland basin (U.S.A), and within primary bone and fracture porosity in fossil bone samples from the Ischigualasto Fm. In these studies, a cement micro-stratigraphy for each sample guided the LA-ICP-MS U-Pb analyses and further age interpretations. Variations in U-Pb isotopic signatures across different generations of carbonate precipitates demonstrate that specific cements are more adequate for U-Pb dating. Overall, the U-Pb ages from these carbonate precipitates follow a well-defined stratigraphic order and agree with higher precision ages from volcanic deposits (Ischigualasto Fm) or biostratigraphic constraints (Eastern Shelf succession).

In chapter 1, I investigate the U-Pb isotopic signatures obtained by LA-ICP-MS of calcite cements precipitated within primary fractures in carbonate nodules from paleosols in the late Triassic Ischigualasto Fm of northwest Argentina. Based on a cement micro-stratigraphy (paragenesis) for each studied sample, this study demonstrates that ages that approximate pedogenesis and timing of earliest burial can be obtained from syn-pedogenic and earliest generation calcite cements in pedogenic carbonate nodules. The U-Pb carbonate ages are in stratigraphic agreement with published U-Pb zircon and $^{40}Ar/^{39}Ar$ sanidine ages from intercalated volcanic ashes, validating the accuracy and precision of the U-Pb carbonate ages. Finally, I outline

a step-by-step strategy that maximizes the potential for successful U-Pb dating of pedogenic and other syndepositional carbonates from terrestrial successions.

In chapter 2, I applied all the insights and dating strategy from the previous chapter to date carbonate nodules from paleosols in the Eastern Shelf of the Midland Basin (part of the greater Permian Basin region) in Texas, U.S.A. The LA-ICP-MS U-Pb carbonate ages for the carbonate nodules are in stratigraphic order and agree with regional biostratigraphic constraints. Based on the U-Pb carbonate ages and the *S. crassitectoria* biozone, the Wolfcampian-Leonardian Boundary (WLB) in the studied Eastern Shelf succession likely lies within the middle-upper Waggoner Ranch Fm and has an age of 287.1 ± 4.4 Ma (mid-late Artinskian), making it correlative with the extrapolated age of ~286 Ma for the Leonardian-type section from the Glass Mountains of West Texas, thus resolving the long-debate for the stratigraphic position and age of the WLB in the Eastern Shelf succession. A modeled U-Pb age for another proposed WLB in the Eastern Shelf succession indicates that it is a separate stratigraphic boundary that predates the WLB higher in the stratigraphy by ~5 Ma. However, the age for this pre-WLB is significant as it aligns with global environmental perturbations at the close of the Sakmarian international stage that correlate with an abrupt rise in paleo-CO_2 that marked the beginning of the demise of the Late Paleozoic Ice Age.

In Chapter 3, I examine the U-Pb systematics and potential for U-Pb dating of calcite cements precipitated both within the primary porosity of fossil bone and early burial fractures that formed in Dinosauria and Archosauria fossil bones from the Ischigualasto Fm of northwest Argentina. Based on a cement micro-stratigraphy for each sample, the U-Pb ages from these cements are interpreted to estimate the timing of calcite precipitation within the vadose zone before the bone material transitioned into the shallow phreatic zone. I infer that the timing of calcite precipitation is close to the time of death and burial of the specimens due to a lack of evidence for U-Pb open-

system behavior in the analyzed cements and previous calculations for depositional rates in that section of the Ischigualasto Fm. The U-Pb ages for the calcite cements are comparable to existing radioisotopic ages of volcanic deposits and calcite cements precipitated in carbonate nodules from paleosols intercalated within the succession (Chapter 1). This study marks the first successful indirect dating of basal Eoraptor and Herrerasaurus dinosaurs from the Ischigualasto Fm, a key succession for interrogating the origin of the rapid emergence and diversification of early dinosaurs and environmental perturbations in southern Pangea during the Late Triassic.

References Cited:

Guillong, M., Wotzlaw, J.F., Looser, N., and Laurent, O., 2020, Evaluating the reliability of U-Pb laser ablation inductively coupled plasma mass spectrometry (LA-ICP-MS) carbonate geochronology: Matrix issues and a potential calcite validation reference material: Geochronology, v. 2, doi:10.5194/gchron-2-155-2020.

Rasbury, E.T., Piccione, G., Holt, W., and Ward, W.B., 2023, Potential for constraining sequence stratigraphy and cycle stratigraphy with U-Pb dating of carbonates: Earth-Science Reviews, v. 243, doi:10.1016/j.earscirev.2023.104495.

Nuriel, P., Wotzlaw, J.F., Ovtcharova, M., Vaks, A., Stremtan, C., Šala, M., Roberts, N.M.W., and Kylander-Clark, A.R.C., 2021, The use of ASH-15 flowstone as a matrix-matched reference material for laser-ablation U-Pb geochronology of calcite: Geochronology, v. 3, doi:10.5194/gchron-3-35-2021.

Drost, K., Chew, D., Petrus, J.A., Scholze, F., Woodhead, J.D., Schneider, J.W., and Harper, D.A.T., 2018, An Image Mapping Approach to U-Pb LA-ICP-MS Carbonate Dating and Applications to Direct Dating of Carbonate Sedimentation: Geochemistry, Geophysics, Geosystems, v. 19, doi:10.1029/2018GC007850.

Gulbranson, E.L. et al., 2022, U–Pb Geochronology and Stable Isotope Geochemistry of Terrestrial Carbonates, Lower Cretaceous Cedar Mountain Formation, Utah: Implications for Synchronicity of Terrestrial and Marine Carbon Isotope Excursions: Geosciences (Switzerland), v. 12, doi:10.3390/geosciences12090346.

Montano, D., Gasparrini, M., Rohais, S., Albert, R., and Gerdes, A., 2022, Depositional age models in lacustrine systems from zircon and carbonate U-Pb geochronology: Sedimentology, v. 69, doi:10.1111/sed.13000.

Roberts, N.M.W. et al., 2020, Laser ablation inductively coupled plasma mass spectrometry (LA-ICP-MS) U-Pb carbonate geochronology: Strategies, progress, and limitations: Geochronology, v. 2, doi:10.5194/gchron-2-33-2020.

Roberts, N.M.W., Rasbury, E.T., Parrish, R.R., Smith, C.J., Horstwood, M.S.A., and Condon, D.J., 2017, A calcite reference material for LA-ICP-MS U-Pb geochronology: Geochemistry, Geophysics, Geosystems, v. 18, doi:10.1002/2016GC006784.

Hill, C.A., Polyak, V.J., Asmerom, Y., and P. Provencio, P., 2016, Constraints on a Late Cretaceous uplift, denudation, and incision of the Grand Canyon region, southwestern Colorado Plateau, USA, from U-Pb dating of lacustrine limestone: Tectonics, v. 35, doi:10.1002/2016TC004166.

Montano, D., Gasparrini, M., Gerdes, A., Della Porta, G., and Albert, R., 2021, In-situ U-Pb dating of Ries Crater lacustrine carbonates (Miocene, South-West Germany): Implications for continental carbonate chronostratigraphy: Earth and Planetary Science Letters, v. 568, doi:10.1016/j.epsl.2021.117011.

Rochín-Bañaga, H., Davis, D.W., and Moysiuk, J., 2024, U–Pb dating of belemnites and rugose corals: The potential for absolute dating of calcitic invertebrate fossils: Chemical Geology, v. 644, doi:10.1016/j.chemgeo.2023.121862.

Chapter 1: U-Pb geochronology of paleosol carbonate cements by LA-ICP-MS: A proof of concept and strategy for dating the terrestrial record

This chapter is reproduced from the original publication: Aguirre Palafox, L. E., Müller, A., McLean, N. M., Ludvigson, G. A., Colombi, C. E., & Montañez, I. P. (2024). U-Pb geochronology of paleosol carbonate cements by LA-ICP-MS: A proof of concept and strategy for dating the terrestrial record. Geochemistry, Geophysics, Geosystems, 25, e2024GC011488. https://doi.org/10.1029/2024GC011488

Abstract

This study investigates the potential of LA-ICP-MS U-Pb dating for carbonate nodules in the Late Triassic Ischigualasto Formation of northwestern Argentina. We establish a fully characterized paragenetic sequence to guide the analysis of three pedogenic carbonates and compare the U-Pb ages with published geochronology from volcanic ashes within the sedimentary succession. Our findings demonstrate the importance of interpreting U-Pb data within a well-defined paragenetic framework for accurate age interpretation of pedogenic carbonates. We observe variations in U-Pb isotopic signatures across different generations of carbonate precipitates and identify syn-pedogenic and early burial calcite cements as most suitable for precise dating. Respectively, these two calcite cements are interpreted as microcodium and crack-lining calcite cements formed early in the paragenetic sequence during pedogenesis to early burial of the paleosols as they transitioned from the unsaturated vadose to saturated phreatic zone below the water table. The U-Pb ages obtained from the carbonate nodules agree with the radioisotopic ages of volcanic ashes, supporting the validity of our dating strategy. These results contribute to advancing U-Pb carbonate geochronology and highlight its increased potential for dating

sedimentary records in the terrestrial realm. Future research should focus on replicating similar work on different carbonate nodules within the Ischigualasto Fm and expanding the application of LA-ICP-MS U-Pb dating to other carbonate-bearing formations, especially in successions with limited absolute ages or where volcanic ashes are sparse or absent.

1. Introduction

In the terrestrial realm, pedogenic carbonates that precipitated in paleosols (fossil soils) are important archives of past physical, biological, and chemical surface processes (e.g., Ekart et al., 1999; Kraus, 1999; Tabor and Myers, 2015; Gulbranson et al., 2022). Despite the widespread abundance of carbonate-bearing paleosols in the geologic record (Retallack, 1988; Boucot et al., 2013), and their integral role in paleoclimate and environmental reconstructions, obtaining geologically meaningful ages from carbonate-bearing paleosols has proven challenging. Initial dating efforts via isotope dilution (ID) U-Pb carbonate geochronology produced mixed results (e.g., Rasbury et al., 1998, 2000; Rasbury and Cole, 2009). Analogous to dating studies of other terrestrial and marine carbonates, the limited success of ID U-Pb carbonate geochronology can be attributed, in part, to the scarcity of samples with U/Pb and U concentrations adequate for precise dating. In addition, sample sizes (up to tens of mg) required for ID TIMS analysis at the time increased the potential for homogenization of multiple generations of carbonate within a sample or the inclusion of organic or other mineral material present in the sample.

The high throughput of laser ablation inductively coupled plasma mass spectrometry (LA-ICP-MS), its low expense, high-spatial resolution, and minimal sample preparation have driven a revolution in U-Pb geochronology of zircons, and recent advances demonstrate the potential for carbonate dating at ~2-10% precision (e.g., Roberts et al., 2020; Gulbranson et al., 2022; Montano

et al., 2022; Rasbury et al., 2023). Recently, interest in LA-ICP-MS U-Pb carbonate geochronology has grown substantially driven by studies that introduced fast and accurate methods for dating carbonates (e.g., Drost et al., 2018), albeit with lower precision than single zircon ID-TIMS U-Pb dating (Drost et al., 2018; Roberts et al., 2020). Access to a well-calibrated series of reference carbonate standards (Hill et al., 2016; Roberts et al., 2017; Guillong et al., 2020; Nuriel et al., 2021) and new in-field and laboratory strategies increases the potential for robust U-Pb carbonate dating (Guillong et al., 2020; Roberts et al., 2020; Rasbury et al., 2021; 2023; Montano et al., 2021, 2022). The successful application of LA U-Pb carbonate geochronology to constrain the timing of carbonate precipitation and diagenesis in a given stratigraphic succession or sedimentary basin is now well documented (e.g., Li et al., 2014; Godeau et al., 2018; Parrish et al., 2018; Chaldekas et al., 2021; Elisha et al., 2021; Gulbranson et al., 2022; Rembe et al., 2021; Roberts and Holdsworth, 2022; Rasbury et al., 2021). This body of work opens up opportunities for dating the sedimentary record. The next step in advancing the field is considering the U-Pb dates within a detailed paragenetic context (i.e., the sequential order of mineral formation), given the complexity of cement micro-stratigraphy typically found in pedogenic carbonates and other syndepositional and early burial carbonate precipitates.

To date, most studies have focused on applying LA-ICPMS U-Pb carbonate geochronology to dating fracture-filling and intergranular cements for constraining the timing of fluid flow, tectonic events, and reservoir evolution (Pan et al., 2020; Liu et al., 2021; Roberts and Holdsworth, 2022). To our knowledge, there are only two published studies that specifically targeted pedogenic carbonate nodules (Methner et al., 2016; Rochín-Bañaga et al., 2023). The paucity of studies can be attributed to factors that hinder or limit the acquisition of usable U-Pb isotopic data, including

(1) low U and high Pb concentrations typically found in pedogenic and meteoric carbonates, (2) the occurrence of thin (<100 μm) and multiple generations of cements, (3) the presence of micropores and high abundance of detrital material, (5) the overall high susceptibility of carbonates to diagenesis and thus alteration of their isotopic systematics, and (6) calculating ages from assumed synchronous carbonate material. These and other potential factors can result in measured U-Pb ages of paleosol carbonates that are neither accurate nor precise and, thus of limited utility for geochronology. Moreover, the accurate interpretation of a given carbonate age must be examined in its geologic and paragenetic context which requires careful petrographic characterization of the generations of carbonate precipitates prior to U-Pb dating.

In this study, we examine the U-Pb systematics and potential for LA-ICP-MS dating of carbonate nodules using cement micro-stratigraphy as a framework for guiding the LA-ICP-MS U-Pb analysis of three pedogenic carbonates collected from intervals in the Late Triassic Ischigualasto Formation of northwestern Argentina that permit comparison to published zircon and sanidine geochronology from volcanic ashes intercalated with the carbonate nodule-bearing succession (Rogers et al., 1993; Martínez et al., 2011; Colombi et al., 2021). We document the importance of interpreting U-Pb data using a fully characterized paragenetic sequence to identify cements most suitable for U-Pb dating and their accurate age interpretation. We show that U-Pb isotopic signatures vary across the analyzed generations of carbonate precipitates, and that syn-pedogenic and early burial calcite cements within these nodules display U-Pb ratios and U concentrations most adequate for precise dating. We interpret the U-Pb ages from these cements to approximate, within the uncertainty of the U-Pb ages, the timing of nodule formation in the vadose zone and their initial transition from the vadose into the phreatic zone. As a proof of

concept, the U-Pb dates for the carbonate nodules we present here are comparable to the existing radioisotopic ages of the volcanic ashes intercalated with the carbonate nodule-bearing succession.

2. Geologic Setting and Sample Selection

The Late Triassic Ischigualasto Fm of northwestern Argentina is a paleosol and vertebrate-rich succession deposited in a continental rift basin (Figure 1). The Ischigualasto Fm consists of 400 to 700 m of laminated to thinly bedded mudstones and siltstones intercalated with fine- to coarse-grained stratified sandstones and conglomerates (Figure 2), interpreted as floodplain and fluvial channel-filling deposits, respectively, as well as intercalated volcanic ashes and basaltic dykes (Currie et al., 2009; Colombi et al., 2017). Carbonate-bearing paleosols (calcic Vertisols, calcic Argillisols, and Calcisols; Tabor et al., 2006) are developed in the lower half of succession along the basin axis, and throughout basin margin successions. Given the high fossil preservation potential, abundance and diversity of tetrapod fossils, including mammal-like cynodonts and the earliest dinosaurs in the Ischigualasto Fm, as well as paleofloral assemblages (macro and microflora), this succession has been the target of many studies (e.g., Artabe et al., 2001; Césari and Colombi, 2013; Colombi et al., 2017), including studies interrogating the origin of the rapid emergence and diversification of early dinosaurs and environmental perturbations in southern Pangea during the Late Triassic (e.g., Rogers et al., 1993; Martínez et al., 2011, 2012; Desojo et al., 2020; Colombi et al., 2021; Mancuso et al., 2022).

For this study, two nodules from a basin axis section (ISCH-107 and ISCH-288) and one from the western margin of the basin axis (ISCH-251) were selected from a collection of pedogenic nodules provided by C. Colombi. These nodules were selected based on their stratigraphic position and proximity to published zircon U-Pb and sanidine and plagioclase $^{40}Ar/^{39}Ar$ ages from

intercalated volcanic ashes (Figure 2). Sanidine and plagioclase $^{40}Ar/^{39}Ar$ ages from Martínez et al. (2011) and Rogers et al. (1993) were recalibrated by Martínez et al. (2011) to the ^{40}K decay constant determined by Renne et al. (2010). The nodules from the basin axis section (Figure 2) are bracketed by (1) the "Herr Toba" bentonite 20 m above the base of the Ischigualasto Fm (Figure 2) with a recalibrated $^{40}Ar/^{39}Ar$ sanidine plateau age of 231.4 ± 0.3 Ma (±2σ; Rogers et al., 1993; Martínez et al., 2011), (2) a dated tuff deposit 310 m above the base of the Ischigualasto Fm with a CA-TIMS U-Pb zircon age of 228.91 ± 0.14 Ma (±2σ; Colombi et al., 2021) and (3) the "Jach Toba" bentonite 630 m above the base of the Ischigualasto Fm with a recalibrated $^{40}Ar/^{39}Ar$ plagioclase age of 225.9 ± 0.9 Ma (±2σ; Martínez et al., 2011). The margin section is correlated to the main basin axis section using a normalized thickness between these two sections considering boundaries between members as basinwide guidelines (Currie et al., 2009).

3. Materials and Methods

3.1 Carbonate Petrography

Polished and uncovered thick sections (~250 μm thick) for each sample were stained using Alizarin Red and Potassium Ferricyanide solution (Dickson, 1965) and studied petrographically using plane-polarized light and by cathodoluminescence (CL). For each sample, a cement stratigraphy was developed based on observed calcite textures and fabrics, cross-cutting relationships, and CL banding.

CL images were collected at the Kansas Geological Survey Digital Cathodoluminescence Imaging Laboratory, using a Relion Industries Reliotron III cold cathode chamber. Operating conditions included a rarified Helium atmosphere at 50 milliTorr, with an accelerating voltage of

10 kilovolts and beam current of 1.0 milliamp. The CL chamber and 16 Mpx Peltier-cooled Olympus DP73 microscope camera were mounted on a modified Olympus BX41 microscope.

3.2 U-Pb carbonate geochronology

In situ U-Pb analyses of three polished thick sections were carried out using a Photon Machines Analyte G2 193 nm ArF excimer laser ablation system connected to a Thermo Scientific Element2 ICPMS. Analyses were performed using circular 85 μm diameter laser spots ablated with the laser at 3.0 J/cm^2 fluency and a 10 Hz repetition rate for 30 seconds and carried to the ICPMS in helium gas with a 1.1 l/min combined flow rate. To ensure proper laser spot selection, targeted areas of interest in each nodule were observed using the laser's built-in camera in transmitted and reflected light and cross-referenced with their respective established micro-stratigraphies. Downhole fractionation, Pb isotopic fractionation and drift, and uncertainty propagation were corrected by bracketing measurements of unknowns with NIST 612 glass reference material (Jochum et al., 2011) using the Iolite software (Paton et al., 2011). U-Pb fractionation was corrected and analytical scatter propagated into the isotopic ratios using an in-house Excel spreadsheet (based on the spreadsheet of Kylander-Clark, pers. comm. 2020). The carbonate reference material DBTL (Hill et al., 2016) was used to calibrate U-Pb ratios, and WC-1 (Roberts et al., 2017) was used for validation of the U-Pb fractionation.

The software package IsoplotR (Vermeesch, 2018) was used to visualize U–Pb data and calculate initial ^{234}U and ^{230}Th-disequilibrium corrected LA-ICPMS U-Pb dates. A conservative initial ^{234}U/^{238}U of 2 ±2 value was used based on the average of activity ratios from a compilation of shallow-groundwater studies (e.g., Roberts et al., 2020). An initial ^{230}Th/^{238}U of 0 was used due to Th being highly insoluble in natural aqueous systems. All LA-ICP-MS U-Pb carbonate date

uncertainties are reported at ±2σ and expressed in the format X/Y/Z, where X incorporates analytical uncertainties only, Y additionally includes the uncertainty in the age of the primary reference material (here, DBTL; Hill et al., 2016), and Z includes our ±2% external reproducibility.

4. Results

4.1 Carbonate Paragenesis

The three studied nodules consist of a matrix of calcite micrite (microcrystalline < 10 um), with minor amounts of detrital quartz, feldspar, and Fe and Mn oxides. The nodules exhibit circumgranular cracks, vascular plant root casts, and fractures. Petrographic relationships, cathodoluminescence, and carbonate staining document three generations of calcite cements that partially to fully occlude void and fracture porosity. The distribution of cement generations varies within and among the three samples.

Generation 1 calcite cements (Gen 1): Gen 1 cements are present only in nodule ISCH-251 as two morphologies. Gen 1A occurs as inclusion-rich fibrous to thinly bladed calcite (50 to 150 μm in length) crystals that irregularly to evenly rim the external walls of primary voids, which are fully to partially filled with organic-rich microcrystalline calcite (Figure 3a), as well as cements radiating off micritic clots (Figure 3b). Inclusion-rich layers within Gen 1A define zonation observed in plane-polarized light. Gen 1B occurs as granular calcite crystals that are subrounded to equant and are concentrated in clusters within primary porosity (Figure 3b). Less commonly, Gen 1 cements occur as clear equant calcite crystals (90 to 120 μm in length) that rim clasts of brecciated Gen 1A cement (Figure 3b) or line primary voids. Overall, Gen 1 is non-ferroan (pink/red staining) and displays nonluminescence to zoned dull luminescence.

Interpretation: Sample ISCH-251 is interpreted to have formed in a palustrine deposit that experienced prolonged periods of pedogenic modification, when carbonate nodules formed, based on field and thin section observations. The elongated strand and clotted morphology of much of the carbonate micrite in this sample is interpreted to be microbially mediated by cyanobacteria biofilms and or algae (Alonso-Zarza and Wright, 2010). Gen 1 cements in nodule ISCH-251 formed as active soil processes. We interpret Gen 1A as microcodium associated with root casts based on their association with the inferred microbially precipitated micrite and their occurrence as cements radiating off the external walls of primary voids that are partially to fully occluded with organic-rich microcrystalline calcite (Figure 3a). Based on cross-cutting relationships, Gen 1B granular calcite cements likely formed as precipitates within primary voids soon after precipitation of microcodium and in syn-pedogenetic fractures analogous to pseudomicrokarst observed in palustrine limestones (Plaziat and Freytet 1978). This is the earliest generation of cement coating clasts and lining voids. Where subrounded clusters of Gen 1B cements occur likely reflects physical erosion and/or corrosion of the cements by freshwaters, possibly during intermittent (seasonal?) flooding of the palustrine deposits.

Generation 2 calcite cements (Gen 2; Figure 4): Gen 2 calcite cements occur primarily in the ISCH-107 and ISCH-288 nodules as the first generation of cement in primary void and fracture porosity. These cements occur as clear to inclusion-rich equant to prismatic crystals (40 to 100 μm in length) that irregularly to isopachously line syndepositional circumgranular cracks and root casts as well as early compaction fractures (Figure 4a, 4b and 4f). Gen 2 cements are pink-staining (non-ferroan). Zonation characterized by alternating inclusion-rich (honey-colored) to clear calcite, dissolution surfaces, detrital and authigenic Fe-oxides and staining define three distinctive layers (Gen 2A-C; Figure 4). Gen 2A is laterally discontinuous and has uneven thickness, with

crystal terminations defining linear to irregular surfaces (Figures 4b and 4d). Minor amounts of very fine-grained (< 10 μm) detrital and/or authigenic Fe-oxides overlie Gen 2A surfaces (Figure 4d). Gen 2A exhibits homogenous dully orange luminescence (Figure 4c). Gen 2B is similar in crystal morphology to and overgrows Gen 2A cements. Scalenohedral terminations are well-developed in places, whereas they exhibit irregular surfaces elsewhere (Figures 4a, 4d and 4e). In Gen 2B cements, minor amounts of fine-grained detrital and/or authigenic Fe-oxides overlie this cement (Figures 4d and 4e). Gen 2B cements exhibit alternating non-luminescent (clear calcite) and uniformly dull orange (honey-colored, inclusion-rich calcite) luminescence (Figures 4c). The third layer, Gen 2C occurs as prismatic crystals with well-developed scalenohedral terminations (Figures 4d and 4e). These crystals are zoned in plane-polarized light with an outermost honey-colored zone (Figure 4e) and exhibit thin alternating zonation of dull and bright luminescence (Figure 4c). Detrital and authigenic Fe-oxides occur both as inclusions within the terminal parts of Gen 2C (Figures 4a and 4b) and as coating surfaces of the cement, in places as microbotryoids (up to 250 μm) with micron-size needles of Fe-oxide precipitates (Figure 4a). In some primary void and fracture porosity Gen 2C is the first crack-lining cement.

Interpretation: Overall, Gen 2 cements are interpreted to have formed early in the paragenetic sequence during pedogenesis to early burial of the paleosols as they transitioned from the unsaturated vadose to the saturated phreatic zone below the water table. This interpretation of Gen 2 cements as archiving the transition from vadose to phreatic conditions is based on the following characteristics and inferred conditions: (1) the presence of honey-colored inclusion-rich bands in Gen 2A and B cements interpreted to be soil-sourced organics; (2) the irregular distribution and flat terminations of calcite crystals of Gen 2A suggesting formation in partially fluid-filled porosity (i.e., growth to the meniscus in vadose conditions); (3) irregular surfaces on Gen 2A and 2B

cements interpreted as dissolution surfaces between periods of cement precipitation in the chemically dynamic vadose environment; (4) the presence of Fe-staining and detrital and authigenic Fe-oxides on the surfaces of Gen 2A, B, and C cements indicate oxidizing environments and infiltration of soil materials into non-water saturated porosity; and (5) for Gen 2C cements, the well-developed scalenohedral crystal terminations that indicate growth into a water-saturated pore coupled with thin alternating zonation of dull and bright luminescence, which is interpreted to record fluctuating Eh conditions (Barnaby and Rimstidt, 1989), indicates precipitation proximal to the vadose-phreatic transition (see Discussion).

Generation 3 calcite cements (Gen 3): Gen 3 cements occur in ISCH 107, 251 and 288 as clear blocky calcite spar (100 to 500 μm in length) that fills remaining porosity (Figures 4a, 4b, 4e and 4f). These cements are slightly ferroan (mauve/light purple-staining; Figures 4b and 4f) and exhibit uniformly orange to brown dull luminescence with less common dull zonation (Figure 4c).

Interpretation: Gen 3 is interpreted to have precipitated in the deeper phreatic zone with burial given its occurrence as the final cement occluding remaining porosity, its elevated ferroan composition and dull luminescence.

4.2 U-Pb Carbonate Geochronology

U-Pb LA-ICP-MS data and ages of representative calcite cement generations from the three carbonate nodules are presented in Figure 5, Table 1, and Supporting Information. This data is also available at Geochron.org via https://www.geochron.org/dataset/html/geochron_dataset_2024_01_11_XZkeX

ISCH-107 was collected from a Calcisol 107 m above the base of the Ischigualasto Fm in the Cancha de Bochas Member (Figure 2). The isochron fit to all U-Pb data, including the carbonate micrite, Gen 2 cements and mixed spots that ablated both of these carbonate precipitates (n = 98), shows scatter well outside analytical uncertainties (MSWD = 6.3; Figure 5a). Analyses of carbonate micrite and Gen 2 cements only (n=58) have a U-Pb date of ca. 239 Ma (MSWD = 7.1; Figure 5b). U-Pb dates of ca. 251 Ma (MSWD = 2.6) and 230.5 ± 2.2/3.2/5.6 Ma (MSWD = 1.1) are obtained by only plotting carbonate micrite (n=31; Figure 5c) and Gen 2 cements data (n=27; Figure 5d), respectively. For the Gen 2 cements, the uranium concentration and spread in $^{238}U/^{206}Pb$ range from 0.5 to 40 ppm by mass and 1 to 27, respectively.

The second basin axis sample ISCH-288 was collected from a compound paleosol in the Valle de la Luna Member 288 m above the base of the Ischigualasto Fm. Based on U-Pb data (n=20) from Gen 2 cements, this nodule has a calculated U-Pb date of 229.4 ± 3.4/4.1/6.2 Ma (MSWD = 1.0, n=20; Figure 5e), and its uranium concentration and spread in $^{238}U/^{206}Pb$ range from 80 to 120 ppm by mass and 23 to 27, respectively. However, the initial $^{207}Pb/^{206}Pb$ (0.324 ± 0.005) of ISCH-288 from Gen 2 cements is significantly lower than values documented in terrestrial carbonates (Roberts et al., 2020). Instead, we favor a date of 233.6 ± 3.9/4.5/6.5 Ma, calculated from a best fit line to the four most radiogenic analyses from large cracks anchored to a geologically reasonable $^{207}Pb/^{206}Pb$ of 0.84 ± 0.05 (Figure 5g; see Section 5.3.2). This value for the initial $^{207}Pb/^{206}Pb$ also matches those calculated from ISCH-107 and ISCH-251 (Table 1; Figure 5d, 5f). Similar to the ISCH-107 U-Pb dataset, adding micrite and/or analyses from mixed carbonate precipitates results in excess scatter about best-fit U-Pb isochrons and meaningless dates (Figure S1c to S1E).

The third carbonate nodule, ISCH-251, was collected from a calcic Argillisol in the basin margin section correlated to a stratigraphic position equivalent to 359 m above the base of the Ischigualasto Fm in the basin axis section (Figure 2). ISCH-251 has a calculated U-Pb date of 228.4 ± 5.0/5.5/7.1 Ma based on Gen 1A cements data (MSWD = 1.7, n=30; Figure 5f), and its uranium concentration and spread in $^{238}U/^{206}Pb$ range from 0.6 to 7 ppm by mass and 0.8 to 13, respectively. Best-fit U-Pb isochrons of other carbonate precipitates in ISCH-251 result in meaningless dates (Figures S1f to S1j).

5. Discussion

We successfully determined U-Pb carbonate ages from the studied samples. In this section, we document the distinctive isotopic signatures and U-Pb ratios of the carbonate micrite, syn-pedogenic (Gen 1) cements in ISCH-251, and syn-pedogenic to early burial cements (Gen 2) in ISCH-107 and ISCH-288 nodules that determine their potential for U-Pb carbonate dating.

5.1 Carbonate Micrite

The carbonate micrite matrix in all samples has a moderate spread in $^{238}U/^{206}Pb$ (Figure 6), although most data cluster around ~9, and a higher isotopic scatter on T-W plots than the other analyzed carbonate precipitates (Figures 5a to 5d). The micron-scale heterogeneity of the carbonate micrite, observed best under cathodoluminescence (CL), may contribute to the observed isotopic scatter. Similar CL patterns in carbonate nodules have been documented by others and suggest the juxtaposition of carbonate crystals with different diagenetically resistant domains (e.g., Ludvigson et al., 2010; Ross et al., 2017). The 85 μm laser spot diameter used in this study did not

permit analysis of individual components of the micrite. As seen in CL and plane-polarized light, the higher abundance of detrital material (e.g., oxides and clays) within the carbonate micrite further increases the potential for mixing of these materials of different geochemical compositions.

Moreover, petrographic analysis following LA-ICP-MS analysis documents that some spot analyses sampled a mixture of different carbonate precipitates (e.g., carbonate micrite and Gen 2 cement) despite the careful positioning of laser spots via the built-in laser chamber camera. Cement bands thinner than 85 μm and the complex three-dimensional distribution of cements in cracks contributed to the inadvertent sampling of different carbonate precipitates. The U-Pb isotopic data of these "mixed spots" slightly deviate from the isotopic signatures of spots that solely analyzed the intended carbonate generation. On T-W plots, these "mixed generation" analyses contribute to scatter around the best-fit line exceeding analytical uncertainties, and therefore to dates with lower precision, and to higher MSWD values (Figure 5a). This highlights the importance of petrographic evaluation after LA-ICP-MS analysis in addition to pre-ablation screening to (1) accurately link isotopic signatures to intended targeted material, and (2) to avoid inclusion of isotopic data that represent mixtures of different generations of calcite or include detrital materials into the age calculations.

5.2 Syn-pedogenic Cements

U-Pb isotopic signatures of syn-pedogenic Gen 1A cements show promise for U-Pb dating of carbonate nodules. The isotopic data of Gen 1 cements in the palustrine sample ISCH-251 show moderate spread in $^{238}U/^{206}Pb$, clustering between 1 to 10, and U concentrations ranging from 0.9 to 7 ppm by mass (Figure 6). Whereas these U concentrations are low, they are still favorable for

U-Pb dating and slightly higher than the average of ~1 ppm reported from terrestrial carbonates (Roberts et al., 2020). Based on U-Pb data (Figure 6) and petrographic observations, the higher U concentrations in Gen 1A cements are due to the sampling of microcodium. Although the exact process of microcodium formation (rhizogenic vs. non-rhizogenic) remains equivocal, this calcitic microfeature is associated with biologically mediated processes in terrestrial surface environments (e.g., Freytet & Plaziat, 1982; Jaillard et al., 1991; Alonso-Zarza et al., 1998; Kosir, 2004; Kabanov et al., 2008; Kayğılı et al., 2019). Gen 1A cements in sample ISCH-251 are interpreted to have precipitated around root casts, preserved as voids partially to fully occluded by organic-rich microcrystalline calcite (cf. Kabanov et al., 2008). In modern soils, higher U concentrations are documented in plant roots and in soil solution surrounding the roots (e.g., Stojanović et al., 2010; Tandy et al., 2013). In ancient analogs, organic-rich material in rhizoliths and other sedimentary deposits (e.g., black shales) is strongly associated with higher U concentrations (e.g., Gauthier-Lafaye et al., 1989; Rasbury et al., 1997; Kelly et al., 2006; Cuney, 2010; Cumberland et al., 2016). The U concentrations suitable for dating of Gen 1A cements are likely attributable to their close association with organic-rich microcrystalline calcite. This, coupled with a moderate spread in $^{238}U/^{206}Pb$, makes Gen 1A cements promising targets for U-Pb dating.

Gen 1B cements are less suitable for U-Pb dating due to a higher isotopic scatter on T-W plots. Although Gen 1B cements have a range in $^{238}U/^{206}Pb$ similar to Gen 1A cements, the U-Pb date from these cements (ca. 245 Ma; Figure S1i) has a higher MSWD of 2.8 and is 15 Ma older than both Gen 1A (228.4 ± 5.0/5.5/7.1 Ma) and the 310 m dated tuff (228.91 ± 0.14 Ma), therefore meaningless in a geologic context. The association of Gen 1B cements with calcite precipitates that formed within fractures, due to pseudomicrokarst formation within the nodules, explains the

complicated relationship of the $^{238}U/^{206}Pb$ as Gen 1B cements were subjected to periods of physical erosion and corrosion by freshwaters, and thus do not represent closed systems.

5.3 Syn-pedogenic to Early Burial Cements

Gen 2 cements in the evaluated carbonate nodules are the most suitable for U-Pb dating. In general, these cements are the most radiogenic, have a larger spread in $^{238}U/^{206}Pb$, and have higher U concentrations compared to carbonate micrite and Gen 1 cements (Figure 6). Gen 2 cements in the ISCH-107 and ISCH-288 nodules line circumgranular cracks that are pedogenic and occur in early compaction fractures. Coupled with their crystal morphology and CL characteristics, this constrains their formation to syn-pedogenic to earliest burial of the soil profile, specifically during their transition from vadose to phreatic conditions. Gen 2 cements display irregular thicknesses, sharp planar terminations of crystals in some cement layers, and evidence of dissolution surfaces on Gen 2A and 2B cements. These features, along with Fe-oxide staining, and the presence of detrital and authigenic oxides between Gen 2 A—B cements constrain the timing of initial precipitation of Gen 2 cements to the unsaturated vadose zone. Under these conditions, cement precipitation is limited by the fluid-air meniscus and infiltration of unsaturated soil waters and detrital influx occur. The common occurrence of scalenohedral terminations of Gen 2C cements, however, along with the more isopachous distribution of these cements and their lack of corrosion indicates the bulk of Gen 2C cements precipitated in water-saturated conditions. We hypothesize that the transition from the vadose to shallow phreatic zone is archived in the Gen 2B and 2C cements.

5.3.1 Eh Control on Uranium Incorporation in Gen 2 Cements

For the successful U-Pb dating of pedogenic carbonate, it is critical to understand the most suitable geochemical conditions that favor the incorporation of uranium. The behavior of uranium in solution is primarily controlled by its oxidation state and in turn the Eh (redox potential) and pH of the system. Our understanding of uranium mobilization and stability in natural, and often complex, aqueous environments is complicated, however, by the affinity of uranium to hydrolyze and form complexes and solids with available ions such as CO_3^{2-}, Ca^{2+}, Mg^{2+}, Na^{+} and PO_4^{3-}, and some organic ligands. The formation and behavior of these uranium complexes determine uranium solubility, sorption, and competition with other ions for complexation with uranium and colloid formation (Burns and Finch, 2018).

Redox-sensitive elements such as Fe and Mn are common in soil and groundwater systems. In calcite, Mn and Fe are incorporated into the crystal lattice only in their reduced Mn^{2+} and Fe^{2+} states. Thus, the cathodoluminescence of calcite cements can be a powerful tool in determining the redox potential of the pore fluids from which they precipitated. The incorporation of Mn^{2+} into the calcite lattice stimulates luminescence, whereas Fe^{2+} reduces or quenches luminescence. At circumneutral pH typical of near-surface freshwaters of the vadose and shallow phreatic zones, reduction of Mn^{4+} to Mn^{2+} occurs at higher Eh values (~ 0.4 mV) as compared to those for the reduction of Fe^{3+} to Fe^{2+} (~ 0.1 mV; Figure 7). Thus, calcite cements that form in oxidizing conditions (Eh > 0.4 mV) lack Fe^{2+} and Mn^{2+} and are nonluminescent. Theoretically, bright orange luminescence in calcite cements should develop under slightly reducing conditions (Eh ranging from 0.4 to ~ 0.1 mV) as Mn^{4+} is reduced to Mn^{2+} before the reduction of Fe^{3+} to Fe^{2+}. At lower Eh conditions (Eh < 0.1 mV), dull luminescence develops as iron (Fe^{3+}) is increasingly reduced to Fe^{2+} that in turn is incorporated into the precipitating calcite. For Gen 2 cements, the observed thin

(<20 μm) oscillating zonation between nonluminescence to bright or dull luminescence is interpreted to record fluctuating Eh conditions during their precipitation proximal to the water table (Figure 7). In this environment, minor shifts (~0.1 mV) in Eh greatly impact the availability and concentration of Mn^{2+} and Fe^{2+}, leading to a narrow range of Eh values that record a dynamic change in CL (Barnaby and Rimstidt, 1998). The formation of Gen 2C cements proximal to the vadose-phreatic boundary constrains the timing of diagenesis of Gen 2 cements (see Section 5.5).

As presented above, Gen 2A and 2B cements are interpreted to have formed in the chemically dynamic environments of the water-unsaturated vadose to saturated shallow phreatic zones. Therefore, we posit that the enrichment of U in Gen 2A and 2B cements occurred as incorporation of stable uranyl-carbonate and uranyl-carbonate-calcium complexes into the calcite lattice as the soil profile transitioned from oxidizing to increasingly reducing conditions as it underwent burial in the phreatic zone. The Eh of soils typically has a complex distribution given soil spatial heterogeneity and the hydrologic regimes operating at different timescales (e.g., Liptzin et al., 2011). This leads to localized 'hot spots' of biogeochemical cycling (McClain et al., 2003) and physiochemical gradients that govern the transport or immobilization of chemical species. In the case of U, U(VI) in the form of the UO_2^{2+} (Uranyl) cation is the most soluble and stable U oxidation state in solution in oxic and aerated environments, whereas U(IV) dominates in reducing conditions and is considerably less soluble. However, few studies have addressed the oxidation state of U in natural calcites. Two carbonate studies by Kelly et al. (2003, 2006) provide an analogue for the Gen 2 cements documented in this study. These studies document incorporation of the U(VI) in the form of the uranyl cation complexes in the crystal lattice of a speleothem calcite and in a calcrete that formed proximal to an oscillating groundwater table. The formation of UO_2-CO_3-Ca complexes under reducing conditions is highly resistant to bioreduction and they are

readily adsorbed to calcite surfaces (Brooks et al., 2003; Rihs et al., 2004). Although other studies document greater uptake of U(IV) in calcite than of U(VI), these studies involve reducing hydrothermal environments and deep anoxic groundwaters (Drake et al., 2018; Gabitov et al., 2021). Notably, U(IV) incorporation into the calcite lattice occurs as a direct substitution for the Ca cation in reducing environments (Sturchio et al., 1998; Gulbranson et al., 2022) and at higher temperatures (~60 to 125 °C) than those expected in soil environments. Thus, we disfavor U(IV) incorporation into Gen 2 cements under its low temperature conditions. Additionally, the organic inclusions in Gen 2A and 2B cements, observed as honey-colored inclusion-rich bands, could be another source for U-enrichment in these cements.

5.3.2 $^{207}Pb/^{206}Pb$ of ISCH-288

Gen 2 cements in ISCH-288 (Figure 5e) are dominated by radiogenic U-Pb isotopic compositions, but there is a smaller range of U/Pb, higher U concentrations (> 80 ppm), and different U-Pb systematics compared to the Gen 2 cements of ISCH-107. A best-fit isochron through this dataset provides a date of 229.4 ± 3.4/4.1/6.2 Ma for ISCH-288 (Figure 5e) that agrees with established zircon and sanidine ages from intercalated volcanic ashes (Rogers et al., 1993; Martínez et al., 2011; Colombi et al., 2021). However, its initial $^{207}Pb/^{206}Pb$ ratio of 0.324 ± 0.005 (Figure 5e) is significantly lower than values documented in a compilation of fracture fill (~0.5) and diagenetic carbonate (~0.6) samples (Roberts et al., 2020). Additionally, a best-fit line calculated by anchoring all ISCH-288 Gen 2 U-Pb analyses to an initial $^{207}Pb/^{206}Pb$ of 0.84 that matches those of ISCH-107 and ISCH-251 leads to an older date (ca. 240.4 ± 2.0 Ma) inconsistent with the volcanic ash ages. One possible explanation for the low y-intercept $^{207}Pb/^{206}Pb$ of the Gen 2 cements in ISCH-288 is that it reflects the true initial common Pb isotopic composition. An

MSWD of 1.0 for the unanchored fit through all Gen 2 analyses is consistent with this hypothesis, and more radiogenic Pbc values (< 0.75) have been attributed to leaching of unsupported radiogenic lead from U-bearing minerals (Roberts et al., 2020).

The unusual apparent initial $^{207}Pb/^{206}Pb$ could be attributed to open-system behavior, specifically systematic leaching of uranium from Gen 2 cements. In this case, the plotted U-Pb analyses progressively shift towards the left on the Tera-Wasserburg concordia plot. Therefore, we favor an intercept age of 233.6 ± 3.9/4.5/6.5 Ma, calculated from a best-fit line to the four most radiogenic analyses from large cracks anchored to a $^{207}Pb/^{206}Pb$ of 0.84 ± 0.05, to represent a better age estimate for the precipitation of Gen 2 cements (Figure 5g). By using our most concordant analyses, we attempt to minimize the effect of potential open-system processes. Whereas this carbonate age is older than expected for the Ischigualasto Fm., the age still agrees within its uncertainty with the "Herr Toba" bentonite and is still in correct stratigraphic order with the 310 m ash (Figure 2).

5.4 Late Cements

U-Pb isotopic signatures of late Gen 3 cements are the least suitable for U-Pb dating of carbonate nodules. These cements have the narrowest spread in $^{238}U/^{206}Pb$ (Figure 6), and also the lowest U concentrations. Gen 3 cements are the least radiogenic leading to a well-constrained Pbc value but a large uncertainty on the lower concordia intercepts in the T-W plot (Figure S1j).

5.5 Accuracy and Precision of the Proposed U-Pb Paleosol Dating Strategy

The U-Pb carbonate ages from the three studied samples are within age uncertainties of published single zircon U-Pb and sanidine and plagioclase $^{40}Ar/^{39}Ar$ ages from intercalated volcanic ashes (±2σ; Rogers et al., 1993; Martínez et al., 2011; Colombi et al., 2021; Figure 2). A carbonate age of 230.5 ± 2.2/3.2/5.6 Ma for ISCH-107 is chronologically consistent and bracketed by (1) the "Herr Toba" bentonite 20 m above the Peña conglomerate (Figure 2) with a recalibrated $^{40}Ar/^{39}Ar$ sanidine age of 231.4 ± 0.3 Ma (Rogers et al., 1993; Martínez et al., 2011), and (2) a recently dated tuff deposit ~ 310 m above the base of the Ischigualasto Fm (Figure 2) with a CA-TIMS U-Pb zircon age of 228.91 ± 0.14 Ma (Colombi et al., 2021). ISCH-107 is located ~87 m above "Herr Toba," whereas ISCH-288 is ~12 m below the dated tuff (at 310 m, Figure 2). Despite an age of 233.6 ± 3.9/4.5/6.5 Ma for ISCH-288 (see Section 5.3.2), this age is within its uncertainty in agreement with the "Herr Toba" bentonite and still in correct stratigraphic order with the ~ 310 m dated tuff. The U-P age of 228.4 ± 5.0/5.5/7.1 Ma for ISCH-251 is within the age uncertainty of sample ISCH-288 and bracketed by the (1) tuff deposit at 310 m (Colombi et al., 2021), and (2) the "Jach Toba" bentonite at 630 m (Figure 2) with a recalibrated $^{40}Ar/^{39}Ar$ plagioclase age of 225.9 ± 0.9 Ma (±2σ; Martínez et al., 2011). ISCH-251 is ~49 m above the dated tuff at 310 m. The obtained U-Pb carbonate ages on Gen 2 cements are thus consistent with volcanic ash deposition and their interpretation as dating syn-pedogenic and early diagenetic processes.

5.5.1 Carbonate Micrite

The results of this study indicate that carbonate micrite in pedogenic nodules should be avoided as a dating target due to a tighter spread in U/Pb (Figure 6) and higher scatter in U-Pb isotopic signatures that lead to inaccurate and imprecise dates (Figure 5c). This is even more critical without

thorough petrographic analysis linking U-Pb signatures to the ablated material or for successions without established age radiometric constraints (e.g., U-Pb zircon, Ar/Ar sanidine). In a recent study, Rochin-Bañaga et al. (2023) analyzed the "massive matrices" of carbonate nodules from a single paleosol and five pedogenic nodule conglomerates using line-scan analysis with a length of 4-5 mm and a laser spot diameter of 150 µm. The U-Pb isotopic data was regressed via Bayesian statistics utilizing the Ultichron software (Davis and Rochín-Bañaga, 2021), resulting in hundreds of measurements per sample, which aimed to maximize the spread in $^{238}U/^{206}Pb$. Upon visualization of these measurements on T-W concordia plots, a significant vertical scatter in $^{207}Pb/^{206}Pb$ ratios was observed. However, due to the large number of analyses in a linear array, best-fit isochrons can still be fitted through these measurements, leading to low MSWD values and reasonable U-Pb carbonate dates. The study presented here, however, demonstrates that carbonate micrite results (Figure 5c and Figures S1c and S1g) yield dates inconsistent with established chronostratigraphy. This is even more pronounced when plotting carbonate micrite with other calcite cement generations. Additionally, it is important to note that whereas the accuracy and precision of the carbonate ages reported in Rochin-Bañaga et al. (2023) agree within uncertainties with a single zircon age obtained from an ash-fall deposit via CA-ID-TIMS, only one carbonate nodule came from a paleosol. The remaining carbonate nodule ages reported were derived from detrital nodules within a conglomerate, two of which were calculated as weighted means. Given the age uncertainty of current U-Pb carbonate geochronology via LA-ICP-MS (typically 1-3%, e.g., Roberts et al., 2020), and the lack of additional higher-precision age constraints to bracket the dates of these detrital nodules, the accuracy and precision of targeting carbonate matrix material should be further explored. Moreover, without careful petrographic studies, plotting carbonate

micrite along with other carbonate precipitates like thin early calcite cements, such as those lining cracks (Gen 2), can further lead to inaccurate dates with low precision as seen in Figure 5b.

5.5.2 Syn-pedogenic Cements

The U-Pb age of 228.4 ± 5.0/5.5/7.1 Ma for Gen 1A cements, determined from U-Pb measurements of microcodium, in nodule ISCH-251 is interpreted to record the timing of pedogenesis (i.e., soil development) in a palustrine environment, because microcodium forms during the early stages of pedogenesis (e.g., Martin-Chivelet and Gimenez, 1992). Additionally, the brecciation of Gen 1A cements (Figure 3b) is interpreted to have occurred during desiccation and/or by the activity of soil organisms and plant roots during subaerial exposure. Furthermore, although palustrine carbonates can form within a season, they typically develop over 10s to 1000s of years (Platt and Wright, 1991; Alonso-Zarza, 2003).

5.5.3 Syn-pedogenic to Early Burial Cements

This study documents that U-Pb dating of syn-pedogenic to early burial cements (Gen 2) provides insightful geochronological constraints for carbonate nodule formation. It is important to note that these ages should be considered minimum age estimates for the precipitation of Gen 2 cements. Estimates for the length of carbonate nodule formation in soils range between 1000 to 10,000 years in arid to semi-arid conditions (Gile et al., 1981; Deutz et al. 2001; 2002), although studies have suggested precipitation within a decade (Zamanian et al., 2016; Li et al., 2018). During carbonate nodule formation, circumgranular cracks develop by desiccation and progressive pedogenic carbonate growth (Wright and Tucker, 1991). Gen 2A and B cements, lining primary

porosity such as circumgranular cracks, are interpreted to have initially precipitated in the vadose zone. Petrographic evidence, however, indicates that precipitation of Gen 2 cements continued through early burial of the soil profile into the shallow phreatic zone. We constrain the timing of burial of soil profiles in the Ischigualasto Fm through the vadose-to-phreatic transition to ~10s to 100s of kyr. This estimate was derived using the average depth (0.1 to 2 m) to the zone of carbonate nodule accumulation in soils (Retallack 2005, 2009), estimates of the depth (0.25 to 2 m) to the groundwater table in unconfined aquifers (Fan et al., 2013; Jasechko et al., 2020), including an estimated depth of the paleo-groundwater table for the Ischigualasto Basin during deposition (Tabor et al., 2006), and a long-term accumulation rate of 10 cm/kyr estimated using stratigraphic thickness between radioisotopically dated horizons. The 10s to 100s of kyr estimate aligns with other estimates of burial rates of paleosols (1 kyr to 10s of kyrs; Deutz et al., 2001; Rusakov et al., 2019; Layzell et al., 2023). Collectively, the inferred duration of nodule formation, burial through the vadose to shallow phreatic zone and precipitation of Gen 2 cements, is well within the uncertainties of the U-Pb carbonate ages obtained in this study.

5.6 Protocol for U-Pb Carbonate Nodule Dating

The U-Pb dating strategy for pedogenic carbonate nodules presented here lies on establishing accurate paragenetic frameworks through petrographic study prior to analysis by LA-ICP-MS. Whereas recent studies have pointed out the need for careful characterization of carbonates in other geologic settings (e.g., lacustrine; Montano et al., 2021, 2022), no protocol has targeted pedogenic carbonates. Therefore, we propose the following protocol for U-Pb dating of pedogenic carbonates:

1) Sample selection: To minimize the probability of diagenetic overprint, carbonate nodules from paleosols in successions with known or suspected shallow burial histories should be prioritized and then backed up with robust paragenetic frameworks to assess the degree of diagenesis. In the field, carbonate nodules smaller than 25 mm in diameter should be avoided since small nodules could have less developed and fewer cracks. Since cracks and crack-lining cements might not be obvious without first cutting the nodule, a minimum of 10 nodules per targeted paleosol horizon should be collected.

2) Petrographic screening: Polished thick (~200 μm) sections of each carbonate nodule should be made to characterize syn-pedogenic and diagenetic precipitates in each sample and to develop a thorough paragenetic framework. This should include staining of the thick sections by established methods (Dickson 1965) and cathodoluminescence petrography to ensure a robust paragenetic framework and to identify and avoid post depositional cement generations with ages that are likely outside the uncertainties of U-Pb ages for syn-pedogenic and early diagenetic cements, and to avoid the influence of diagenetic overprinting.

3) LA-ICP-MS analysis: In general, a laser spot diameter of 85 μm is sufficient to measure U-Pb isotopic signatures from most porosity lining cements. However, if the cements are thicker, a larger laser spot size is recommended if possible to integrate more ablated material and reduce counting statistic uncertainties. In a sample with both syn-pedogenic and early diagenetic cements, the latter should have higher priority as our results indicate that these cements have a higher potential for successful U-Pb carbonate dating. However, if possible, we encourage the dating of both syn-pedogenic and early diagenetic cements within the same sample to maximize the dating success rate of the sample.

4) Petrography post-LA-ICP-MS analysis: Examination of the ablation pits following analysis is recommended to ensure the accurate ablation of the intended carbonates. This is particularly important when using a small laser spot (< 100 μm) on samples with thin cements because mixing of different carbonate cement generations can contribute to isotopic scatter, dates with lower precision, and higher MSWD values on T-W plots.

5) Lastly, this approach lends itself to be used as a high-spatial-resolution screening tool, identifying small but well-characterized, dateable volumes of cements, which can then possibly be micro-sampled and dated by higher-precision techniques (e.g., ID-TIMS).

6. Conclusions

U-Pb isotopic data obtained by LA-ICPMS in this study demonstrate that ages that approximate pedogenesis and timing of earliest burial can be obtained from syn-pedogenic and earliest generation calcite cements in pedogenic carbonate nodules. This study further demonstrates that LA-ICPMS age dating carried out within a well-characterized paragenetic framework provides a more robust strategy to interpret chronological information from the terrestrial stratigraphic record. In turn, this permits age constraints on proxy and paleontological records developed from the same U-Pb carbonate dated successions. In this study, we validate the accuracy and precision of a proposed dating strategy for pedogenic carbonate nodules by developing U-Pb ages for three samples from the Ischigualasto Fm, Argentina. We demonstrate that the carbonate ages are in stratigraphic agreement with published U-Pb zircon and $^{40}Ar/^{39}Ar$ sanidine ages from intercalated volcanic ashes. For the Ischigualasto Fm, the combination of new LA-ICPMS U-Pb carbonate ages and published ID-TIMS dates fills the gaps between zircon and

sanidine dates. The proposed dating strategy, including the development of a robust paragenetic framework, provides a pathway to streamline paleosol dating efforts in the future as it identifies carbonate precipitates most suitable for U-Pb carbonate geochronology, and ensures the avoidance of younger cements and diagenetic overprinting prior to LA-ICP-MS analysis. The proposed dating strategy also maximizes the potential for successful U-Pb dating of pedogenic and other syndepositional carbonates from terrestrial successions, including those for which datable volcanic deposits are sparse or absent.

Acknowledgments

This study was funded by U.S. National Science Foundation awards EAR- 1729882 to IPM.

Open Research

The LA-ICPMS U-Pb data used for concordia plots and $^{238}U/^{206}Pb$ vs U concentration plot in the study are available at Geocrhon via https://www.geochron.org/dataset/html/geochron_dataset_2024_01_11_XZkeX

Figures and Table:

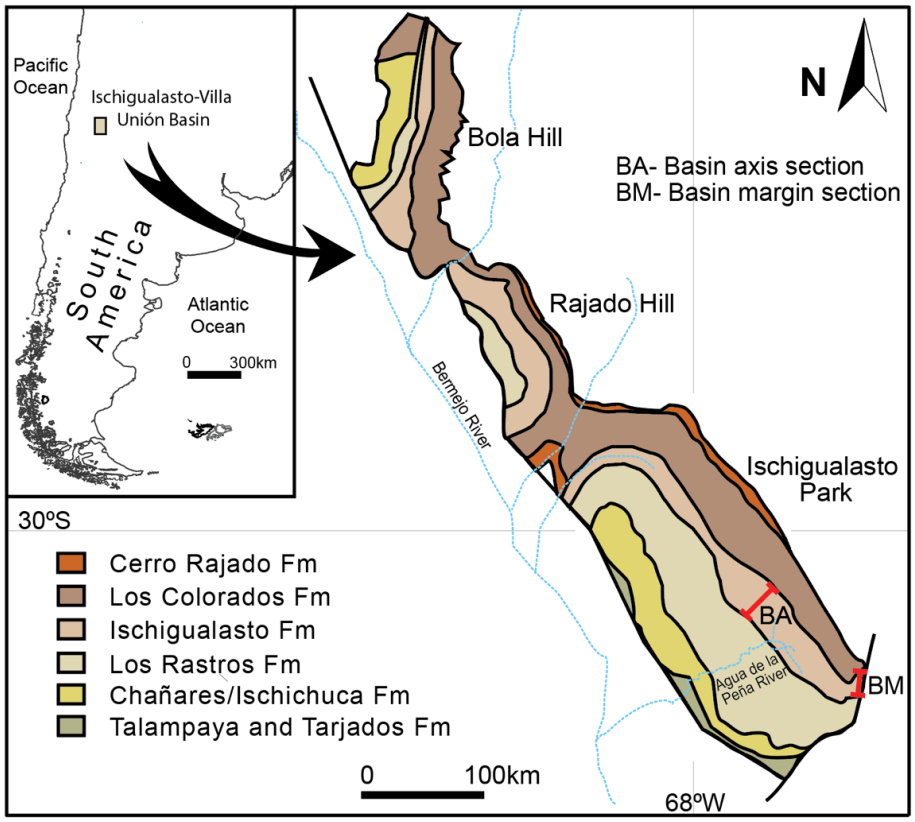

Figure 1. Location and geologic map of the Ischigualasto-Villa Unión Basin, Argentina. Permian (Talampaya, Tarjados), Triassic (Chañeres/Ischichuca, Lost Rastros, and Ischigualasto Fms.) through Jurassic (Los Colorados Fm.) stratigraphy indicated by colors, with the Late Triassic Ischigualasto Fm. in tan. Red lines indicate the locations of outcrop sections (BA=basin axis; BM=basin margin). Figure adapted from Colombi et al. (2021).

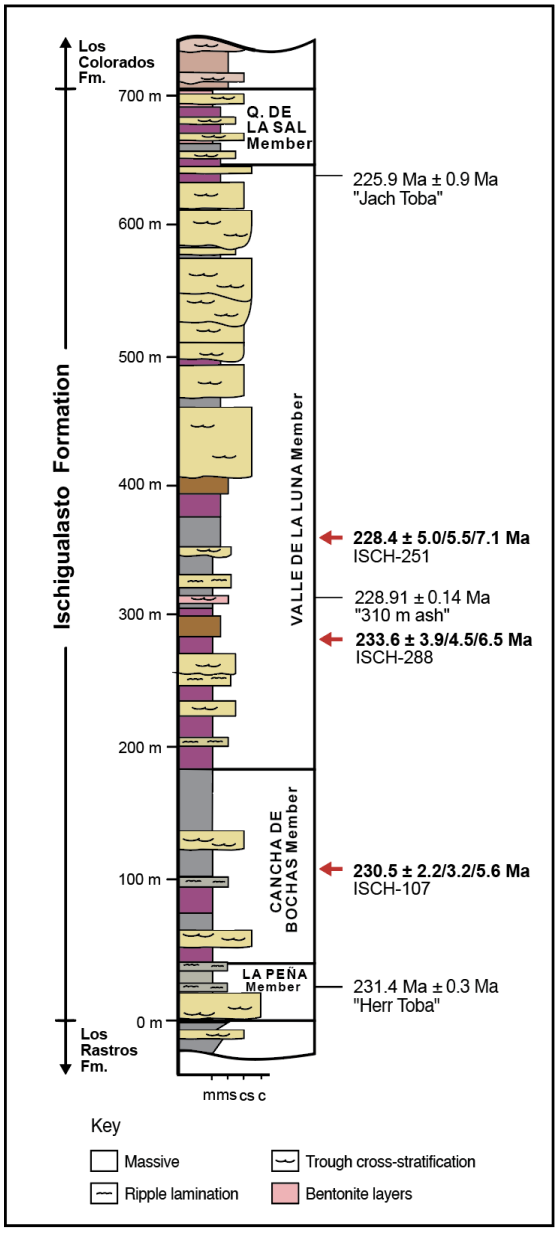

Figure 2. Generalized stratigraphy for the basin axis region of the Ischigualasto Fm modified after Colombi et al. 2021. Stratigraphic position of published zircon U-Pb and sanidine and plagioclase $^{40}Ar/^{39}Ar$ ages from intercalated volcanic ashes shown by black lines (Rogers et al., 1993; Martínez et al., 2011; Colombi et al., 2021) and of the U-Pb carbonate ages of earliest generation calcite cements in the ISCH-251, ISCH-107 and ISCH-288 carbonate nodules shown by red arrows; (this

study). Colors in the stratigraphic column represent similar colors of rocks as seen in outcrop. Uncertainties on all ages are ± 2σ.

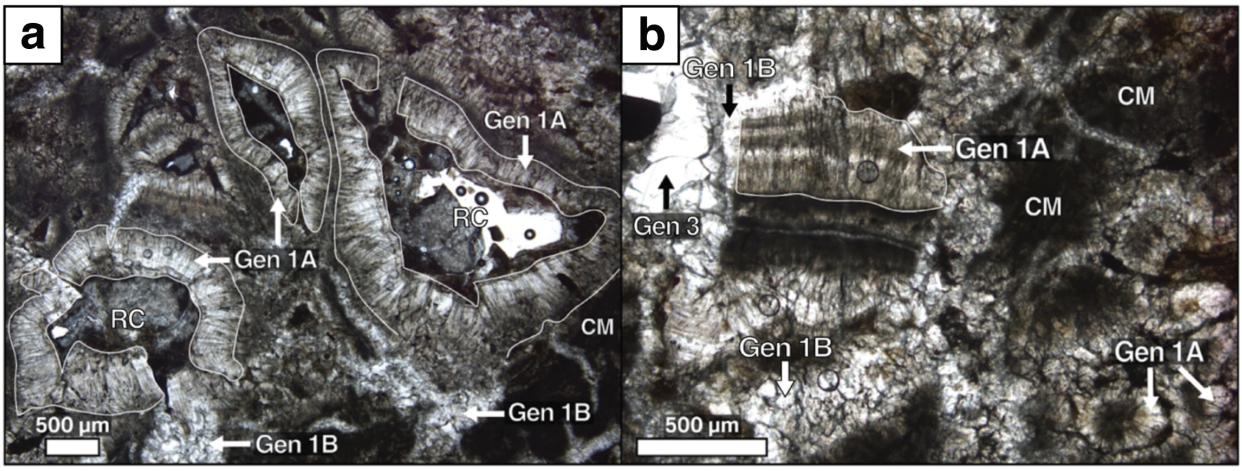

Figure 3. Photomicrographs of Generation 1 calcite cements developed in a carbonate nodule from a palustrine deposit (ISCH-251), PPL view. (A) Calcite cements interpreted as syn-pedogenetic microcodium growing externally off inferred root casts that are partially to fully occluded with organic-rich microcrystalline calcite (Gen 1A) and associated granular calcite cements (Gen 1B; bottom of the photomicrograph). (B) Clast of brecciated Gen 1A cements (white arrow in upper part of image) overgrown by subrounded to equant calcite cement (Gen 1B; left side of image); clear blocky calcite spar (Gen 3) occludes remaining porosity. Note fibrous Gen 1A cements radiating off a micritic clot in the lower right-hand side of the image (vertical arrow). CM- Carbonate micrite. RC- Root cast. Visible laser ablation pits are 85 µm in diameter.

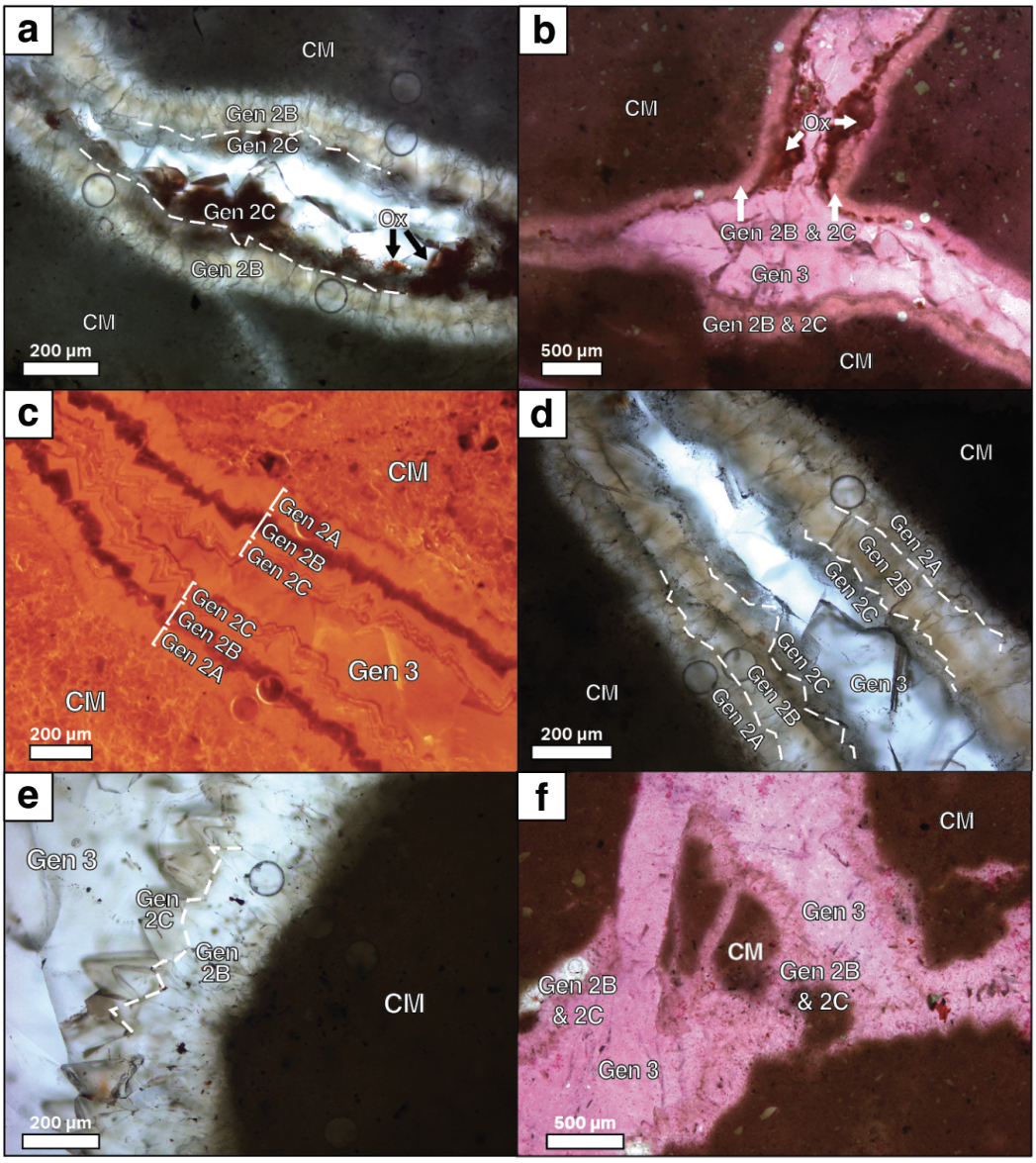

Figure 4. Photomicrographs of Generation 2 and 3 calcite cements developed in pedogenic carbonate nodules (ISCH-107 and ISCH-288). Gen 2 cements are interpreted to have formed early during pedogenesis to early burial of the paleosols into the saturated zone below the water table, while Gen 3 cements are interpreted to have precipitated in the deeper phreatic zone during further burial. (a) A syndepositional to early compaction crack in ISCH-107 lined by Gen 2B and 2C calcite cements, minor episodes of Fe-oxide staining, and a later generation of microbially

mediated iron oxide precipitates (ox); clear blocky spar (Gen 3) occludes remaining porosity, PPL view. (b) Stained ISCH-107 sample showing the discontinuous thickness of non-ferroan (pink) Gen 2 cements and slightly ferroan (mauve/light purple) Gen 3 cements. Oxides and the bottom of laser pits remain unstained. PPL view. (c and d) Paired CL (c) and PPL (d) images of a primary void in nodule ISCH-107. Gen 2 cements can be further divided into three distinctive growth/generations, with Gen 2A displaying orange luminescence, Gen 2B nonluminescence to dull luminescence and Gen 2C defined by alternating dull red to orange luminescence zones. (e) PPL view of Gen 2 cements exhibiting Fe-oxide inclusions (Gen 2B) and well-developed scalenohedral terminations in ISCH-288. (f) Brecciation of syn-pedogenic to early burial, pink-stained Gen 2B and 2C cements before the infill of remaining porosity by late mauve-stained Gen 3 cements in ISCH-288, PPL view. CM- Carbonate micrite. Visible laser ablation pits are all 85 μm in diameter.

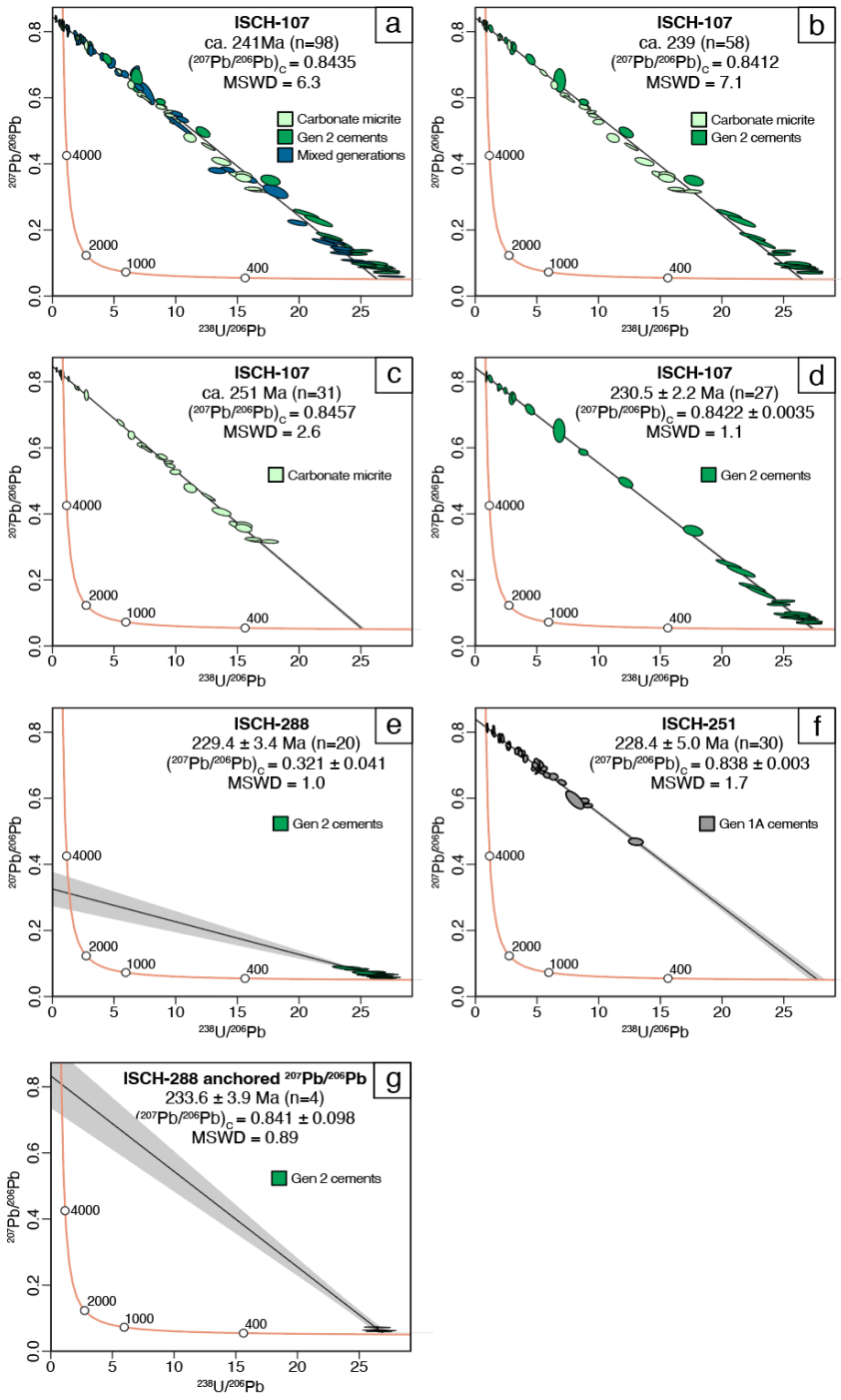

Figure 5. Tera-Wasserburg concordia plots of analyzed carbonate precipitates in the studied pedogenic carbonate nodules. (a) Plotted U-Pb data from carbonate micrite, Gen 2 crack-lining cements, and laser ablation analyses that sampled mixed generations (e.g., Gen 2 and Gen 3, or

Gen 2 and carbonate micrite) in ISCH-107. (b) Plotted U-Pb data from carbonate micrite and Gen 2 in ISCH-107. (c) Plotted U-Pb data from carbonate micrite in ISCH-107. (d) Plotted U-Pb data from Gen 2 crack-lining cements in ISCH-107. (e) Plotted U-Pb data from Gen 2 crack-lining cements in ISCH-288. (f) Plotted U-Pb data from Gen 1A syn-pedogenic cements (microcodium) in ISCH-251. (g) Preferred age for Gen 2 cements in ISCH-288 with an anchored initial $^{207}Pb/^{206}Pb$.

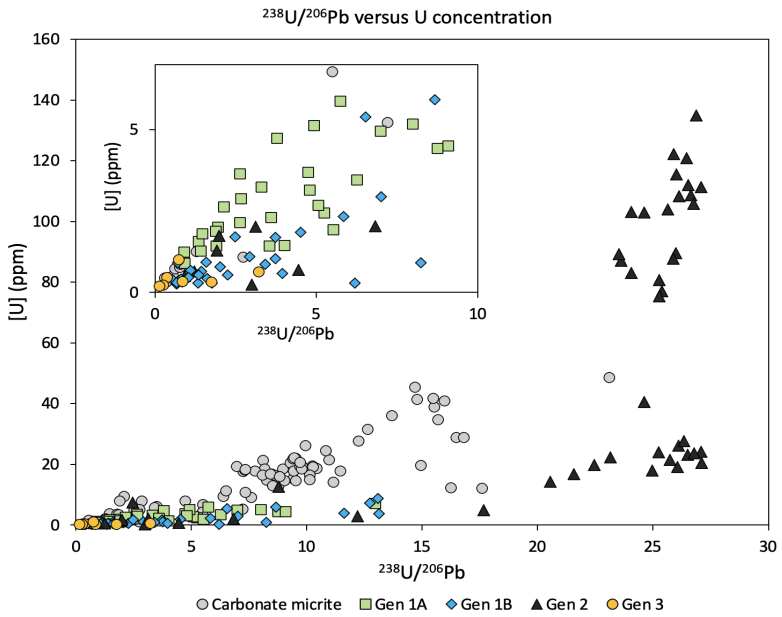

Figure 6. Compilation of U concentration versus $^{238}U/^{206}Pb$ of representative carbonate micrite and Gen 1, Gen 2 and Gen 3 calcite cements in all studied nodules. The carbonate micrite analyses (light gray circles) have moderate U concentrations (up to 44 ppm by mass) but a spread in $^{238}U/^{206}Pb$ of 7 to 20, with most of the analyses clustering ~9. Gen 1A syn-pedogenic cements (green squares) have lower U concentrations (0.9 to 13 ppm by mass) and a moderate spread in $^{238}U/^{206}Pb$ of 1 to 9. Gen 1B cements (blue diamonds) have similar U concentrations and range of $^{238}U/^{206}Pb$ to Gen 1A cements. Gen 2 cements (black triangles) have the widest range in $^{238}U/^{206}Pb$ and define two clusters, ranging from $^{238}U/^{206}Pb$ = 1 to 7 and $^{238}U/^{206}Pb$ = 23 to 27, respectively. The higher $^{238}U/^{206}Pb$ cluster of Gen 2 analyses also has the highest U concentrations of the analyzed carbonate precipitates. Gen 3 cements (yellow circles) have the narrowest range in $^{238}U/^{206}Pb$ (< 4 ppm) and the lowest U concentrations.

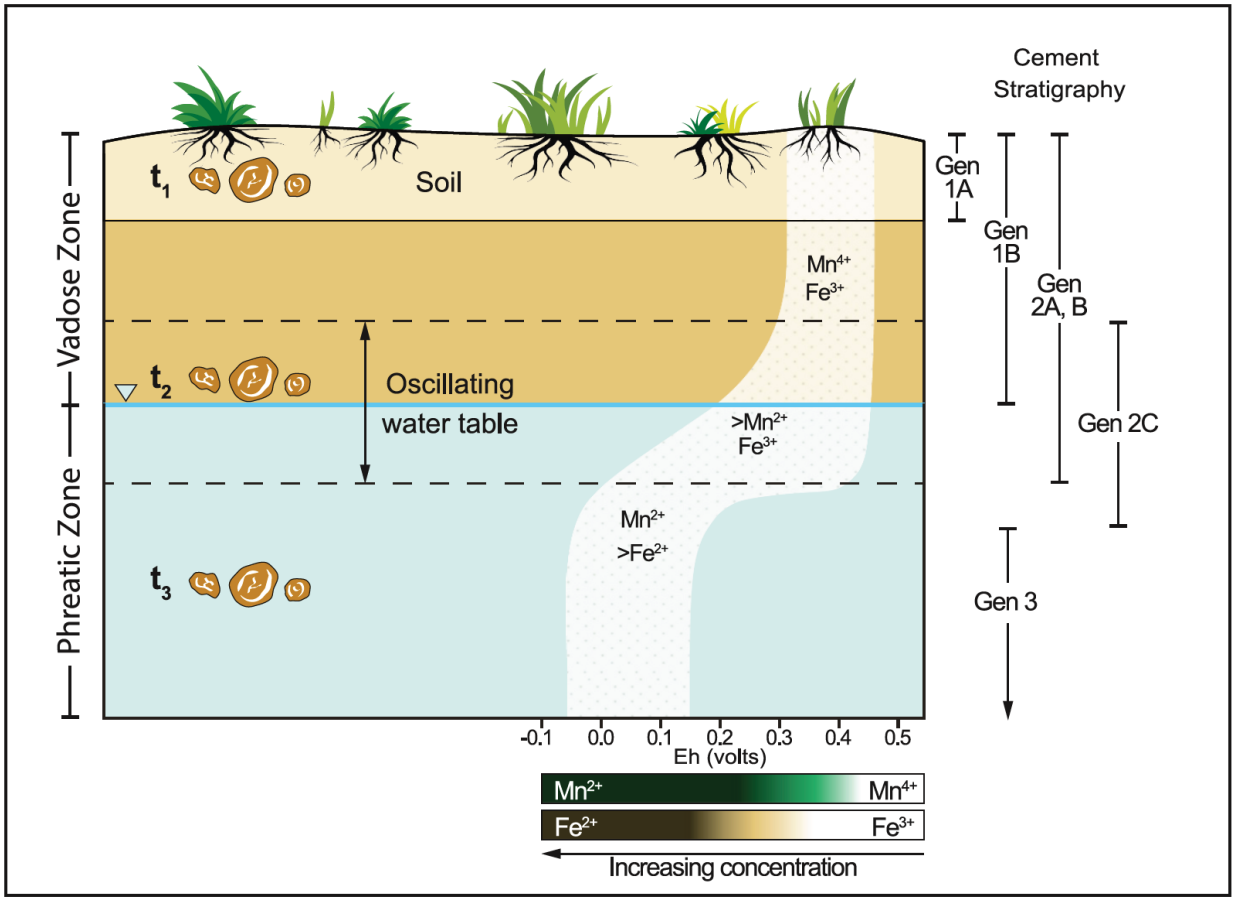

Figure 7. Schematic of a vadose zone paleosol with carbonate nodules undergoing burial across the water table (blue line) into the phreatic zone; dashed lines indicate oscillation of the groundwater table. Stippled region illustrates the evolving Eh conditions (from Edmunds et al., 1987) and Mn and Fe speciation (adapted from Barnaby and Rimstidt 1989) with burial from oxic conditions of the vadose zone to increasingly reducing conditions with burial deeper in the phreatic zone. t_1, carbonate nodules with circumgranular cracks developed due to desiccation and rooting. t_2, initial burial of soil profile from the vadose zone to phreatic zone, formation of early compaction cracks, and incorporation of uranium in Gen 2 cements. t_3, precipitation of Generation 3 cements with continued burial; no constraints on the maximum timing of Gen 3 cements are available.

Table 1. LA-ICP-MS U-Pb data and ages of carbonate nodules from the Ischigualasto Formation.

Sample name	Stratigraphic level (m)	Sample Coordinates	Average U (ppm)	Average Pb (ppm)	Age (Ma)	MSWD	$^{207}Pb/^{206}Pb$ (Pbc)
ISCH-107	107	S 30.06584°, W 67.93979°	14	1.2	230.5 ± 2.2	1.1	0.8422 ± 0.0035
ISCH-288	288	S 30.06584°, W 67.93979°	101	0.4	233.6 ± 3.9	0.89	0.841 ± 0.098
ISCH-251	359	S 30.14422°, W 67.82758°	3	2.7	228.4 ± 5.0	1.7	0.838 ± 0.003

References Cited:

Alonso-Zarza, A.M., and Wright, V.P., 2010, Chapter 2 Palustrine Carbonates: Developments in Sedimentology, v. 61, p. 103–131, doi:10.1016/S0070-4571(09)06102-0.

Alonso-Zarza, A.M., 2003, Palaeoenvironmental significance of palustrine carbonates and calcretes in the geological record: Earth-Science Reviews, v. 60, doi:10.1016/S0012-8252(02)00106-X.

Alonso-Zarza, A.M., Sanz, M.E., Calvo, J.P., and Estévez, P., 1998, Calcified root cells in Miocene pedogenic carbonates of the Madrid Basin: Evidence for the origin of Microcodium b: Sedimentary Geology, v. 116, doi:10.1016/S0037-0738(97)00077-8.

Artabe, A., Morel, E., Spalletti, L., 2001. Paleoecología de las floras triasicas argentinas. In: Artabe, A.E., Morel, E.M., Zamuner, A.B. (Eds.), El Sistema Triasico en la Argentina. Fundacion Museo de La Plata 'Francisco Pascasio Moreno' La Plata, pp. 199–225.

Barnaby, R.J., and Rimstidt, J.D., 1989, Redox conditions of calcite cementation interpreted from Mn and Fe contents of authigenic calcites: Geological Society of America Bulletin, v. 101, doi:10.1130/0016-7606(1989)101<0795:RCOCCI>2.3.CO;2.

Boucot, A.J., Xu, C., and Scotese, C.R., 2013, Phanerozoic paleoclimate: An atlas of lithologic indicators of climate: v. 11.

Brooks, S.C., Fredrickson, J.K., Carroll, S.L., Kennedy, D.W., Zachara, J.M., Plymale, A.E., Kelly, S.D., Kemner, K.M., and Fendorf, S., 2003, Inhibition of bacterial U(VI) reduction by calcium: Environmental Science and Technology, v. 37, doi:10.1021/es0210042.

César, S.N., and Colombi, C.E., 2013, A new Late Triasssic phytogeographical scenario in westernmost Gondwana: Nature Communications, v. 4, doi:10.1038/ncomms2917.

Chaldekas, O., Vaks, A., Haviv, I., Gerdes, A., and Albert, R., 2022, U-Pb speleothem geochronology reveals a major 6 Ma uplift phase along the western margin of Dead Sea Transform: Bulletin of the Geological Society of America, v. 134, doi:10.1130/B36051.1.

Colombi, C., Martínez, R.N., César, S.N., Alcober, O., Limarino, C.O., and Montañez, I., 2021, A high-precision U–Pb zircon age constraints the timing of the faunistic and palynofloristic events of the Carnian Ischigualasto Formation, San Juan, Argentina: Journal of South American Earth Sciences, v. 111, doi:10.1016/j.jsames.2021.103433.

Cumberland, S.A., Douglas, G., Grice, K., and Moreau, J.W., 2016, Uranium mobility in organic matter-rich sediments: A review of geological and geochemical processes: Earth-Science Reviews, v. 159, doi:10.1016/j.earscirev.2016.05.010.

Cuney, M., 2010, Evolution of uranium fractionation processes through time: Driving the secular variation of uranium deposit types: Economic Geology, v. 105, doi:10.2113/gsecongeo.105.3.553.

Currie, B.S., Colombi, C.E., Tabor, N.J., Shipman, T.C., and Montañez, I.P., 2009, Stratigraphy and architecture of the Upper Triassic Ischigualasto Formation, Ischigualasto Provincial Park, San Juan, Argentina: Journal of South American Earth Sciences, v. 27, doi:10.1016/j.jsames.2008.10.004.

Davis, D.W., and Rochín-Bañaga, H., 2021, A new Bayesian approach toward improved regression of low-count U–Pb geochronology data generated by LA-ICPMS: Chemical Geology, v. 582, doi:10.1016/j.chemgeo.2021.120454.

Deutz, P., Montañez, I.P., Monger, H.C., and Morrison, J., 2001, Morphology and isotope heterogeneity of Late Quaternary pedogenic carbonates: Implications for paleosol carbonates as paleoenvironmental proxies: Palaeogeography, Palaeoclimatology, Palaeoecology, v. 166, doi:10.1016/S0031-0182(00)00214-5.

Deutz, P., Montanez, I.P., and Monger, H.C., 2002, Morphology and stable and radiogenic isotope composition of pedogenic carbonates in late quaternary relict soils, New Mexico, U.S.A.: An integrated record of pedogenic overprinting: Journal of Sedimentary Research, v. 72, doi:10.1306/040102720809.

Dickson, J.A.D., 1965, A Modified staining technique for carbonates in thin section [7]: Nature, v. 205, doi:10.1038/205587a0.

Drake, H., Mathurin, F.A., Zack, T., Schäfer, T., Roberts, N.M.W., Whitehouse, M., Karlsson, A., Broman, C., and Åström, M.E., 2018, Incorporation of Metals into Calcite in a Deep Anoxic Granite Aquifer: Environmental Science and Technology, v. 52, doi:10.1021/acs.est.7b05258.

Drost, K., Chew, D., Petrus, J.A., Scholze, F., Woodhead, J.D., Schneider, J.W., and Harper, D.A.T., 2018, An Image Mapping Approach to U-Pb LA-ICP-MS Carbonate Dating and Applications to Direct Dating of Carbonate Sedimentation: Geochemistry, Geophysics, Geosystems, v. 19, doi:10.1029/2018GC007850.

Ekart, D.D., Cerling, T.E., Montañez, I.P., and Tabor, N.J., 1999, A 400 million year carbon isotope record of pedogenic carbonate: Implications for paleoatmospheric carbon dioxide: American Journal of Science, v. 299, doi:10.2475/ajs.299.10.805.

Elisha, B., Nuriel, P., Kylander-Clark, A., and Weinberger, R., 2021, Towards in situ U-Pb dating of dolomite: Geochronology, v. 3, doi:10.5194/gchron-3-337-2021.

Fan, Y., Li, H., and Miguez-Macho, G., 2013, Global patterns of groundwater table depth: Science, v. 339, doi:10.1126/science.1229881.

Freytet, P., and Plaziat, J.C., 1982, Continental carbonate sedimentation and pedogenesis - Late Cretaceous and Early Tertiary of southern France.: Continental carbonate sedimentation and pedogenesis - Late Cretaceous and Early Tertiary of southern France.,.

Gabitov, R. et al., 2021, Uptake of uranium by carbonate crystallization from reduced and oxidized hydrothermal fluids: Chemical Geology, v. 564, doi:10.1016/j.chemgeo.2020.120054.

Gauthier-Lafaye, F., Weber, F., and Ohmoto, H., 1989, Natural fission reactors of Oklo: Economic Geology, v. 84, doi:10.2113/gsecongeo.84.8.2286.

Gile, L.H., Hawley, J.W., and Grossman, R.B., 1981, Soils and geomorphology in the Basin and Range area of southern New Mexico—guidebook to the Desert Project: New Mexico Bureau of Mines and Mineral Resources Memoir 39,.

Godeau, N., Deschamps, P., Guihou, A., Leonide, P., Tendil, A., Gerdes, A., Hamelin, B., and Girard, J.P., 2018, U-Pb dating of calcite cement and diagenetic history in microporous carbonate reservoirs: Case of the Urgonian Limestone, France: Geology, v. 46, doi:10.1130/G39905.1.

Guillong, M., Wotzlaw, J.F., Looser, N., and Laurent, O., 2020, Evaluating the reliability of U-Pb laser ablation inductively coupled plasma mass spectrometry (LA-ICP-MS) carbonate geochronology: Matrix issues and a potential calcite validation reference material: Geochronology, v. 2, doi:10.5194/gchron-2-155-2020.

Hill, C.A., Polyak, V.J., Asmerom, Y., and P. Provencio, P., 2016, Constraints on a Late Cretaceous uplift, denudation, and incision of the Grand Canyon region, southwestern Colorado Plateau, USA, from U-Pb dating of lacustrine limestone: Tectonics, v. 35, doi:10.1002/2016TC004166.

Jaillard, B., Guyon, A., and Maurin, A.F., 1991, Structure and composition of calcified roots, and their identification in calcareous soils: Geoderma, v. 50, doi:10.1016/0016-7061(91)90034-Q.

Jasechko, S., Perrone, D., Seybold, H., Fan, Y., and Kirchner, J.W., 2020, Groundwater level observations in 250,000 coastal US wells reveal scope of potential seawater intrusion: Nature Communications, v. 11, doi:10.1038/s41467-020-17038-2.

Jochum, K.P. et al., 2011, Determination of reference values for NIST SRM 610-617 glasses following ISO guidelines: Geostandards and Geoanalytical Research, v. 35, doi:10.1111/j.1751-908X.2011.00120.x.

Kabanov, P., Anadón, P., and Krumbein, W.E., 2008, Microcodium: An extensive review and a proposed non-rhizogenic biologically induced origin for its formation: Sedimentary Geology, v. 205, doi:10.1016/j.sedgeo.2008.02.003.

Kayğılı, S., Aksoy, E., Jones, B., and Acar, Ş., 2019, The use of Microcodium to identify a paraconformity: An example from the Paleogene sequence of Malatya Basin (eastern Turkey): Sedimentary Geology, v. 380, doi:10.1016/j.sedgeo.2018.11.015.

Kelly, S.D., Newville, M.G., Cheng, L., Kemner, K.M., Sutton, S.R., Fenter, P., Sturchio, N.C., and Spötl, C., 2003, Uranyl incorporation in natural calcite: Environmental Science and Technology, v. 37, doi:10.1021/es025962f.

Kelly, S.D., Rasbury, E.T., Chattopadhyay, S., Kropf, A.J., and Kemner, K.M., 2006, Evidence of a stable uranyl site in ancient organic-rich calcite: Environmental Science and Technology, v. 40, doi:10.1021/es051970v.

Košir, A., 2004, Microcodium revisited: Root calcification products of terrestrial plants on carbonate-rich substrates: Journal of Sedimentary Research, v. 74, doi:10.1306/040404740845.

Košir, A., 1998. Rhizogenic calcretes from a shallow-marine carbonate succession, Paleocene of SW Slovenia (abstract): British Sedimentology Research Group, 37th Annual Meeting, London, Abstract Volume, 34 p.

Kraus, M.J., 1999, Paleosols in clastic sedimentary rocks: Their geologic applications: Earth Science Reviews, v. 47, doi:10.1016/S0012-8252(99)00026-4.

Layzell, A.L., Ludvigson, G.A., Smith, J.J., and Mandel, R.D., 2023, Using the factors of soil formation to assess stable carbon isotope disequilibrium in late Pleistocene (MIS 3) buried soils of the Great Plains, North America: Palaeogeography, Palaeoclimatology, Palaeoecology, v. 620, doi:10.1016/j.palaeo.2023.111574.

Li, Q., Parrish, R.R., Horstwood, M.S.A., and McArthur, J.M., 2014, U-Pb dating of cements in Mesozoic ammonites: Chemical Geology, v. 376, doi:10.1016/j.chemgeo.2014.03.020.

Li, Y., Zhang, W., Aydin, A., and Deng, X., 2018, Formation of calcareous nodules in loess–paleosol sequences: Reviews of existing models with a proposed new "per evapotranspiration model": Journal of Asian Earth Sciences, v. 154, doi:10.1016/j.jseaes.2017.12.002.

Liptzin, D., Silver, W.L., and Detto, M., 2011, Temporal Dynamics in Soil Oxygen and Greenhouse Gases in Two Humid Tropical Forests: Ecosystems, v. 14, doi:10.1007/s10021-010-9402-x.

Liu, E., Zhao, J.X., Wang, H., Pan, S., Feng, Y., Chen, Q., Liu, F., and Xu, J., 2021, LA-ICPMS in-situ U-Pb Geochronology of Low-Uranium Carbonate Minerals and Its Application to Reservoir Diagenetic Evolution Studies: Journal of Earth Science, v. 32, doi:10.1007/s12583-020-1084-5.

Ludvigson, G.A., Joeckel, R.M., González, L.A., Gulbranson, E.L., Rasbury, E.T., Hunt, G.J., Kirkland, J.I., and Madsen, S., 2010, Correlation of aptian-albian carbon isotope excursions in continental strata of the cretaceous Foreland Basin, Eastern Utah, U.S.A.: Journal of Sedimentary Research, v. 80, doi:10.2110/jsr.2010.086.

Martín-Chivelet, J., and Giménez, R., 1992, Palaeosols in microtidal carbonate sequences, Sierra de Utiel Formation, Upper Cretaceous, SE Spain: Sedimentary Geology, v. 81, doi:10.1016/0037-0738(92)90060-5.

Martínez, R.N., Apaldetti, C., Alcober, O.A., Colombi, C.E., Sereno, P.C., Fernandez, E., Malnis, P.S., Correa, G.A., and Abelin, D., 2012, Vertebrate succession in the ischigualasto formation: Journal of Vertebrate Paleontology, v. 32, doi:10.1080/02724634.2013.818546.

Martinez, R.N., Sereno, P.C., Alcober, O.A., Colombi, C.E., Renne, P.R., Montañez, I.P., and Currie, B.S., 2011, A basal dinosaur from the dawn of the dinosaur era in southwestern pangaea: Science, v. 331, doi:10.1126/science.1198467.

McClain, M.E. et al., 2003, Biogeochemical Hot Spots and Hot Moments at the Interface of Terrestrial and Aquatic Ecosystems: Ecosystems, v. 6, doi:10.1007/s10021-003-0161-9.

Methner, K., Mulch, A., Fiebig, J., Wacker, U., Gerdes, A., Graham, S.A., and Chamberlain, C.P., 2016, Rapid Middle Eocene temperature change in western North America: Earth and Planetary Science Letters, v. 450, doi:10.1016/j.epsl.2016.05.053.

Montano, D., Gasparrini, M., Gerdes, A., Della Porta, G., and Albert, R., 2021, In-situ U-Pb dating of Ries Crater lacustrine carbonates (Miocene, South-West Germany): Implications for continental carbonate chronostratigraphy: Earth and Planetary Science Letters, v. 568, doi:10.1016/j.epsl.2021.117011.

Montano, D., Gasparrini, M., Rohais, S., Albert, R., and Gerdes, A., 2022, Depositional age models in lacustrine systems from zircon and carbonate U-Pb geochronology: Sedimentology, v. 69, doi:10.1111/sed.13000.

Nuriel, P., Wotzlaw, J.F., Ovtcharova, M., Vaks, A., Stremtan, C., Šala, M., Roberts, N.M.W., and Kylander-Clark, A.R.C., 2021, The use of ASH-15 flowstone as a matrix-matched reference material for laser-ablation U-Pb geochronology of calcite: Geochronology, v. 3, doi:10.5194/gchron-3-35-2021.

Pan, L., Hu, A., Liang, F., Jiang, L., Hao, Y., Feng, Y., Shen, A., and Zhao, J., 2021, Diagenetic conditions and geodynamic setting of the middle Permian hydrothermal dolomites from southwest Sichuan Basin, SW China: Insights from in situ U–Pb carbonate geochronology and isotope geochemistry: Marine and Petroleum Geology, v. 129, doi:10.1016/j.marpetgeo.2021.105080.

Parrish, R.R., Parrish, C.M., and Lasalle, S., 2018, Vein calcite dating reveals Pyrenean orogen as cause of Paleogene deformation in southern England: Journal of the Geological Society, v. 175, doi:10.1144/jgs2017-107.

Paton, C., Hellstrom, J., Paul, B., Woodhead, J., and Hergt, J., 2011, Iolite: Freeware for the visualisation and processing of mass spectrometric data: Journal of Analytical Atomic Spectrometry, v. 26, doi:10.1039/c1ja10172b.

Platt, N.H., and Wright, V.P., 1991, Lacustrine carbonates: facies models, facies distributions and hydrocarbon aspects: Lacustrine facies analysis, doi:10.1002/9781444303919.ch3.

Plaziat, J.C., and Freytet, P., 1978. Le pseudo-microkasrs pédologique: un aspect particulier des paléo-pédogenèses développéess sur les depots calcaires lacustres dans le tertiaire du Lnaguedoc. Comptes Rendués Academie Science Paris, 286 (1978), pp. 1661-1664

Rasbury, E.T., Hanson, G.N., Meyers, W.J., Holt, W.E., Goldstein, R.H., and Saller, A.H., 1998, U-Pb dates of paleosols: constraints on late Paleozoic cycle durations and boundary ages: Geology, v. 26, p. 403–406, doi:10.1130/0091-7613(1998)026<0403:UPDOPC>2.3.CO;2.

Rasbury, E.T., and Cole, J.M., 2009, Directly dating geologic events: U-Pb dating of carbonates: Reviews of Geophysics, v. 47, doi:10.1029/2007RG000246.

Rasbury, E.T., Meyers, W.J., Hanson, G.N., Goldstein, R.H., and Saller, A.H., 2000, Relationship of uranium to petrography of caliche paleosols with application to precisely dating the time of sedimentation: Journal of Sedimentary Research, v. 70, doi:10.1306/2DC4092B-0E47-11D7-8643000102C1865D.

Rasbury, E.T., Piccione, G., Holt, W., and Ward, W.B., 2023, Potential for constraining sequence stratigraphy and cycle stratigraphy with U-Pb dating of carbonates: Earth-Science Reviews, v. 243, doi:10.1016/j.earscirev.2023.104495.

Rasbury, E.T., Present, T.M., Northrup, P., Tappero, R. V., Lanzirotti, A., Cole, J.M., Wooton, K.M., and Hatton, K., 2021, Tools for uranium characterization in carbonate samples: Case studies of natural U-Pb geochronology reference materials: Geochronology, v. 3, doi:10.5194/gchron-3-103-2021.

Rembe, J., Zhou, R., Sobel, E.R., Kley, J., Chen, J., Zhao, J.-X., Feng, Y., and Howard, D.L., 2022, Calcite U–Pb dating of altered ancient oceanic crust in the North Pamir, Central Asia: Geochronology, v. 4, p. 227–250, doi:10.5194/gchron-4-227-2022.

Renne, P.R., Mundil, R., Balco, G., Min, K., and Ludwig, K.R., 2010, Joint determination of 40K decay constants and 40Ar*/40K for the Fish Canyon sanidine standard, and improved accuracy for 40Ar/39Ar geochronology: Geochimica et Cosmochimica Acta, v. 74, doi:10.1016/j.gca.2010.06.017.

Retallack, G.J., 2009, Cambrian, Ordovician and Silurian pedostratigraphy and global events in Australia: Australian Journal of Earth Sciences, v. 56, doi:10.1080/08120090902806321.

Retallack, G.J., 1988, Field recognition of paleosols: Special Paper of the Geological Society of America, v. 216, doi:10.1130/SPE216-p1.

Retallack, G.J., 2005, Pedogenic carbonate proxies for amount and seasonality of precipitation in paleosols: Geology, v. 33, doi:10.1130/G21263.1.

Rihs, S., Sturchio, N.C., Orlandini, K., Cheng, L., Teng, H., Fenter, P., and Bedzyk, M.J., 2004, Interaction of uranyl with calcite in the presence of EDTA: Environmental Science and Technology, v. 38, doi:10.1021/es049847b.

Roberts, N.M.W. et al., 2020, Laser ablation inductively coupled plasma mass spectrometry (LA-ICP-MS) U-Pb carbonate geochronology: Strategies, progress, and limitations: Geochronology, v. 2, doi:10.5194/gchron-2-33-2020.

Roberts, N.M.W., and Holdsworth, R.E., 2022, Timescales of faulting through calcite geochronology: A review: Journal of Structural Geology, v. 158, doi:10.1016/j.jsg.2022.104578.

Roberts, N.M.W., Rasbury, E.T., Parrish, R.R., Smith, C.J., Horstwood, M.S.A., and Condon, D.J., 2017, A calcite reference material for LA-ICP-MS U-Pb geochronology: Geochemistry, Geophysics, Geosystems, v. 18, doi:10.1002/2016GC006784.

Rochín-Bañaga, H., Gastaldo, R.A., Davis, D.W., Neveling, J., Kamo, S.L., Looy, C. V., and Geissman, J.W., 2023, U-Pb dating of pedogenic calcite near the Permian−Triassic boundary, Karoo Basin, South Africa: Geological Society of America Bulletin, doi:10.1130/b36968.1.

Rogers, R.R., Swisher, C.C., Sereno, P.C., Monetta, A.M., Forster, C.A., and Martínez, R.N., 1993, The Ischigualasto tetrapod assemblage (Late Triassic, Argentina) and 40Ar/39Ar dating of dinosaur origins: Science, v. 260, doi:10.1126/science.260.5109.794.

Ross, J.B., Ludvigson, G.A., Möller, A., Gonzalez, L.A., and Walker, J.D., 2017, Stable isotope paleohydrology and chemostratigraphy of the Albian Wayan Formation from the wedge-top

depozone, North American Western Interior Basin: Science China Earth Sciences, v. 60, doi:10.1007/s11430-016-0087-5.

Rusakov, A., Makeev, A., Khokhlova, O., Kust, P., Lebedeva, M., Chernov, T., Golyeva, A., Popov, A., Kurbanova, F., and Puzanova, T., 2019, Paleoenvironmental reconstruction based on soils buried under Scythian fortification in the southern forest-steppe area of the East European Plain: Quaternary International, v. 502, doi:10.1016/j.quaint.2018.05.016.

Stacey, J.S., and Kramers, J.D., 1975, Approximation of terrestrial lead isotope evolution by a two-stage model: Earth and Planetary Science Letters, v. 26, doi:10.1016/0012-821X(75)90088-6.

Stojanović, M.D., Stevanović, D.R., Milojković, J. V., Grubišić, M.S., and Ileš, D.A., 2010, Phytotoxic effect of the uranium on the growing up and development the plant of corn: Water, Air, and Soil Pollution, v. 209, doi:10.1007/s11270-009-0208-4.

Sturchio, N.C., Antonio, M.R., Soderholm, L., Sutton, S.R., and Brannon, J.C., 1998, Tetravalent uranium in calcite: Science, v. 281, doi:10.1126/science.281.5379.971.

Tabor, N.J., Montañez, I.P., Kelso, K.A., Currie, B., Shipman, T., and Colombi, C., 2006, A Late Triassic soil catena: Landscape and climate controls on paleosol morphology and chemistry across the Carnian-age Ischigualasto-Villa Union basin, northwestern Argentina: Special Paper of the Geological Society of America, v. 416, doi:10.1130/2006.2416(02).

Tabor, N.J., and Myers, T.S., 2015, Paleosols as indicators of paleoenvironment and paleoclimate: Annual Review of Earth and Planetary Sciences, v. 43, doi:10.1146/annurev-earth-060614-105355.

Tandy, S., Brittain, S.R., Grail, B.M., Mcleod, C.W., Paterson, E., and Tomos, A.D., 2013, Fine scale measurement and mapping of uranium in soil solution in soil and plant-soil microcosms, with special reference to depleted uranium: Plant and Soil, v. 368, doi:10.1007/s11104-012-1526-7.

Vermeesch, P., 2018, IsoplotR: A free and open toolbox for geochronology: Geoscience Frontiers, v. 9, doi:10.1016/j.gsf.2018.04.001.

Wright, V.P., and Tucker, M., 1991, Calcretes: An Introduction: Calcretes, v. 2, p. 1–22, doi:10.1002/9781444304497.ch.

Zamanian, K., Pustovoytov, K., and Kuzyakov, Y., 2016, Pedogenic carbonates: Forms and formation processes: Earth-Science Reviews, v. 157, doi:10.1016/j.earscirev.2016.03.003.

Supplemental Material

Introduction

The following supporting information includes Tera-Wasserburg concordia plots of other carbonate precipitates within each studied carbonate nodule (Figure S1), and a table of laser methods used for U-Pb analyses (Table S1).

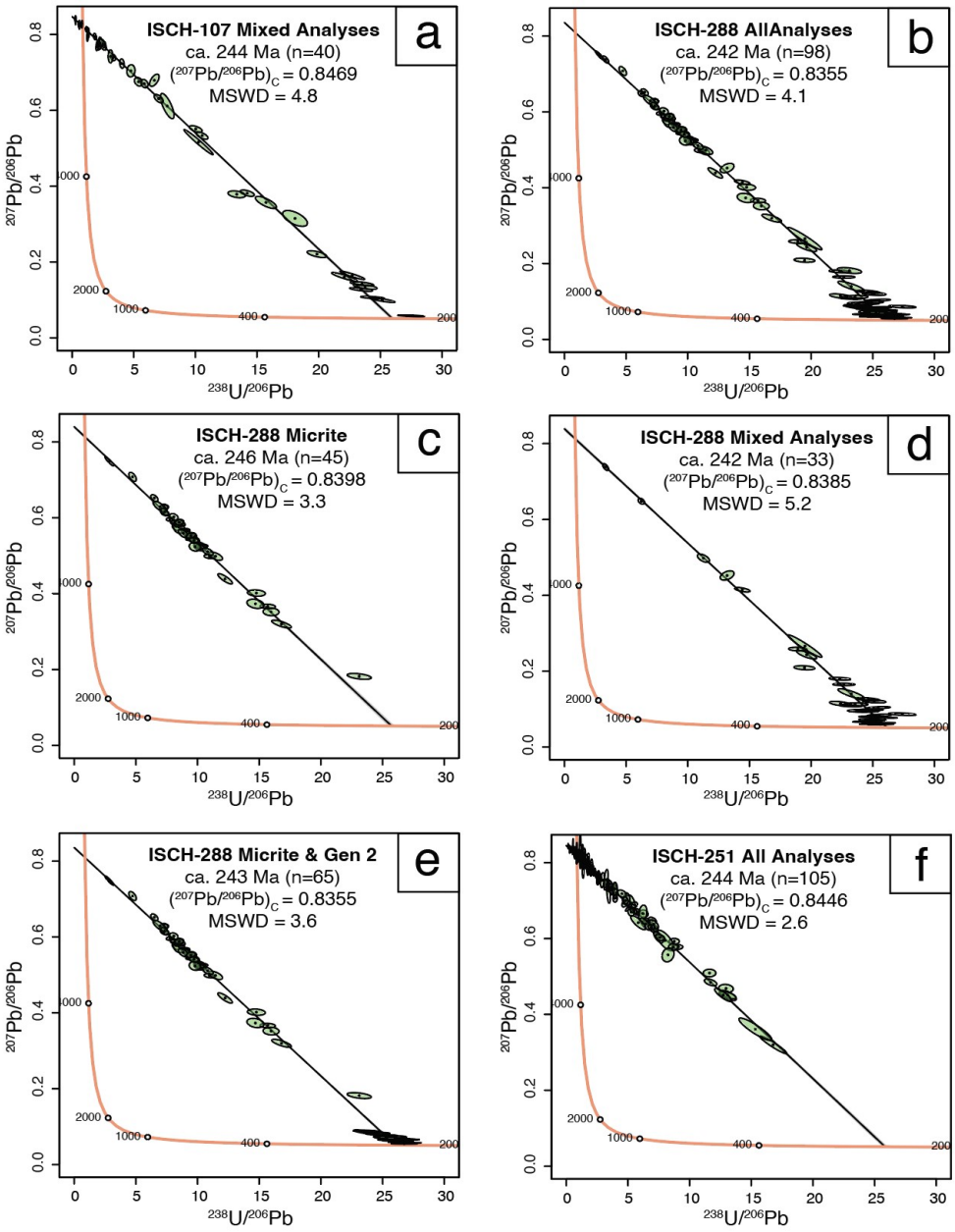

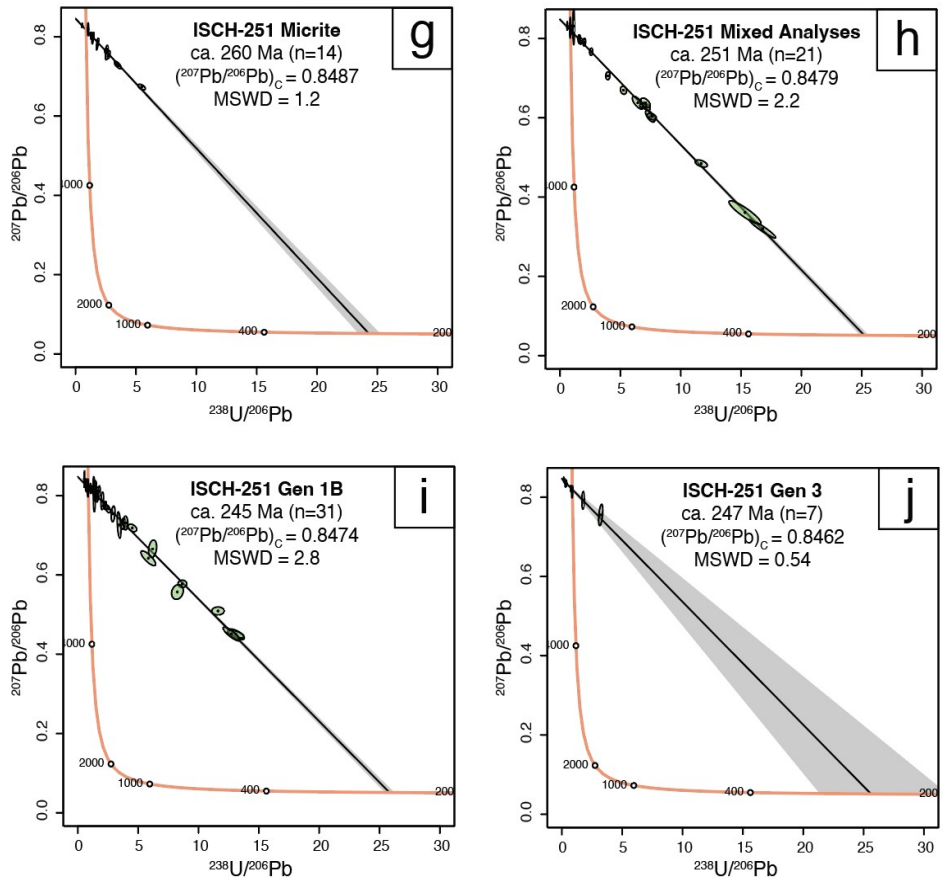

Figure S1. Tera-Wasserburg concordia plots of analyzed carbonate precipitates in the studied pedogenic carbonate nodules (a-j). Sample name and the corresponding analyzed carbonate precipitate of each plot is indicated in the plot title.

Publication	Aguirre-Palafox et al. 2024
Laboratory & Sample Preparation	
Laboratory name	The University of Kansas, Isotope Geochemistry Laboratories
Sample type/mineral	calcite
Sample preparation	polished thick sections
Imaging	reflected, transmitted light
Laser ablation system	
Make, Model & type	Arf excimer 193 nm, Photon Machines Analyte G2, Atlex300
Ablation cell & volume	Helex 2, two-volume cell
Laser wavelength (nm)	193
Pulse width (ns)	5
Fluence (J.cm-2)	3
Repetition rate (Hz)	10
Spot size (um)	85 µm circle
Carrier gas	He, 1.1 l/min, Ar, 1.4 l/min
Ablation duration (secs)	30
ICP-MS Instrument	
Make, Model & type	Thermo Element2 magnetic sector field ICP-MS
RF power (W)	1350
Make-up gas flow (l/min)	Ar, 1.35 l/min
sampling depth (z position of torch)	4.8
Detection system	single detector, counting
Masses measured	Pb206, Pb207, Pb208, Th232, U238
Integration time per peak (ms)	Pb206, Pb207, U238: 80 ms; Pb208, Th232: 8 ms
Total method time	46
Gas blank (s)	17
IC Dead time (ns)	8
UO+/U+ (%)	0.2
238+/232Th+	0.8
Data Processing	
Reference Material info	NIST 612 (Jochum et al. 2011), DBTL (Hill et all. 2016)
238U/238U	137.88
Data processing package used / Correction for LIEF	IGOR PRO, Iolite 2.5, U-PbGeochron3 for Pb, in-house Excel for U-Pb
Common-Pb correction, composition, uncertainty	none
Quality control / Validation	WC1 (Roberts et al. 2017)

Table S1. LA-ICP-MS methods data used in the U-Pb analyses of the Ischigualasto Formation carbonate nodules.

Supplementary Material References

Hill, C.A., Polyak, V.J., Asmerom, Y., and P. Provencio, P., 2016, Constraints on a Late Cretaceous uplift, denudation, and incision of the Grand Canyon region, southwestern Colorado Plateau, USA, from U-Pb dating of lacustrine limestone: Tectonics, v. 35, doi:10.1002/2016TC004166.

Jochum, K.P. et al., 2011, Determination of reference values for NIST SRM 610-617 glasses following ISO guidelines: Geostandards and Geoanalytical Research, v. 35, doi:10.1111/j.1751-908X.2011.00120.x.

Roberts, N.M.W., Rasbury, E.T., Parrish, R.R., Smith, C.J., Horstwood, M.S.A., and Condon, D.J., 2017, A calcite reference material for LA-ICP-MS U-Pb geochronology: Geochemistry, Geophysics, Geosystems, v. 18, doi:10.1002/2016GC006784.

Chapter 2: Paleosol carbonate U-Pb age constraints on the North American Wolfcampian-Leonardian Boundary, Eastern Shelf of the Midland Basin, USA.

Abstract

The late Paleozoic greater Permian Basin region hosts a rich archive of sedimentary, paleobiologic, and paleoclimatic records that capture a dynamic history of tectonic, eustatic, and climatic and biological changes during the Late Paleozoic Ice Age (LPIA). However, chronostratigraphic correlation across the region and to stratigraphic successions across Euramerica and elsewhere remains challenging due to the reliance on North American fusulinid and conodont biostratigraphy, the lack of widespread radiometrically dateable volcanic deposits, and disagreement over the stratigraphic placement and absolute age of the North American Wolfcampian-Leonardian Boundary (WLB). Here, we present the first laser ablation inductively coupled plasma mass spectrometry (LA-ICP-MS) U-Pb carbonate ages for carbonate nodules from paleosols in the Eastern Shelf of the Midland Basin. Based on the U-Pb carbonate ages and biostratigraphic correlations, the WLB in the Eastern Shelf succession likely lies within the middle-upper Waggoner Ranch Fm and has an age of 287.1 ± 4.4 Ma (mid-late Artinskian), making it correlative with the age for the Leonardian-type section from the Glass Mountains of West Texas. A modeled age of 290.8 ± 4.3 Ma (late Sakmarian) for the traditional WLB in the Eastern Shelf succession (base Petrolia Fm) indicates that this is a separate stratigraphic boundary that predates the WLB higher in the stratigraphy by ~5 Ma. The age for this pre-WLB is significant as it straddles the onset of the rapid rise in paleo-CO_2 at the close of the Sakmarian that marks the final stage of the LPIA and is associated with major local and global paleoenvironmental perturbations.

1. Introduction

Throughout the geologic record, Earth has experienced major climate shifts between greenhouse and icehouse states, with the latter being less common. The Late Paleozoic Ice Age (LPIA), spanning the Carboniferous Period and early Permian, was the longest-lived and potentially most extensive glacial period since the radiation of multicellular life. The LPIA archives repeated shifts from glacial to interglacial climate conditions documented to be in sync with fluctuations in paleo-CO_2 that spanned concentrations analogous to those of the last glacial period (≤220 ppm) to those (≥500 ppm), similar to what are projected for this century (Montañez et al. 2016; Steinthorsdottir et al. 2024; Jurakova et al. 2025). Widespread continental glaciogenic deposits in the mid- to high-latitudes indicate a dynamic glaciation–deglaciation record, with ice waxing and waning from multiple centers and multiple transcontinental ice sheets. These recurrent climate changes led to documented major environmental changes and ecosystem shifts (Richey et al. 2020; Chen et al. 2022; Marchetti et al., 2022; Montañez, 2022; Mattheaus et al. 2023) primarily inferred from study of low-latitude sedimentary successions.

The Permian Basin and adjacent platforms (herein referred to as the greater Permian Basin region), located in the western coastal zone of equatorial Pangaea during the late Carboniferous and early Permian (Fig. 1), host a rich archive of sedimentary, paleobiologic, and paleoclimatic records that capture a dynamic history of tectonic, eustatic, and climatic and biological changes in this key region during the late Paleozoic. In the marine successions, glacio-eustatic fluctuations inferred from base-level changes have been linked to the waxing and waning of continental glaciers in southern Gondwana (Alnazghah and Kerans, 2018; Kohn et al., 2019). These marine records, integrated with conodont and fusulinid biostratigraphy (e.g., Wilde, 1990; Kohn et al., 2019;

Wahlman, 2019; Wardlaw and Nestell, 2019; Lucas et al., 2022), have been used to reconstruct the extent and timing of major early Permian marine seaways (Lucas et al., 2024). Contemporaneous paleotropical terrestrial records from the greater Permian Basin region record long-term aridification from wetter conditions of the late Carboniferous to semiarid to arid climates of the Permian. This transition is documented by changes in fossil soil (paleosols) morphologies and their geochemical and stable isotopic compositions, as well as turnovers in faunal and floral assemblages documented as an increase of drought-tolerant forms such as reptiles among tetrapods and xeromorphic forms among plants (e.g., Tabor and Montañez, 2004; DiMichele et al., 2006; Tabor and Poulsen, 2008; Tabor et al., 2013; Falcon-Lang et al., 2015; Looy and Stevenson, 2014; Baumgardner et al., 2016; Koll and DiMichele, 2021). The upper Pennsylvanian to upper Permian strata of the greater Permian Basin region further record major shifts in depositional systems indicated by changes in sedimentary provenance that have been linked to late Paleozoic tectonic and climate processes (e.g., Lui and Stockli, 2019, Lawton et al., 2021; Tian et al., 2022; Griffis et al., 2023).

The latest Carboniferous through Permian succession of the Eastern Shelf of the Midland Basin, TX, part of the greater Permian Basin region (Fig. 1), has become an important late Paleozoic archive of the response of low-latitude terrestrial environmental and ecosystems to fluctuations in paleo-CO_2, global warmings and coolings, and sea-level changes driven by the waxing and waning of higher latitude continental glaciers (e.g., DiMichele et al., 2006, 2020; Montañez et al. 2007; Baumgardner et al., 2016; Koll and DiMichele, 2021; Zhu and Tabor, 2021; Griffis et al., 2023; Lucas et al., 2024). These studies have been possible in part given that the dominantly terrestrial record of the Eastern Shelf can be correlated to the deeper-water marine deposits of surrounding basins by the intercalated marine limestones, which were deposited by

marine incursions from the Midland Basin during transgressions (Hentz 1988; Lucas et al. 2024). Correlation of Eastern Shelf records to those developed from low-latitude successions beyond the greater Permian Basin region or from higher-latitude basins, however, has relied on the use of North American conodont and fusulinid biostratigraphy given the lack of radiometrically dateable volcanic deposits in the Eastern Shelf succession. Such correlations are limited by uncertainties in the correlation of the provincial North American marine biozones and stages with those defining the International stages (Chronostratigraphic Chart (www.stratigraphy.org/chart) (Boardman et al., 2009; Wahlman, 2019; Henderson et al. 2020; Lucas et al., 2022, 2024).

Application of U-Pb carbonate geochronology for dating sedimentary successions is now well documented (e.g., Li et al., 2014; Godeau et al., 2018; Parrish et al., 2018; Gulbranson et al., 2022; Rembe et al., 2021; Roberts and Holdsworth, 2022; Rasbury et al., 2009; Montano et al., 2022; Rochín-Bañaga et al., 2023; Aguirre Palafox et al., 2024). Pedogenic carbonates that precipitate in paleosols (fossil soils) hold significant potential for dating terrestrial successions, owing to advancements in imaging and U-Pb data processing techniques (Drost et al., 2018; Rochín-Bañaga et al., 2023) and the development of novel strategies for dating pedogenic carbonates that tie a well-characterized cement paragenetic framework to the ablated carbonate material (Aguirre Palafox et al., 2024). The common occurrence of carbonate-bearing paleosols throughout the Permian succession of the Eastern Shelf provides an ideal location to test the potential for building a U-Pb-constrained chronostratigraphic framework for this paleoecologically and paleoclimatically important succession.

Here, we present the first radioisotopic ages for pedogenic carbonates from the early Permian succession of the Eastern Shelf obtained by U-Pb LA-ICPMS. We interpret the U-Pb carbonate ages to constrain, within the uncertainty of the U-Pb ages, the timing of carbonate nodule formation

in the paleosols. We document that the U-Pb carbonate ages are in stratigraphic order and within the age range suggested by biostratigraphic correlations. We discuss the implications of the new radiometric ages for the Eastern Shelf succession on constraining the timing of regional biostratigraphic zones in the greater Permian Basin region and for their correlation to the international stages, as well as provide new constraints on the stratigraphic position and absolute age of a key, but long debated chronostratigraphic marker, the Wolfcampian-Leonardian Boundary, used for widespread correlation of paleotropical Euramerican successions and their records.

2. Geologic Background

The Permian Basin developed during flexural subsidence created by the collision of Laurasia and Gondwana during the Late Mississippian-Early Pennsylvanian. The Delaware and Midland basins, separated by the Central Basin Platform, constitute the main two depocenters of the Permian Basin (Fig. 1). The Eastern Shelf succession lies east of the Midland Basin and consists of terrestrial strata of latest Carboniferous (Late Pennsylvanian) through earliest Triassic age. The Eastern Shelf succession slopes west-southwest and contains intercalated marine limestones that extend out from the Midland Basin. To the south and east, the shelf is bordered by the Ouachita-Marathon orogenic belt, a part of the Central Pangaea Mountains, whereas to the north the Eastern Shelf is flanked by the Wichita Mountains (Hentz, 1988; Leary et al., 2020).

The diversity of strata in the greater Permian Basin region and general lack of radioisotope ages, in particular in shallower water and terrestrial successions, make precise chronostratigraphic correlation across the region and to stratigraphic successions elsewhere challenging. North

American fusulinid and conodont zonations have provided biostratigraphic constraints for correlation within the greater Permian Basin region and across North America, but disagreement exists over the stratigraphic placement and absolute ages of North American stage boundaries. A key boundary used for chronostratigraphic correlation is the Wolfcampian-Leonardian Boundary (WLB), but its utility has been compromised by uncertainties in its stratigraphic position in successions of the Greater Permian Basin region (Fig. 2).

The WLB has been defined in three locations in the greater Permian Basin region with varying stratigraphic positioning (Fig. 2). First, the stratotype WLB was proposed in the Glass Mountains of West Texas (Ross and Ross, 2003; Fig. 1) based on the first occurrence of the fusulinid *Schwagerina crassitectoria* and *S. guembeli* in the basal Skinner Ranch/Hess fms, which unconformably overlie the Lenox Hills Fm. Second, the stratigraphic position of the WLB in the type section correlates to the upper Artinskian international stage based on the occurrence of the conodont *Neostreptognathodus exsculptus* (Henderson, 2018; Lucas et al., 2022). The WLB in the Stephen L1V core from the Midland Basin is defined by the presence of *N. exsculptus* near the top of the Wolfcamp A strata, indicating a likely correlation to the lower to middle international Artinkskian stage (Kohn et al. 2019; Fig. 2). This WLB is dated at ~288 to 287 Ma based on the conodont biostratigraphy defined in the Midland Basin and its correlation to higher-precision U-Pb zircon ages from the lower Permian Dal'ny Tulkas section in Russia (Chernykh, 2006; Schmitz and Davydov, 2012; Kohln et al., 2019). Recent zircon TIMS ages from a core from the Midland Basin yield ages of 287.19 ± 0.5 Ma for the lower Wolfcamp A and 288.2 ± 1.7 Ma for the upper Wolfcamp B (±2σ; Tian et al., 2022) and agree with the age range of ~288 to 287 Ma for the WLB in the Midland Basin. Third, the WLB in the Eastern Shelf succession, which occurs in the Elm Creek Limestone at the base of the Petrolia Fm and has an interpolated age (293.5 to 292.3 Ma) of

early Sakmarian. This substantially older age than those of the two other boundaries is based on the presence of the conodonts *Sweetognathus whitei* and *Sw. bucaramangus* and their correlation to Midcontinent cyclothems and assumptions of astronomical forcing (Schmitz and Davydov, 2012; Henderson, 2018).

In this study, analyzed pedogenic carbonates span the Asselian through the Kungurian intervals of the Eastern Shelf succession (Fig. 3). The Wolfcampian Bowie Gp (Group) defines the lowermost stratigraphic unit in our study and comprises the Markley and Archer City fms, with the Carboniferous-Permian boundary located within the uppermost Markley Fm (Wardlaw, 2005; Wardlaw and Nestell, 2014). The Bowie Gp is characterized by channel-filling sandstones capped by paleosols that formed in floodplain mudstones (Hentz, 1988; Fig. 3), with some paleosols that can be laterally traced into marine limestones (Tabor and Montañez, 2004). The Wichita and Clear Fork groups overlie the Bowie Gp, with the Wichita Gp consisting of the Nocona, Petrolia and Waggoner Ranch fms. The uppermost strata are the Clear Fork Gp that consists of the Arroyo, Vale, and Choza fms in the study area (Fig. 3). Locally, the Wolfcampian-Leonardian Boundary is defined in the Elm Creek Limestone near the base of the Petrolia Fm, Wichita Gp. A shift in fluvial style from bedload-dominated sandstone facies of the Bowie Gp (Markley and Archer City fms) to low-energy fluvial sandstones and overbank deposits with thick paleosols occurs at the transition into the Wichita and Clear Fork groups (Hentz, 1988; Tabor and Montañez, 2004; Simon et al., 2018).

3. Materials and Methods

3.1 Carbonate petrography

Five pedogenic carbonate nodules were selected for study based on the stratigraphic position of the paleosols from which they were collected, including samples representative of the lowermost Bowie, Wichita Gp and uppermost Clear Fork Gp (Fig. 3). A polished thick section (~250 μm thick) was made of each sample and studied petrographically under plane-polarized light and by cathodoluminescence (CL). A cement microstratigraphy (i.e., paragenesis) was developed for each sample based on observed calcite crystal morphologies, cross-cutting cement relationships, spatial relationship to host micrite and primary features, including desiccation cracks and root casts, secondary porosity, non-carbonate authigenic minerals and on observed CL zonation.

3.2 U-Pb carbonate geochronology

In situ U-Pb analyses via LA-ICP-MS of the five polished thick sections were carried out in four sessions at the University of Kansas between 2021 and 2022. Analyses were performed using a Photon Machines Analyte G2 193 nm ArF excimer laser ablation system connected to a Thermo Scientific Element2 ICPMS. Laser ablation was carried out using a 3.0 J/cm^2 fluency and a 10 Hz repetition rate for 30 seconds creating circular 65 μm (ABBA-3C, NOPLAT, CFC-3D) and 85 μm (PAM-2F and WFBU-10E) diameter ablation spots. Ablated material was carried to the ICPMS in helium gas with a 1.1 l/min combined flow rate. Targeted areas of interest in each nodule were observed using the laser's built-in camera in transmitted and reflected light and cross-referenced with spatial maps of each sample microstratigraphy. Downhole fractionation, Pb isotopic fractionation and drift, and uncertainty propagation were corrected by bracketing measurements of unknowns with NIST 612 and NIST 614 glass reference material (Jochum et al., 2011) using the Iolite software (Paton et al., 2011). U-Pb fractionation was corrected and analytical scatter

propagated into isotopic ratios using an in-house Excel spreadsheet (based on the spreadsheet of Kylander-Clark, pers. comm. 2020). The carbonate reference material DBTL (Hill et al., 2016) was used to calibrate U-Pb ratios, and WC-1 (Roberts et al., 2017) was used for validation of the U-Pb fractionation.

The software package IsoplotR (Vermeesch, 2018) was used to visualize U–Pb data and calculate initial ^{234}U and ^{230}Th-disequilibrium corrected LA-ICPMS U-Pb ages. A conservative initial $^{234}U/^{238}U$ of 2 ± 2 (2σ) value was used based on the average of activity ratios from a compilation of shallow-groundwater studies (e.g., Roberts et al., 2020). An initial $^{230}Th/^{238}U$ of 0 was used because Th is highly insoluble in natural aqueous systems.

A Bayesian MCMC model was employed to refine U-Pb ages and their uncertainties for the Eastern Shelf samples. The model makes only a simple assumption of superposition, that the lowest sample in the studied stratigraphy (ABBA-3C; Fig. 3) is the oldest and that each stratigraphically overlying sample is younger than the one below it.

4. Results

4.1 Carbonate Paragenesis

The five studied pedogenic carbonate nodules consist of a matrix of calcite micrite (microcrystalline calcite < 10 um), with minor amounts of detrital Fe and Mn oxides. The nodules exhibit tapered casts of plant roots, pedogenic circumgranular and non-linear cracks, and less common post-pedogenetic fractures and porosity. The paragenesis (i.e., cement stratigraphy) of the nodules changes through the succession with calcite cement fabrics and morphologies reflecting changing environmental and local climate conditions through the interval of deposition.

Here, we present the paragenetic sequence for two nodules from the Archer City and Waggoner Ranch fms, as they represent end-members of the cement morphologies and paragenetic relationships observed in the five pedogenic carbonate nodules.

4.1.1 Archer City Paragenesis

A carbonate nodule (ABBA-3C) from a paleosol in the bonebed stratigraphic level in the upper Archer City Fm (Sandstone 8 of Hentz 1988; Fig. 3) contains two generations of calcite cements that line and occlude primary porosity. The first generation of calcite cement (Gen 1) consists of multiple layers (2 to 3) of clear fine-to-medium crystalline, prismatic to equant to subrounded crystals that line primary porosity and rim micritic clots and brecciated micrite host (Figs. 4A and 4C). Discrete cement layers (~30 to 100 μm in thickness) are differentiated by the presence of microcrystalline Fe-oxides that are incorporated in and/or overlie cement crystal terminations (Fig. 4B). Cement layers are irregular in thickness with crystal terminations that range, and pass laterally, from scalenohedral to subrounded or irregular to flat-topped crystals (Figs. 4A and 4B). A discontinuous thin (~10 to 30 μm) layer of microcrystalline calcite, in places forming micritic clots, overlies Gen 1 cements (Figs. 4A-4C). Gen 1 cements exhibit alternating thin (10s of μm) bands of dull to medium-dull luminescence (Fig. 4D).

Generation 1 cements are overlain by clear calcite cements (Gen 2) composed of medium-crystalline equant to subrounded crystals that occlude the remaining primary porosity (Figs. 4A-4C). Gen 2 cements exhibit well-developed CL zonation that is initially nonluminescent (NL) followed by a sequence of μm-scale brightly luminescent (BT) orange bands separated by a thin NL band, passing into alternating thicker (10s μm) NL and brightly luminescent yellow bands

(Fig. 4D). A similar cement paragenesis is observed in carbonate nodules from the Nocona (NOPLAT) and Petrolia (PAM-2F) fms.

Interpretation: Gen 1 cements are interpreted as having formed under vadose conditions during pedogenesis. Their subrounded to irregular crystal terminations record episodes of dissolution between precipitation of cement layers, possibly in response to seasonal or longer-term climate fluctuations. Intervals of flat-topped crystals in Gen 1 cements record precipitation terminated by the fluid-air meniscus in unsaturated pores of the vadose zone. Microcrystalline Fe-oxides occluded within and overlying Gen 1 cements are interpreted as authigenic, likely microbially mediated precipitates (Alonso-Zarza and Wright, 2010), although a detrital origin cannot be excluded. The micritic laminae and clots that overlie Gen 1 cements are also interpreted as bacterially mediated (Alonso-Zarza and Wright, 2010).

The medium-crystalline equant to subrounded crystal morphologies of Gen 2 cements indicate they precipitated under saturated conditions. The alternating NL to BT zonation observed in Gen 2 cements are interpreted to record the transition from overall oxidizing pore waters in the vadose zone into the zone proximal to the water table where redox (Eh) conditions decrease rapidly and vary due to fluctuations in the water table (Barnaby and Rimstidt, 1989) as previously proposed by; Aguirre-Palafox et al. (2024) for Triassic pedogenic nodules from the Ischigualasto Basin, Argentina.

4.1.2 Waggoner Ranch Paragenesis

A carbonate nodule (WFBU-10E) from a paleosol in the middle Waggoner Ranch Fm contains two generations of calcite cements that line and occlude primary porosity. The first generation of

calcite cement (Gen 1a) consists of a thick (100 to 200 μm) near isopachous layer of laminated fibrous cements that line root casts and syndepositional desiccation cracks and that overgrow brecciated host micrite (Figs. 5A-5C). The pink-gray coloration of Gen 1a cements is due to Fe- and Mn-oxide microcrystalline inclusions (Figs. 5A-5C). These cements exhibit dull luminescence. Gen 1b cements overgrow Gen 1a as a thin (30 to 50 μm) layer of clear fibrous cements with internal lamination defined by discrete μm-scale Fe-oxide crystals (Figs. 5B and 5C). These cements exhibit dull to nonluminescence. As with Gen 1a cements, a discontinuous thin (~10 to 30 μm) layer of microcrystalline calcite, in places forming micritic clots, overlies the fibrous cements. Parallel to randomly oriented, clear fibrous to elongated prismatic crystals with acute scalenohedral terminations (Fig. 5B) nucleate off of the Gen 1b fibrous cements. Tapered (v-shaped) root casts penetrate both Gen 1a and b cements and the host micrite (Figs. 5A, 5B and 5C); solely Gen 1b precipitated in the root casts (Figs. 5A and 5E). Very fine crystalline micrite discontinuously overlies some Gen 1a and 1b cements, always on the bottom of primary pores (Fig. 5D). This fine crystalline micrite exhibits bright yellow luminescence.

Gen 1 cements are overlain by multiple layers of prismatic to bladed calcite with acute scalenohedral crystal terminations (Gen 2). Cement layers (10s of μm) are defined by alternating inclusion-rich and inclusion-poor laminae, with the terminal layer exhibiting a highly irregular surface, including regions of acute scalenohedral terminations (Fig. 5E). Gen 2 cements on the bottom of some primary pores occur as irregularly distributed layers of subrounded equant crystals (Fig. 5B). These cements exhibit weakly zoned dull to bright luminescence. A similar cement paragenesis is observed in a carbonate nodule from the basal Clear Fork Gp (CFC-3D).

Gen 3 cements consist of blocky clear calcite crystals with well-developed rhombohedral crystal surfaces that occlude remaining primary porosity (Figs. 5B-5D) and exhibit dull orange luminescence.

Interpretation: Gen 1 cements are interpreted as forming during active soil processes. Calcite laminae are interpreted as biologically mediated precipitates that formed in vadose conditions under a seasonal semi-arid to arid climate (Wright et al., 1995; Alonso-Zarza, 2003; Zhou and Chafetz, 2009; Alonso-Zarza and Wright, 2010). Specifically, Gen 1a laminated fibrous cements are interpreted as calcrete cements. Their pink and gray coloration is due to the intermittent presence of manganese and iron oxides/hydroxides interpreted to record fluctuating pore fluid Eh in the soil (Barnaby and Rimstidt, 1989), most likely controlled by seasonal wetting and desiccation processes (Alonso-Zarza and Wright, 2010). Desiccation cracks and brecciated pedogenic micrite clasts further indicate periods of wetting and drying of the soil. The discrete Fe-oxide spherules between Gen 1a and 1b cements are interpreted as bacterially mediated oxide precipitates, whereas the discontinuous irregular layers of microcrystalline calcite overlying the Gen 1b fibrous cements are interpreted to have precipitated in bacterial biofilms. The outermost layer of parallel to randomly oriented clear fibrous to elongated prismatic crystals of Gen 1b cements is interpreted as having precipitated rapidly in evaporatively concentrated and supersaturated soil waters.

Tapered (v-shaped) root casts that penetrate Gen 1a and initial Gen1b cements, but are lined by the Gen 1b cements, indicate that both Gen 1a and 1b cements are syn-pedogenic having precipitated pre- to immediately post-root decay. The very fine crystalline micrite that overlies Gen 1 cements lining the bottom of primary pores is interpreted as vadose crystal silt that was

deposited in pores by soil waters flowing through the unsaturated zone of the soil and/or as having precipitated from evaporatively concentrated supersaturated pore waters.

Gen 2 cements that occur as irregularly distributed layers of subrounded equant crystals are interpreted as having formed in unsaturated pores in the soil. The Gen 2 cements with acute scalenohedral terminations are interpreted as having precipitated from supersaturated, evaporatively concentrated waters, as metals and other cations in concentrated waters inhibit the growth of calcite along crystal surfaces leading to acute scalenohedral terminations (e.g., Milodowski et al., 2018). The irregular surfaces of Gen 2 cement layers that are interpreted as dissolution surfaces and superposition of cements inferred to have precipitated from supersaturated fluids further indicate seasonal or climate-driven fluctuations in soil water chemistry.

Gen 3 cements that occur as blocky clear calcite crystals and occlude remaining primary porosity are interpreted to have formed in water-saturated pores of the phreatic zone. The medium dull luminescence of Gen 3 indicates the incorporation of both Mn^{2+} and Fe^{2+} in the crystal lattice, indicating Eh conditions typical of the deeper phreatic conditions.

4.2 U-Pb carbonate geochronology

^{234}U- and ^{230}Th-disequilibrium corrected LA-ICPMS U-Pb data are presented in Figure 6, Table 1, and in the Supporting Information. The MATLAB code for the Bayesian age-depth model is available at the GitHub repository at https://github.com/noahmclean and the U-Pb LA-ICP-MS data is available at geochron.org at

https://www.geochron.org/dataset/html/geochron_dataset_2025_03_21_8TrmD

Uncertainties for the U-Pb intercept and the MCMC-modeled dates are reported as ± 2σ and expressed in the format X/Y/Z, where X incorporates only analytical uncertainties, Y additionally includes the uncertainty in the age of the primary reference material (here, DBTL; Hill et al., 2016), and Z includes our ± 2% external reproducibility.

The stratigraphically lowest carbonate nodule (ABBA-3C) was collected from the upper Archer City Fm (Sandstone 8 of Hentz 1988; Fig. 3). Based on data from Gen 1 cements characteristic of the Archer City paragenesis, ABBA-3C has an isochron U-Pb age of 294.3 ± 6.2/6.9/9.0 Ma (MSWD = 1.7, n=22; Fig. 6A) and a modeled age of 296.0 ± 5.1/5.9/8.4 Ma (Table 1). Calcite precipitates from the ABBA-3C have a Uranium (U) concentration and spread in $^{238}U/^{206}Pb$ ranging from 0.5 to 3.5 ppm by mass and 0.2 to 13, respectively. An isochron age of 294.0 ± 15/15.3/16.4 Ma (MSWD = 1.3, n=9) was calculated from Gen 2 cements in the ABBA-3C nodule.

Nodule NOPLAT was collected from the uppermost Nocona Fm (lower Parkey's Oil Patch; Fig. 3). NOPLAT has a calculated U-Pb age of 292.7 ± 8.7/9.2/10.9 Ma (MSWD = 1.5, n=12; Fig. 6B) and a modeled age of 292.5 ± 4.8/5.6/8.1 Ma based on Gen 1 cements characteristic of the Archer City Fm paragenesis (Table 1). The U concentration and spread in $^{238}U/^{206}Pb$ of calcite precipitates in the NOPLAT nodule range from 2 to 10 ppm by mass and 0.7 to 14, respectively.

Nodule PAM-2F was collected from the middle Petrolia Fm (Fig. 3). PAM-2F has an isochron U-Pb age of 289.2 ± 5.9/6.6/8.8 Ma (MSWD = 2.8, n=14) obtained from analyzing Gen 1 cements characteristic of the Archer City paragenesis. An isochron age of 289.4 ± 4.6/5.4/7.9 Ma (MSWD = 1.2, n=12; Fig. 6C) and a modeled age of 289.1 ± 3.8/4.8/7.5 Ma was obtained from analyzing Gen 2 cements similar to Gen 2 cements characteristic of the Archer City paragenesis (Table 1).

The U concentration and spread in $^{238}U/^{206}Pb$ of calcite precipitates from the PAM-2F nodule range from 0.6 to 17 ppm by mass and 1.7 to 20, respectively.

Nodule WFBU-10E was collected from the middle Waggoner Ranch Fm (Fig. 3). WFBU-10E has a calculated U-Pb age of 284.2 ± 7.4/7.9/9.8 Ma (MSWD = 1.5, n=38; Fig. 6D) and a modeled age of 285.1 ± 4.8/5.6/8.0 Ma based on Gen 1 cements (Table 1). Calcite precipitates in the WFBU-10E nodule have a U concentration and spread in $^{238}U/^{206}Pb$ of 0.8 to 4.9 ppm by mass and 0.3 to 9.9, respectively.

The stratigraphically highest nodule (CFC-3D) was collected from the basal Clear Fork Gp (Arroyo Fm; Fig. 3). CFC-3D has an isochron U-Pb age of 283.2 ± 6.1/6.7/8.8 Ma (MSWD = 1.7, n=34; Fig. 6E) and a modeled age of 281.6 ± 5.0/5.7/8.0 Ma based on Gen 2 cements characteristic of the Waggoner Ranch paragenesis. The uranium concentration and spread in $^{238}U/^{206}Pb$ of calcite precipitates in CFC-3D ranges from 1.4 to 5.3 ppm by mass and 1.2 to 8.9, respectively.

Isochron dates calculated from Gen 3 cements yield geologically meaningless ages with high age uncertainties outside the expected age range (early Permian) for the Eastern Shelf succession. This is explained by the limited number of analyses from Gen 3 cements (n = 3).

5. Discussion

5.1 Accuracy and Precision of the Pedogenic Carbonate Nodule Ages from the Eastern Shelf Succession

In this study of pedogenic carbonates from paleosols that developed in the lower Permian succession of the Eastern Shelf, greater Permian Basin region, we demonstrate that U-Pb dating of calcite cements, guided by nodule-specific paragenetic frameworks, provides radioisotope

constraints on the timing of soil formation and early burial of the soil across the groundwater table into the shallow phreatic zone. The calculated U-Pb carbonate ages for the five studied nodules are in stratigraphic order, with their uncertainties in agreement with ages constrained by the regional biostratigraphy (Fig. 2; Table 1). All U-Pb ages for the nodules obtained from lower Permian strata are constrained to the early Permian.

U-Pb dating of isolated calcite cements that precipitated in primary porosity of pedogenic carbonate nodules has recently been shown to successfully constrain the timing of soil formation (vadose zone) through early diagenesis in the shallow phreatic zone (Aguirre-Palafox et al. 2004). Gen 1 cements in the Archer City nodule are interpreted to have formed under vadose conditions during pedogenesis. Gen 1 calcrete cements from the Waggoner Ranch nodule are also interpreted to have formed during pedogenesis but under seasonal, drier conditions. Uranium enrichment in the Gen 1 cements from the Archer City and Waggoner Ranch parageneses is attributed to their association with organic matter (Rasbury et al., 2000). In the geologic record, organic-rich material in rhizoliths (i.e., carbonate that formed around roots) and other sedimentary deposits (e.g., black shales) is strongly associated with higher U concentrations (Cumberland et al., 2016; Cuney, 2010; Gauthier-Lafaye et al., 1989; Kelly et al., 2006; Rasbury et al., 1997). Studies of modern soils also document higher U concentrations in plant roots and in soil solution surrounding the roots (Stojanović et al., 2010; Tandy et al., 2013). In the studied strata of the Eastern Shelf succession, a modeled age of 296.0 ± 5.1/5.9/8.4 Ma obtained from analysis of Gen 1 cements in the stratigraphically lowermost nodule (ABBA-3C) indicates an Asselian age (Figs. 2 and 3). The age for the ABBA-3C nodule is in stratigraphic agreement with the Carboniferous-Permian boundary (298.89 Ma; Ramezani et al., 2007) that is identified in the uppermost Markley Fm that underlies the Archer City Fm (Wardlaw, 2005; Wardlaw and Nestell, 2014; Fig. 2).

Gen 2 cements in the Archer City and Waggoner Ranch nodules are interpreted as syn-depositional to earliest burial cements precipitated near a fluctuating groundwater table or during the transition from the vadose zone into the shallow phreatic zone. The stratigraphically highest nodule (CFC-3D) in the basal Clear Fork Gp has a modeled age of 281.6 ± 5.0/5.7/8.0 Ma obtained from analysis of Gen 2 cements (Figs. 2 and 3). The age for the CFC-3D nodule is consistent with the independent assignment of the Clear Fork Gp to the international Kungurian Stage based on the occurrence of the fusulinid *S. crassitectoria* in the underlying Talpa Limestone of the Wichita/Albany Gp (Myers, 1968; Fig. 2); the *S. crassitectoria* biozone is confined to the late Artinskian (Wahlman, 2019). The U-Pb ages for the carbonate nodules (NOPLAT, PAM-2F, WBFU-10E; Figs. 2 and 3; Table 1) in strata between the lowermost Archer City and uppermost Clear Fork nodules are in stratigraphic order, albeit the ages for two nodules are somewhat younger than expected but still in agreement within the age uncertainties (see section 5.3 below).

Aguirre-Palafox et al. (2004) presented U-Pb ages, estimated using syn-depositional (Gen 1) to earliest burial cements that formed in the shallow phreatic zone (Gen 2) in carbonate nodules from the Late Triassic Ischigualasto Formation of northwestern Argentina, that are in stratigraphic order and agree with the radioisotopic ages of volcanic ashes. U-Pb ages from analogous calcite cements (Figs. 4 and 5) in carbonate nodules from the Eastern Shelf succession presented in this study are also in stratigraphic order and generally agree with regional biostratigraphic constraints. Despite the geographical and geological differences of the two successions, both studies indicate that U-Pb chronostratigraphic frameworks can be established via U-Pb dating of syn-depositional and earliest burial calcite cements from carbonate nodules formed in paleosols. Current U-Pb carbonate geochronology limitations do not permit distinction between ages from syn-depositional and earliest burial calcite cements as the transition of carbonate nodules through the vadose into

the phreatic realm typically occurs in 1 kyr to 10s of kyrs (e.g., Deutz et al., 2002; Rusakov et al., 2019; Layzell et al., 2023). Further advances in U-Pb carbonate geochronology are needed to aid in the age distinction between the two diagenetic environments.

5.2 Limitations of U-Pb Carbonate Age Uncertainties

Despite significant analytical advancements in U-Pb carbonate dating via LA-ICP-MS, the age uncertainties of the studied carbonate nodules are an order of magnitude greater than those achieved by higher-precision methods such as single zircon ID-TIMS U-Pb dating. The precision of any carbonate U-Pb analysis depends on three factors: the precision of the measured isotope ratios, the spread in U-Pb ratios within the targeted carbonate sample/generation, and how radiogenic the samples are. To date, few studies have directly targeted pedogenic carbonate nodules for U-Pb carbonate geochronology (Methner et al., 2016; Rochín-Bañaga et al., 2023; Aguirre-Palafox et al., 2024), and only one study has carried out U-Pb carbonate analysis in a well-defined cement paragenetic framework. Consequently, our understanding of the factors influencing the precision of carbonate U-Pb dates will expand as more studies evaluate pedogenic carbonates as a reliable chronometer. This study, building on the work of Aguirre-Palafox et al. (2024), advances this understanding by further documenting the importance of carrying out U-Pb carbonate dating within a robust paragenetic framework to accurately link U-Pb signatures with the temporal context of the cement generations (paragenesis). For example, targeting micritic carbonate matrix in carbonate nodules can yield U-Pb carbonate ages with reasonable MSWDs and age uncertainties, but ages that lack geological context due to the higher abundance of detrital material (e.g., oxides and clays) within the carbonate micrite that increases the potential for mixing of materials of different geochemical compositions and of generations of micritic cement (cf.

Deutz et al. 2002). In turn, such complications contribute to higher U-Pb isotopic scatter around best-fit lines on Tera-Wasserburg concordia plots (Aguirre-Palafox et al., 2024).

The U-Pb dates presented in this study were derived from isolated cements but with thicknesses only slightly larger than the 65 and 85 μm diameter laser spot used for analysis. The lack of thicker cements limited the number of U-Pb data points used for constructing individual sample isochrons or made analyzing a single generation of cement more difficult. The lower number of analyses, in turn, can result in an underrepresentation in the spread of measured $^{238}U/^{206}Pb$ and $^{207}Pb/^{206}Pb$ ratios, potentially leading to insufficient data to accurately anchor end-members in Tera-Wasserburg concordia plots. Targeting more cements of paragenetic equivalence in time-equivalent nodules could improve age uncertainties and should be prioritized in future studies.

Enhanced analytical, data-processing, and age-modeling techniques are also necessary to further advance the U-Pb dating of pedogenic carbonates. A Bayesian approach to U-Pb data processing and age modeling that incorporates superposition constraints has proven effective in reducing age uncertainties (Keller et al., 2018; Rochín-Bañaga et al., 2023). Additionally, using U-Pb carbonate LA-ICP-MS analysis to target specific cement generations for analysis by ID-TIMS could achieve substantially higher precision and accuracy of U-Pb dates of pedogenic carbonates than those obtained by LA-ICP-MS alone. Utilizing an integrated ID-TIMS approach has the potential to circumvent the high external uncertainty contribution (typically >2%) associated with current U-Pb carbonate LA-ICP-MS limitations and could yield age precision better than 0.5% based on well-characterized laser-ablation-guided sampling. To what degree an integrated ID-TIMS approach can be applied will be determined by the spatial extent of each cement generation within each nodule sample.

5.3 U-Pb Carbonate Age constraints for correlating the North American biozones to the International Stages.

The new radiometric ages for the carbonate nodules from the lower Permian strata of the Eastern Shelf succession permit direct correlation to the international stages by assessing the stratigraphic relationship of the U-Pb ages to the conodont and fusulinid biostratigraphy.

The Carboniferous-Permian boundary in the greater Permian Basin and Midcontinent regions is defined by the first appearance of *Streptognathodus isolatus* (Ritter, 1995; Wardlaw and Nestell, 2019). In the Midland Basin, *S. isolatus* occurs at the base of the Stockwether Limestone Member of the Pueblo Fm (Wardlaw, 2005; Wardlaw and Nestell, 2014) and is correlated to the top of the Markley Fm in the Eastern Shelf succession based on mapping of sandstone units (Hentz, 1988). The modeled age of 296.0 ± 5.1 Ma for the stratigraphically lowest studied carbonate nodule (ABBA-3C) from the uppermost Archer City Fm indicates an Asselian age (298.9 to 293.52 Ma; Fig. 2), the first lower Permian international stage. An Asselian age is also in agreement with the nodule's stratigraphic position ~100 m above the Carboniferous-Permian boundary (298.89 Ma; Ramezani et al., 2007). A U-Pb constrained Asselian age further aligns with the mid to late Asselian age suggested by the occurrence of the conodont *Sweetognathus merrilli* in the Coleman Junction Limestone (Coleman Junction Fm) and which is assigned an age range of 297.2 Ma to 294.9 Ma based on correlation to the Midcontinent US succession (Boardman et al., 2009; Henderson, 2018; Fig. 2).

The modeled U-Pb ages for the two nodules from the Nocona and Petrolia fms in the Eastern Shelf succession place them within the Sakmarian (2nd Permian stage; 293.52 to 290.51 Ma) and early Artinskian (3rd stage; 290.51 to 283.3 Ma) international stages (Fig. 2). The modeled U-Pb age of 292.5 ± 4.8 Ma for the NOPLAT nodule from the top of the Nocona Fm, ~120 m above the

Archer City (ABBA-3C) nodule (Fig. 2), places it within the mid-Sakmarian Stage. However, an older late Asselian age is expected given its stratigraphic position ~20 m below the Elm Creek Limestone. This reflects the occurrence of conodonts *Sw. whitei* and *Sw. bucaramangus* in the Elm Creek Limestone that have an assigned early Sakmarian age based on correlation to the Kansas Midcontinent succession (Wardlaw, 2005; Holterhoff et al., 2013; Henderson, 2018). That said, the biostratigraphically constrained late Asselian age for the NOPLAT nodule is within the calculated precision of the U-Pb carbonate age.

The modeled age of 289.1 ± 3.8 Ma for the nodule (PAM-2F) collected from the middle Petrolia Fm indicates an early Artinskian age. As with the NOPLAT nodule, a slightly older, mid-late Sakmarian age is expected given the stratigraphic proximity of the paleosol, ~45 m above the Elm Creek Limestone, which has been assigned an early Sakmarian age based on the conodont biostratigraphy (Wardlaw, 2005; Holterhoff et al. 2013; Henderson, 2018). The age for the pedogenic nodule (PAM-2F) from the middle Petrolia Fm, however, overlaps within the uncertainty of the U-Pb carbonate age, with the biostratigraphically assigned mid-late Sakmarian age.

The modeled U-Pb ages for the remaining nodules place them within the late Artinskian and Kungurian (282.2 to 274.37 Ma) international stages (Fig. 2). The modeled age of 285.1 ± 4.8 Ma for the WFBU-10E nodule from the middle Waggoner Ranch Fm, ~135 m above the PAM-2F nodule, indicates a late Artinskian age given the assigned age range of this stage (290.51 to 282.3 Ma). The 285.1 ± 4.8 Ma age also aligns well with the age inferred from the stratigraphic position of this nodule ~25 m below the Talpa Fm (Fig. 2), which is biostratigraphically constrained to ~286 to 283 Ma (mid-to-late Artinskian) based on the presence of the fusulinid *Schwagerina crassitectoria* (Myers, 1968; Ross and Ross, 2003; Wardlaw, 2005). A modeled age of 281.6 ± 5.0

Ma for the stratigraphically uppermost carbonate nodule (CFC-3D) from the basal Clear Fork Gp and ~85 m above the Waggoner Ranch nodule indicates an early Kungurian age (Fig. 2). This age aligns well with the late Artinskian age extrapolated from its stratigraphic position ~60 m above the *Schwagerina crassitectoria* bearing Talpa Fm.

5.4 Constraining the Wolfcampian-Leonardian Boundary in the Eastern Shelf Succession

The age and stratigraphic position of the Wolfcampian-Leonardian Boundary (WLB) within the greater Permian Basin region varies regionally (Fig. 2), reflecting the different criteria used to define the boundary, including lithologic changes and the regional biostratigraphy (e.g., Wilde, 1990; Ross and Ross, 2003; Henderson and Shen, 2020; see Section 'Geologic Setting' for details). The new modeled age of 285.1 ± 4.8 Ma for nodule WFBU-10E suggests the WLB in the Eastern Shelf succession is defined in the upper Artinskian (mid-upper Waggoner Ranch Fm), which comes 35 m below the Talpa Fm that includes the fusulinid *S. crassitectoria* (Myers, 1968). The mid-late Artinskian age (287.1 ± 4.4 Ma) for WLB in the Eastern Shelf succession aligns well with the type WLB in the Glass Mountains type-section of West Texas (Ross and Ross, 1963; Fig. 2), further correlating the age of the WLB across the greater Permian Basin region. In contrast, the modeled age of 290.8 ± 4.3 Ma for the traditionally assigned WLB at the base of the Petrolia Fm based on the U-Pb ages of the underlying NOPLAT nodule (292.5 ± 4.8 Ma) in the Nocona Fm and the overlying PAM-2F nodule (289.1 ± 3.8 Ma) in the Petrolia Fm indicates a late Sakmarian age. This age is ~5 Myr older than the type WLB from the Glass Mountains and ~3 to 4 Ma older than the WLB defined in the Stephen L1V core from the northern Midland Basin (Fig. 2). This stratigraphic offset suggests that the traditional WLB records a unique stratigraphic boundary that we will refer to as the "pre-WLB." The age of 290.8 ± 4.3 Ma for the pre-WLB is in better

agreement with the “WLB” from the U.S. Midcontinent (Kansas) defined by a lithological change from cyclothems to red beds and evaporites and with an interpolated age range of 293.5 to 292.3 Ma (early to mid-Sakmarian; Fig. 2).

The correlation of the pre-WLB in the Eastern Shelf succession to the latter part of the international Sakmarian Stage is significant as it aligns with major regional- to global-scale paleoenvironmental, paleoclimatic, and paleobiological changes that occurred during the final stage of the LPIA. Regionally, a shift from bedload to suspended load-dominated fluvial systems is recorded immediately following the pre-WLB in the Eastern Shelf succession (Griffis et al., 2023). This shift in the dominant mode of deposition is accompanied by changes in zircon provenance that indicate a decrease in the erosion of local bedrock and evidence for increased eolian transport from increasingly arid exposed areas in the greater Permian Basin region to the Eastern Shelf and Midland Basin (Liu and Stockli, 2019; Griffis et al., 2023). The increasing influence of eolian deposition across the Eastern Shelf and greater Permian Basin region is attributed to increased aridity in tropical western Euramerica (Soreghan et al., 2018; Griffis et al., 2023). Notably, the modeled U-Pb ages of the calcrete cements in nodules stratigraphically above the pre-WLB (289.1 ± 3.8 Ma for PAM-2F, early Artinskian; 285.1 ± 4.8 Ma for WFBU-10E, late Artinskian; and 281.6 ± 5.0 Ma for CFC-3D, early Kungurian) further support the existence highly seasonal semi-arid to arid climate in the greater Permian Basin region by the early Artinskian Stage (Fig. 2).

Globally, the modeled age of 290.8 ± 4.3 Ma for the pre-WLB stratigraphic boundary recorded in the Eastern Shelf succession coincides with the transition from the 10-Myr CO_2 nadir that spanned the Asselian and Sakmarian to the onset of the rapid rise in paleo-CO_2 through the remainder of the early Permian (Richey et al., 2020), marking the demise of the LPIA. This

transition, straddling the pre-WLB, was also associated with major perturbations in terrestrial and marine ecosystems. In the terrestrial realm, a marked increase in xeromorphic and a decrease in hygromorphic plants and fauna is documented in Euramerica successions starting in the early Artinskian (DiMichele et al., 2001; Looy, 2007; Looy and Stevenson, 2014; Richey et al., 2020; Marchetti et al., 2024). In marine ecosystems, low rates of global macroevolution in marine organisms returned to pre-LPIA rates (Stanley and Powell, 2003), and a turnover from cold-adapted to warm-adapted marine rugose corals, brachiopods and bivalves is documented at the Sakmarian-Artinskian boundary (Wang et al., 2006; Powell, 2005; Clapham and James, 2008).

6. Conclusions

The first U-Pb carbonate ages of pedogenic carbonate nodules from the Eastern Shelf succession obtained via LA-ICP-MS are in stratigraphic order and agree with regional biostratigraphy constraints. The new radiometric ages presented here, spanning from the international Asselian Stage (296.0 ± 5.1 Ma) to the international Kungurian Stage (281.6 ± 5.0 Ma), provide new constraints on the chronology of the conodont and fusulinid biozones in the lower Permian strata of the Eastern Shelf succession by permitting direct correlation to the international stages. Based on the U-Pb carbonate ages and the *S. crassitectoria* biozone, the Wolfcampian-Leonardian Boundary (WLB) in the studied Eastern Shelf succession likely lies within the middle-upper Waggoner Ranch Fm and has a modeled age of 287.1 ± 4.4 Ma (mid-late Artinskian), making it correlative with the extrapolated age of ~286 Ma for the Leonardian-type section from the Glass Mountains of West Texas. Conversely, the modeled age of 290.8 ± 4.3 Ma for the traditional proposed level for the WLB within the Eastern Shelf succession (Elm Creek Limestone/base Petrolia Fm) indicates that this is a separate stratigraphic boundary that predates

the WLB higher in the stratigraphy by ~5 Ma. The age of 290.8 ± 4.3 Ma for the pre-WLB agrees instead, within the uncertainty of the modeled age, with the "WLB" from Kansas with an interpolated age within the range of 293.5 to 292.3 Ma (early to mid-Sakmarian), further indicating a separate stratigraphic boundary.

The ages of 290.8 ± 4.3 Ma for the pre-WLB and 287.1 ± 4.4 Ma for the WLB in the Eastern Shelf succession can be used as markers to more accurately correlate major paleoenvironmental, paleoclimatic, and paleobiological records among the greater Permian Basin region and other low- and high-latitude successions. The age of the pre-WLB in the Eastern Shelf succession is significant as it aligns with global environmental perturbations at the close of the Sakmarian international stage, including a decrease in the geographical distribution of glaciogenic deposits and inferred duration of glaciation in high-latitude successions, and loss of stratigraphic cyclicity and diminished magnitudes of sea-level fluctuations in low-latitude successions. These environmental shifts correlate with an abrupt rise in paleo-CO_2, exceeding the threshold for continental ice formation at the close of the Sakmarian, marking the beginning of the demise of the LPIA.

Open Research

The LA-ICPMS U-Pb data used for concordia plots in the study are available at Geocrhon.org via https://www.geochron.org/dataset/html/geochron_dataset_2025_03_21_8TrmD

Figures and Table:

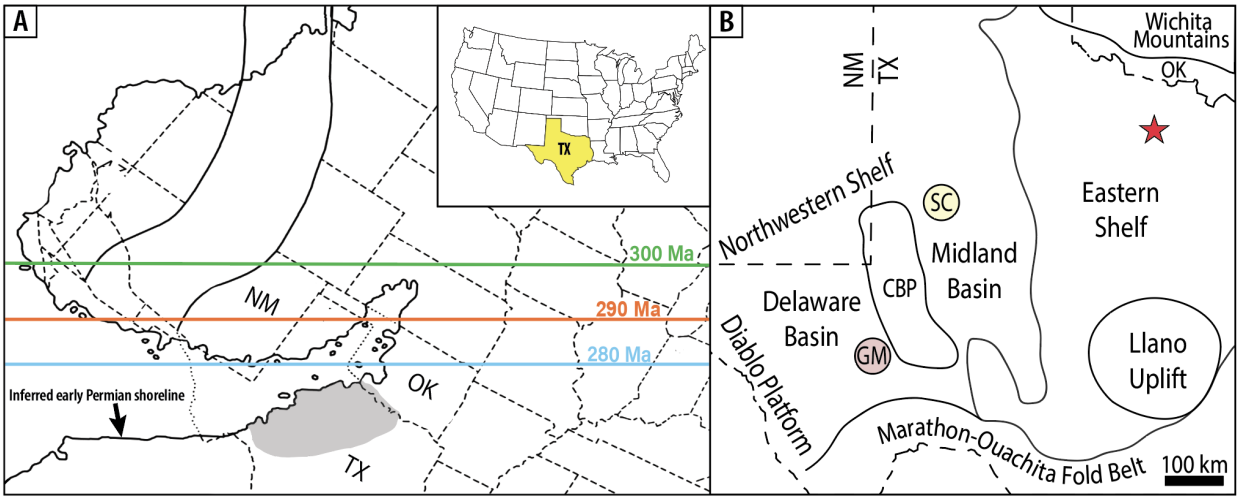

Figure1. Geographic position of the Eastern Shelf of the Midland Basin during the late Paleozoic and present-day modified from Richey et al. (2020). (A) Location of the Permian Eastern Shelf succession (shaded area) with superimposed positions of the reconstructed latest Carboniferous (300 Ma) and early Permian equator (290 and 280 Ma) (Scotese 2016). (B) Map of Carboniferous-Permian basins and platforms of the Greater Permian Basin region, including the Eastern Shelf of the Midland Basin. Red star indicates sampling locality for carbonate nodules used in this study. CBP: Central Basin Platform; GM: Glass Mountains; SC: Stephen LV1 core.

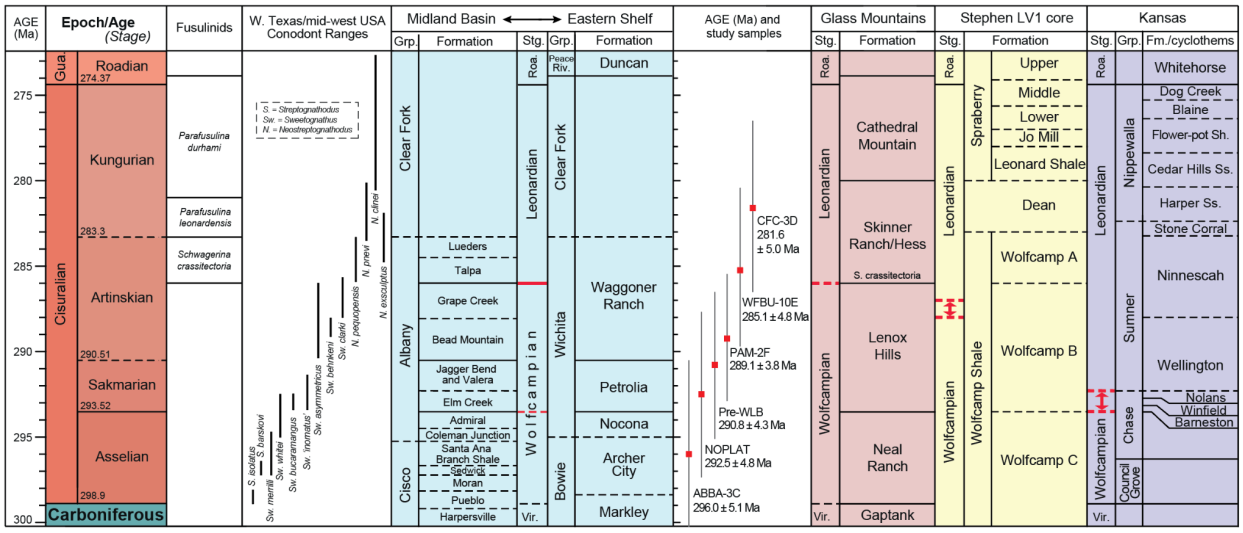

Figure 2. Chronostratigraphic framework and biostratigraphic zonation for fusulinids (North American biozones; Wahlman, 2019) and conodonts (international biozones; Henderson, 2018) for the uppermost Carboniferous through lowermost Middle Permian (Guadalupian) successions in the western U.S. that host currently proposed Wolfcampian-Leonardian boundaries (WLB; red lines). (1) The traditional WLB boundary at the base of the Petrolia Fm (dashed red line) in the Midland Basin and Eastern Shelf successions, and the newly proposed WLB (287.1 ± 4.4 Ma; solid red line) based on U-Pb carbonate ages generated by this study (red squares and conodont biostratigraphy placing it near the base of the Talpa Fm and in the middle Waggoner Ranch Fm, respectively (See Section 5.4), (2) the basal Leonardian boundary as defined in the Glass Mount type section of the boundary (~286 Ma; Ross, 1963; Wilde, 1990), (3) the WLB in the Stephen LV1 core from the Midland Basin defining the WLB boundary below the Wolfcamp A/B boundary (~288 to 287 Ma) based on conodont biostratigraphy (Kohn et al., 2019) and correlation to zircon TIMS ages from the Dn'aly Section and Midland Basin (Schmitz and Davydov, 2012; Tian et al., 2022), and (4) the WLB in Kansas defined as the contact between the Chase Group and the Sumner

Group (293.5 to 292.3 Ma; Henderson, 2018) based on the lithological change from cyclothems to red beds and evaporites, respectively.

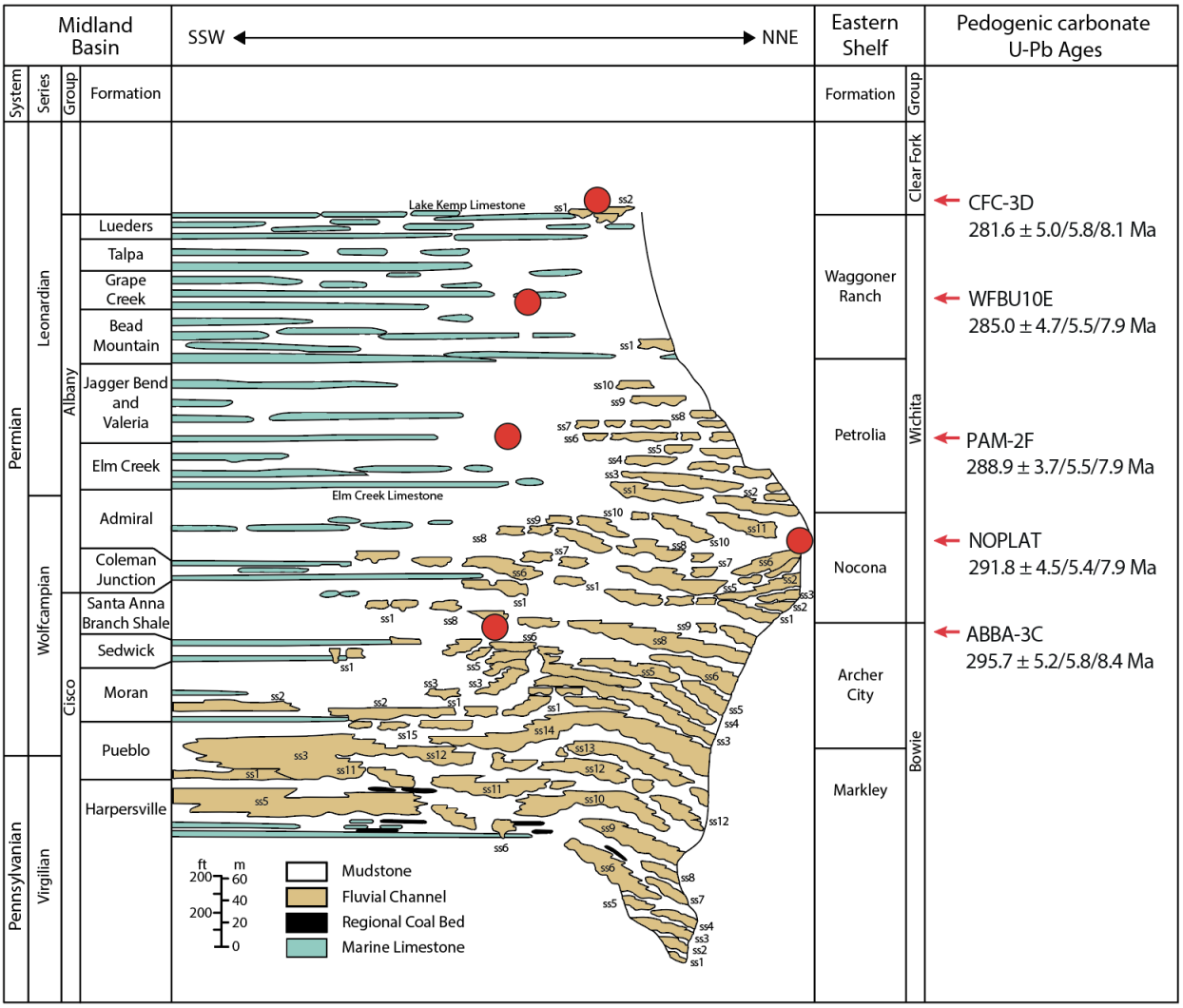

Figure 3. Generalized stratigraphy for the Carboniferous-Permian succession in the Midland Basin and Eastern Shelf, north-central Texas. Stratigraphic position of studied carbonate nodules (red-filled circle), and corresponding Bayesian modeled U-Pb ages of earliest generation calcite cements in paleosol nodules (red arrows). Figure adapted from Tabor and Montañez, 2004 and Hentz, 1988.

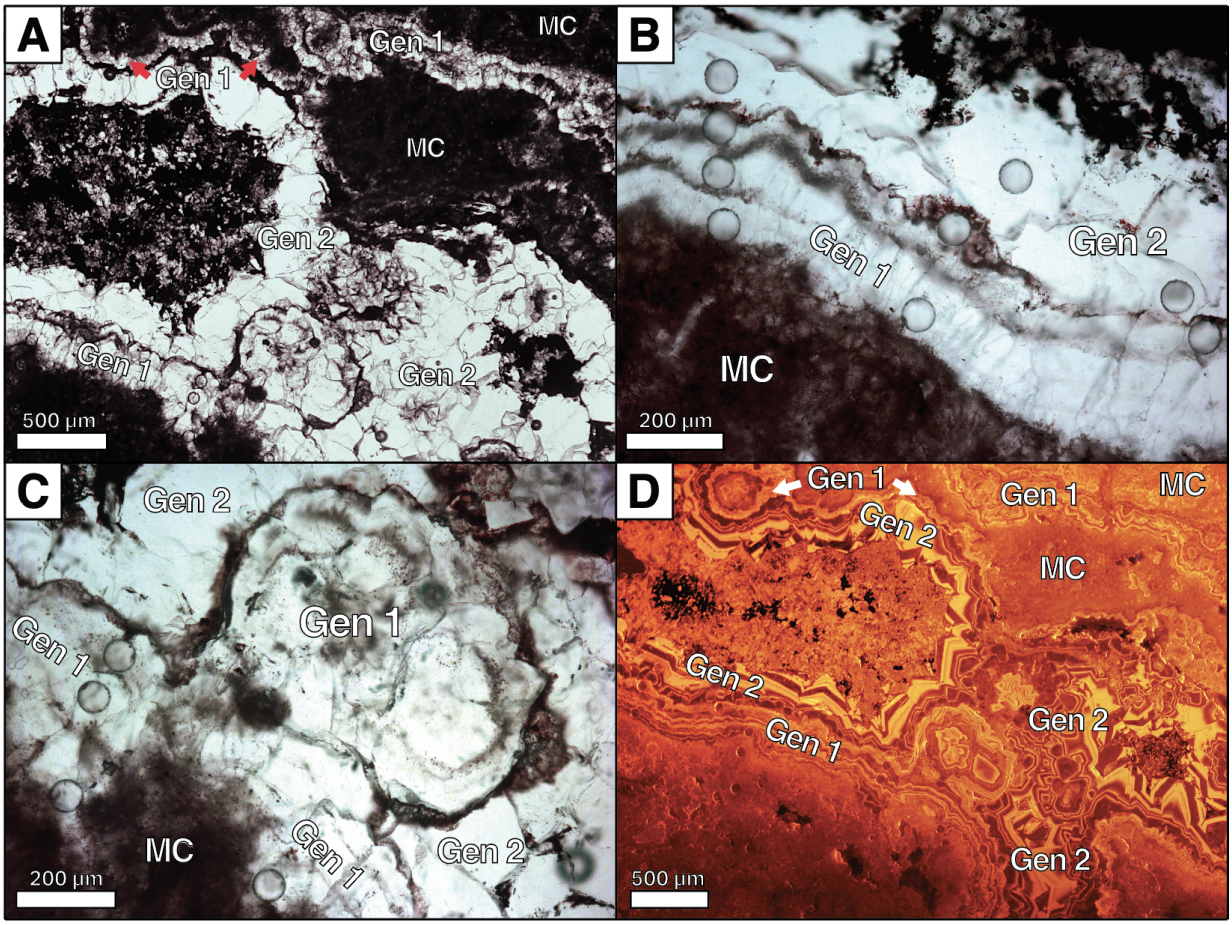

Figure 4. Photomicrographs of generation 1 and 2 calcite cements in Archer City carbonate nodules. (A) Prismatic to equant Gen 1 cements line primary porosity and rim micritic clots and intraclasts. Subrounded to equant generation 2 cements overgrow Gen 1 cements. Higher magnification images of 'A' showing (B) microcrystalline Fe-oxides incorporated in and/or overlying cement crystal terminations of Gen 1 cements, and (C) irregular thickness cements(~10 to 50 µm) of gray microcrystalline calcite overlying Gen 1 cements, interpreted as microbially mediated. Clear subrounded to equant calcite cements (Gen 2) occlude remaining porosity. (D) CL of Gen 1 and Gen 2 cements exhibiting the sequence of zonation. Gen 1: dully and medium dully luminescent, and Gen 2: NL band with two thin orange luminescent terminal bands, followed by alternating thicker bands of NL and bright (yellow) luminescence. CL reveals the discordant nature

of Gen 1 cements and the Gen 2 cements that overgrow them. Visible laser ablation pits are 65 µm in diameter. CM: Carbonate micrite.

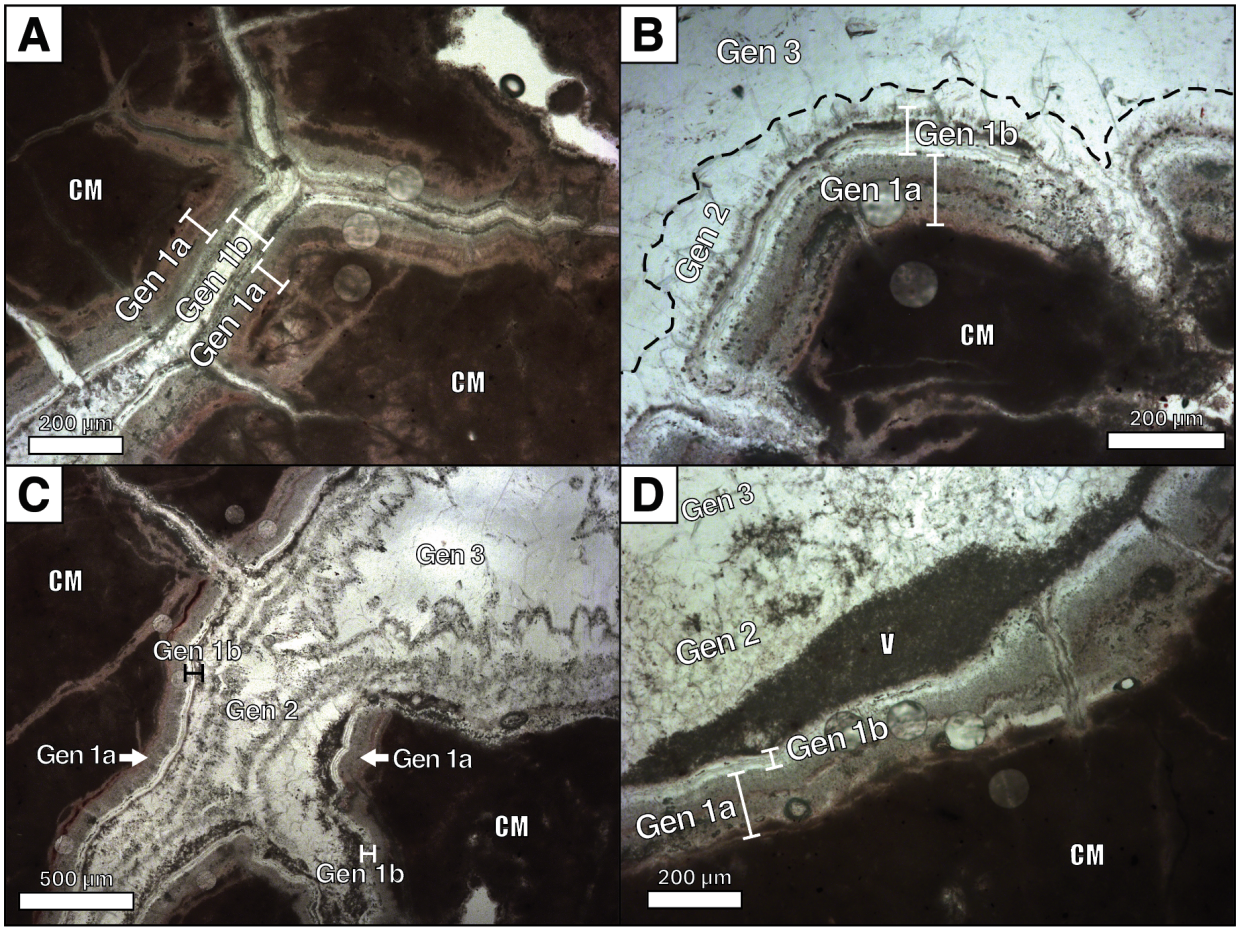

Figure 5. Photomicrographs of generation 1 through 3 calcite cements of Waggoner Ranch carbonate nodules. (A) Gen 1a fibrous cements, interpreted as calcrete, form a near isopachous layer lining primary porosity; Fe-Mn inclusions create the banded gray to pink color. Note that root casts penetrate Gen 1a and Gen 1b cements and infill them (also seen in photomicrographs B, C, and D). (B) Thin layer of clear fibrous cements with acute scalenohedral terminations (Gen 1b) overgrowing Gen 1a cements. Gen 1b cements also include intercalation of µm-scale calcrete laminations. (C) Gen 1-3 cements filling a large desiccation crack in a pedogenic nodule; Gen 2

cements occur as multiple layers of prismatic to bladed calcite with common acute scalenohedral crystal terminations. Blocky clear calcite cements (Gen 3) occlude remaining porosity. (D) Very fine crystalline micrite cement, interpreted as vadose silt (v), overlying Gen 1 cements on the downside of a primary pore. Note the irregular development of subrounded equant crystals (Gen 2) nucleated off of the vadose silt. Visible laser ablation pits are 85 μm in diameter. CM: Carbonate micrite.

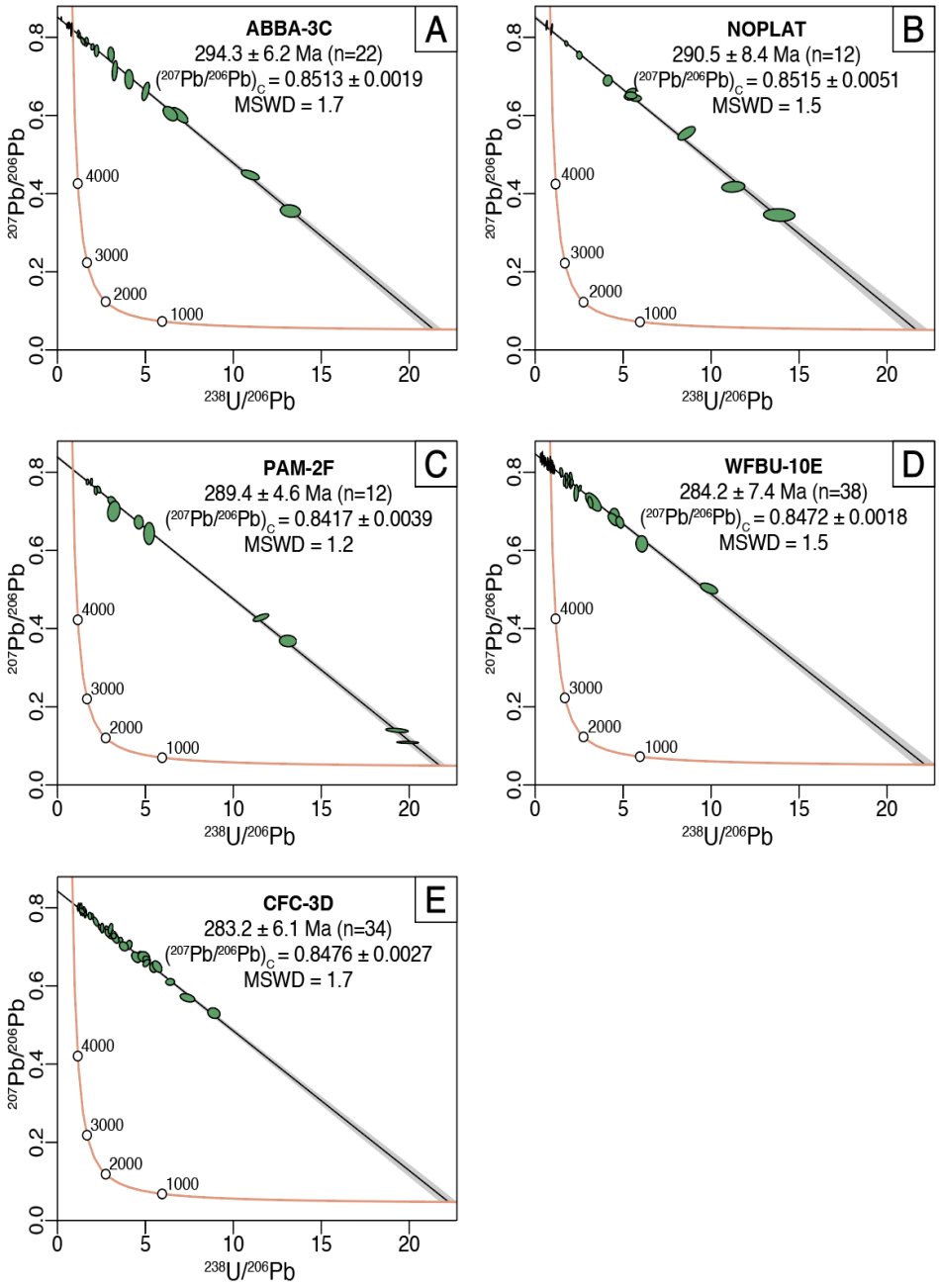

Figure 6. Tera-Wasserburg concordia plots of analyzed carbonate precipitates from the five dated pedogenic carbonate nodules. Plotted U-Pb data for Archer City calcite cements including: (A) Gen 1 from ABBA-3C, (B) Gen 1 from NOPLAT, and (C) Gen 2 from PAM-2F. Plotted U-Pb data for Waggoner Ranch calcite cements including: (D) Gen 1 from WFBU-10E, and (E) Gen 2 from CFC-3D.

Table 1. LA-ICP-MS U-Pb data for carbonate nodules from the Eastern Shelf of the Midland Basin, TX

Sample Name	Group	Formation	Isochron Age (Ma)	MSWD	$^{207}Pb/^{206}Pb$ (Pbc)*	Modeled Age (Ma)
ABBA-3C	Bowie	Archer City	294.3 ± 6.2	1.7	0.8513 ± 0.0019	296.0 ± 5.1
NoPlat-4L	Wichita	Nocona	292.7 ± 8.7	1.5	0.8515 ± 0.0051	292.5 ± 4.8
PAM-2F	Wichita	Petrolia	289.4 ± 4.6	1.2	0.8417 ± 0.0039	289.1 ± 3.8
WFBU-10E	Wichita	Waggoner Ranch	284.2 ± 7.4	1.5	0.8472 ± 0.0018	285.1 ± 4.8
CFC-3D	Clear Fork	Arroyo	283.2 ± 6.1	1.7	0.8476 ± 0.0027	281.6 ± 5.0

* $^{207}Pb/^{206}Pb$ (Pbc): Initial common lead

References Cited:

Aguirre Palafox, L.E., Möller, A., McLean, N.M., Ludvigson, G.A., Colombi, C.E., and Montañez, I.P., 2024, U-Pb Geochronology of Paleosol Carbonate Cements by LA-ICP-MS: A Proof of Concept and Strategy for Dating the Terrestrial Record: Geochemistry, Geophysics, Geosystems, v. 25, p. e2024GC011488, doi:https://doi.org/10.1029/2024GC011488.

Alnazghah, M., and Kerans, C., 2018, Late Pennsylvanian glaciation: Evidence of icehouse conditions from Canyon and cisco units, Midland Basin, Texas: Marine and Petroleum Geology, v. 94, doi:10.1016/j.marpetgeo.2018.04.004.

Alonso-Zarza, A.M., and Wright, V.P., 2010, Chapter 2 Palustrine Carbonates: Developments in Sedimentology, v. 61, p. 103–131, doi:10.1016/S0070-4571(09)06102-0.

Alonso-Zarza, A.M., 2003, Palaeoenvironmental significance of palustrine carbonates and calcretes in the geological record: Earth-Science Reviews, v. 60, doi:10.1016/S0012-8252(02)00106-X.

Barnaby, R.J., and Rimstidt, J.D., 1989, Redox conditions of calcite cementation interpreted from Mn and Fe contents of authigenic calcites: Geological Society of America Bulletin, v. 101, doi:10.1130/0016-7606(1989)101<0795:RCOCCI>2.3.CO;2.

Baumgardner, R.W., DiMichele, W.A., and Vieira, N. de S., 2016, An early Permian coastal flora dominated by Germaropteris martinsii from basinal sediments in the Midland Basin, West Texas: Palaeogeography, Palaeoclimatology, Palaeoecology, v. 459, doi:10.1016/j.palaeo.2016.07.024.

Boardman II, D.R., Wardlaw, B.R., and Nestell, M.K., 2009, Stratigraphy and Conodont Biostratigraphy of the Uppermost Carboniferous and Lower Permian from the North American Midcontinent (Part A): v. Bulletin 2.

Chen, J. et al., 2022, Marine anoxia linked to abrupt global warming during Earth's penultimate icehouse: Proceedings of the National Academy of Sciences of the United States of America, v. 119, doi:10.1073/pnas.2115231119.

Chernykh, V. V, 2006, Lower Permian conodonts in the Urals: Ekaterinburg: Institute of Geology and Geochemistry, Uralian Branch of the Russian Academy of Sciences, v. 130.

Clapham, M.E., and James, N.P., 2008, Paleoecology of early-middle permian marine communities in eastern australia: Response to global climate change in the aftermath of the late paleozoic ice age: Palaios, v. 23, doi:10.2110/palo.2008.p08-022r.

Cumberland, S.A., Douglas, G., Grice, K., and Moreau, J.W., 2016, Uranium mobility in organic matter-rich sediments: A review of geological and geochemical processes: Earth-Science Reviews, v. 159, doi:10.1016/j.earscirev.2016.05.010.

Cuney, M., 2010, Evolution of uranium fractionation processes through time: Driving the secular variation of uranium deposit types: Economic Geology, v. 105, doi:10.2113/gsecongeo.105.3.553.

Deutz, P., Montanez, I.P., and Monger, H.C., 2002, Morphology and stable and radiogenic isotope composition of pedogenic carbonates in late quaternary relict soils, New Mexico, U.S.A.: An integrated record of pedogenic overprinting: Journal of Sedimentary Research, v. 72, doi:10.1306/040102720809.

DiMichele, W.A., Bashforth, A.R., Falcon-Lang, H.J., and Lucas, S.G., 2020, Uplands, lowlands, and climate: Taphonomic megabiases and the apparent rise of a xeromorphic, drought-tolerant flora during the Pennsylvanian-Permian transition: Palaeogeography, Palaeoclimatology, Palaeoecology, v. 559, doi:10.1016/j.palaeo.2020.109965.

DiMichele, W.A., Mamay, S.H., Chaney, D.S., Hook, R.W., and Nelson, W.J., 2001, An Early Permian flora with Late Permian and Mesozoic affinities from north-central Texas: Journal of Paleontology, v. 75, doi:10.1017/s0022336000018230.

DiMichele, W.A., Tabor, N.J., Chaney, D.S., and Nelson, W.J., 2006, From wetlands to wet spots: Environmental tracking and the fate of carboniferous elements in early permian tropical fl oras: Special Paper of the Geological Society of America, v. 399, doi:10.1130/2006.2399(11).

Drost, K., Chew, D., Petrus, J.A., Scholze, F., Woodhead, J.D., Schneider, J.W., and Harper, D.A.T., 2018, An Image Mapping Approach to U-Pb LA-ICP-MS Carbonate Dating and Applications to Direct Dating of Carbonate Sedimentation: Geochemistry, Geophysics, Geosystems, v. 19, doi:10.1029/2018GC007850.

Falcon-Lang, H.J. et al., 2015, Early Permian (Asselian) vegetation from a seasonally dry coast in western equatorial Pangea: Paleoecology and evolutionary significance: Palaeogeography, Palaeoclimatology, Palaeoecology, v. 433, doi:10.1016/j.palaeo.2015.05.010.

Gauthier-Lafaye, F., Weber, F., and Ohmoto, H., 1989, Natural fission reactors of Oklo: Economic Geology, v. 84, doi:10.2113/gsecongeo.84.8.2286.

Godeau, N., Deschamps, P., Guihou, A., Leonide, P., Tendil, A., Gerdes, A., Hamelin, B., and Girard, J.P., 2018, U-Pb dating of calcite cement and diagenetic history in microporous carbonate reservoirs: Case of the Urgonian Limestone, France: Geology, v. 46, doi:10.1130/G39905.1.

Griffis, N., Tabor, N.J., Stockli, D., and Stockli, L., 2023, The Far-Field imprint of the late Paleozoic Ice Age, its demise, and the onset of a dust-house climate across the Eastern Shelf of the Midland Basin, Texas: Gondwana Research, v. 115, doi:10.1016/j.gr.2022.11.004.

Gulbranson, E.L. et al., 2022, U–Pb Geochronology and Stable Isotope Geochemistry of Terrestrial Carbonates, Lower Cretaceous Cedar Mountain Formation, Utah: Implications for Synchronicity of Terrestrial and Marine Carbon Isotope Excursions: Geosciences (Switzerland), v. 12, doi:10.3390/geosciences12090346.

Henderson, C.M., 2018, Permian conodont biostratigraphy: Geological Society, London, Special Publications, v. 450, p. 119–142, doi:10.1144/SP450.9.

Henderson, C., Shen, S., Gradstein, F., and Agterberg, F.P., 2020, The Permian Period: , p. 875–902, doi:10.1016/B978-0-12-824360-2.00024-3.

Hentz, T.F., 1988, Lithostratigraphy and paleoenvironments of Upper Paleozoic continental red beds, North-central Texas: Bowie (new) and Wichita (Revised) Groups: Bureau of Economic Geology, Report of Investigation, v. 170.

Hill, C.A., Polyak, V.J., Asmerom, Y., and P. Provencio, P., 2016, Constraints on a Late Cretaceous uplift, denudation, and incision of the Grand Canyon region, southwestern Colorado Plateau, USA, from U-Pb dating of lacustrine limestone: Tectonics, v. 35, doi:10.1002/2016TC004166.

Jochum, K.P. et al., 2011, Determination of reference values for NIST SRM 610-617 glasses following ISO guidelines: Geostandards and Geoanalytical Research, v. 35, doi:10.1111/j.1751-908X.2011.00120.x.

Jurikova, H. et al., 2025, Rapid rise in atmospheric CO2 marked the end of the Late Palaeozoic Ice Age: Nature Geoscience, v. 18, p. 91–97, doi:10.1038/s41561-024-01610-2.

Kelly, S.D., Rasbury, E.T., Chattopadhyay, S., Kropf, A.J., and Kemner, K.M., 2006, Evidence of a stable uranyl site in ancient organic-rich calcite: Environmental Science and Technology, v. 40, doi:10.1021/es051970v.

Kohn, J., Barrick, J.E., Wahlman, G.P., and Baumgardner, R., 2019, Late Pennsylvanian (Virgilian) to early Permian (Leonardian) conodont biostratigraphy of the ‘“wolfcamp

shale,"' northern midland basin, Texas: SEPM Special Publications, v. 111, doi:10.2110/sepmsp.111.11.

Koll, R.A., and DiMichele, W.A., 2021, Dominance-diversity architecture of a mixed hygromorphic-to-xeromorphic flora from a botanically rich locality in western equatorial Pangea (lower Permian Emily Irish site, Texas, USA: Palaeogeography, Palaeoclimatology, Palaeoecology, v. 563, doi:10.1016/j.palaeo.2020.110132.

Lawton, T.F., Blakey, R.C., Stockli, D.F., and Liu, L., 2021, Late Paleozoic (Late Mississippian–Middle Permian) sediment provenance and dispersal in western equatorial Pangea: Palaeogeography, Palaeoclimatology, Palaeoecology, v. 572, doi:10.1016/j.palaeo.2021.110386.

Layzell, A.L., Ludvigson, G.A., Smith, J.J., and Mandel, R.D., 2023, Using the factors of soil formation to assess stable carbon isotope disequilibrium in late Pleistocene (MIS 3) buried soils of the Great Plains, North America: Palaeogeography, Palaeoclimatology, Palaeoecology, v. 620, doi:10.1016/j.palaeo.2023.111574.

Leary, R.J. et al., 2020, Provenance of Pennsylvanian-Permian sedimentary rocks associated with the Ancestral Rocky Mountains orogeny in southwestern Laurentia: Implications for continental-scale Laurentian sediment transport systems: Lithosphere, v. 12, doi:10.1130/L1115.1.

Li, Q., Parrish, R.R., Horstwood, M.S.A., and McArthur, J.M., 2014, U-Pb dating of cements in Mesozoic ammonites: Chemical Geology, v. 376, doi:10.1016/j.chemgeo.2014.03.020.

Liu, L., and Stockli, D.F., 2019, U-Pb ages of detrital zircons in lower permian sandstone and siltstone of the Permian Basin, west Texas, USA: Evidence of dominant Gondwanan and peri-Gondwanan sediment input to Laurentia: Bulletin of the Geological Society of America, v. 132, p. 245–262, doi:10.1130/B35119.1.

Looy, C. V., 2007, Extending the range of derived late paleozoic conifers: Lebowskia gen. nov. (Majonicaceae): International Journal of Plant Sciences, v. 168, doi:10.1086/518256.

Looy, C. V., and Stevenson, R.A., 2014, Earliest occurrence of autorotating seeds in conifers: The Permian (Kungurian-Roadian) Manifera talaris gen. et sp. nov: International Journal of Plant Sciences, v. 175, doi:10.1086/676973.

Lucas, S.G., Henderson, C.M., Krainer, K., Barrick, J.E., and Reynolds, S.J., 2024, Early Permian seaways in the American Southwest: Journal of South American Earth Sciences, v. 148, p. 105176.

Lucas, S., Henderson, C., Barrick, J., and Krainer, K., 2022, Conodonts and the correlation of the Lower Permian Yeso Group, New Mexico, USA, *in* Stratigraphy, v. 19, p. 77–94, doi:10.29041/strat.19.2.01.

Marchetti, L. et al., 2022, The Artinskian Warming Event: an Euramerican change in climate and the terrestrial biota during the early Permian: Earth-Science Reviews, v. 226, doi:10.1016/j.earscirev.2022.103922.

Matthaeus, W.J., Macarewich, S.I., Richey, J., Montañez, I.P., Mcelwain, J.C., White, J.D., Wilson, J.P., and Poulsen, C.J., 2023, A Systems Approach to Understanding How Plants Transformed Earth's Environment in Deep Time: Annual Review of Earth and Planetary Sciences, v. 51, doi:10.1146/annurev-earth-080222-082017.

Methner, K., Mulch, A., Fiebig, J., Wacker, U., Gerdes, A., Graham, S.A., and Chamberlain, C.P., 2016, Rapid Middle Eocene temperature change in western North America: Earth and Planetary Science Letters, v. 450, doi:10.1016/j.epsl.2016.05.053.

Milodowski, A.E., Bath, A., and Norris, S., 2018, Palaeohydrogeology using geochemical, isotopic and mineralogical analyses: Salinity and redox evolution in a deep groundwater system through Quaternary glacial cycles: Applied Geochemistry, v. 97, doi:10.1016/j.apgeochem.2018.07.008.

Montañez, I.P., McElwain, J.C., Poulsen, C.J., White, J.D., Dimichele, W.A., Wilson, J.P., Griggs, G., and Hren, M.T., 2016, Climate, pCO2 and terrestrial carbon cycle linkages during late Palaeozoic glacial-interglacial cycles: Nature Geoscience, v. 9, p. 824–828, doi:10.1038/ngeo2822.

Montañez, I.P., Tabor, N.J., Niemeier, D., DiMichele, W.A., Frank, T.D., Fielding, C.R., Isbell, J.L., Birgenheier, L.P., and Rygel, M.C., 2007, CO2-forced climate and vegetation instability during late paleozoic deglaciation: Science, v. 315, doi:10.1126/science.1134207.

Montañez, I.P., 2022, Current synthesis of the penultimate icehouse and its imprint on the Upper Devonian through Permian stratigraphic record, *in* Geological Society Special Publication, v. 512, doi:10.1144/SP512-2021-124.

Myers, D.A., 1968, Schwagerina crassitectoria Dunbar and Skinner, 1937, a fusulinid from the upper part of the Wichita Group, Lower Permian, Coleman County, Texas: US Geological Survey, Professional Paper, v. 600, p. 133–139.

Parrish, R.R., Parrish, C.M., and Lasalle, S., 2018, Vein calcite dating reveals Pyrenean orogen as cause of Paleogene deformation in southern England: Journal of the Geological Society, v. 175, doi:10.1144/jgs2017-107.

Paton, C., Hellstrom, J., Paul, B., Woodhead, J., and Hergt, J., 2011, Iolite: Freeware for the visualisation and processing of mass spectrometric data: Journal of Analytical Atomic Spectrometry, v. 26, doi:10.1039/c1ja10172b.

Powell, M.G., 2005, Climatic basis for sluggish macroevolution during the late Paleozoic ice age: Geology, v. 33, doi:10.1130/G21155.1.

Ramezani, J., Schmitz, M.D., Davydov, V.I., Bowring, S.A., Snyder, W.S., and Northrup, C.J., 2007, High-precision U-Pb zircon age constraints on the Carboniferous-Permian boundary in the southern Urals stratotype: Earth and Planetary Science Letters, v. 256, doi:10.1016/j.epsl.2007.01.032.

Rasbury, E.T., Hanson, G.N., Meyers, W.J., and Saller, A.H., 1997, Dating of the time of sedimentation using U-Pb ages for paleosol calcite: Geochimica et Cosmochimica Acta, v. 61, doi:10.1016/S0016-7037(97)00043-4.

Rasbury, E.T., Meyers, W.J., Hanson, G.N., Goldstein, R.H., and Saller, A.H., 2000, Relationship of uranium to petrography of caliche paleosols with application to precisely dating the time of sedimentation: Journal of Sedimentary Research, v. 70, doi:10.1306/2DC4092B-0E47-11D7-8643000102C1865D.

Rembe, J., Zhou, R., Sobel, E.R., Kley, J., Chen, J., Zhao, J.-X., Feng, Y., and Howard, D.L., 2022, Calcite U–Pb dating of altered ancient oceanic crust in the North Pamir, Central Asia: Geochronology, v. 4, p. 227–250, doi:10.5194/gchron-4-227-2022.

Richey, J.D., Montañez, I.P., Goddéris, Y., Looy, C. V., Griffis, N.P., and Dimichele, W.A., 2020, Influence of temporally varying weatherability on CO2-climate coupling and ecosystem change in the late Paleozoic: Climate of the Past, v. 16, p. 1759–1775, doi:10.5194/cp-16-1759-2020.

Ritter, S.M., 1995, Upper Missourian-Lower Wolfcampian (Upper Kasimovian-Lower Asselian) conodont biostratigraphy of the midcontinent, USA: Journal of Paleontology, v. 69, doi:10.1017/S0022336000038129.

Roberts, N.M.W. et al., 2020, Laser ablation inductively coupled plasma mass spectrometry (LA-ICP-MS) U-Pb carbonate geochronology: Strategies, progress, and limitations: Geochronology, v. 2, doi:10.5194/gchron-2-33-2020.

Roberts, N.M.W., Rasbury, E.T., Parrish, R.R., Smith, C.J., Horstwood, M.S.A., and Condon, D.J., 2017, A calcite reference material for LA-ICP-MS U-Pb geochronology: Geochemistry, Geophysics, Geosystems, v. 18, doi:10.1002/2016GC006784.

Rochín-Bañaga, H., Gastaldo, R.A., Davis, D.W., Neveling, J., Kamo, S.L., Looy, C. V., and Geissman, J.W., 2023, U-Pb dating of pedogenic calcite near the Permian−Triassic boundary, Karoo Basin, South Africa: Geological Society of America Bulletin, doi:10.1130/b36968.1.

Ross, C.A., and Ross, J.R.P., 2003, Fusulinid sequence evolution and sequence extinction in Wolfcampian and Leonardian series (lower Permian), glass mountains, West Texas: Rivista Italiana di Paleontologia e Stratigrafia, v. 109.

Rusakov, A., Makeev, A., Khokhlova, O., Kust, P., Lebedeva, M., Chernov, T., Golyeva, A., Popov, A., Kurbanova, F., and Puzanova, T., 2019, Paleoenvironmental reconstruction based

on soils buried under Scythian fortification in the southern forest-steppe area of the East European Plain: Quaternary International, v. 502, doi:10.1016/j.quaint.2018.05.016.

Schmitz, M.D., and Davydov, V.I., 2012, Quantitative radiometric and biostratigraphic calibration of the Pennsylvanian-Early Permian (Cisuralian) time scale and pan-Euramerican chronostratigraphic correlation: Bulletin of the Geological Society of America, v. 124, p. 549–577, doi:10.1130/B30385.1.

Simon, S.S.T., Gibling, M.R., Dimichele, W.A., Chaney, D.S., and Koll, R., 2018, An exhumed fine-grained meandering channel in the lower Permian Clear Fork Formation, north-central Texas, *in* Fluvial Meanders and Their Sedimentary Products in the Rock Record, doi:10.1002/9781119424437.ch6.

Soreghan, M.J., Swift, M.M., and Soreghan, G.S., 2018, Provenance of Permian eolian and related strata in the North American midcontinent: Tectonic and climatic controls on sediment dispersal in Western tropical Pangea: Special Paper of the Geological Society of America, v. 540, doi:10.1130/2018.2540(28).

Stanley, S.M., and Powell, M.G., 2003, Depressed rates of origination and extinction during the late Paleozoic ice age: A new state for the global marine ecosystem: Geology, v. 31, doi:10.1130/G19654R.1.

Steinthorsdottir, M., Montañez, I.P., Royer, D.L., Mills, B.J.W., and Hönisch, B., 2024, Phanerozoic atmospheric CO2 reconstructed with proxies and models: Current understanding and future directions, *in* Reference Module in Earth Systems and Environmental Sciences, doi:10.1016/b978-0-323-99762-1.00074-7.

Stojanović, M.D., Stevanović, D.R., Milojković, J. V., Grubišić, M.S., and Ileš, D.A., 2010, Phytotoxic effect of the uranium on the growing up and development the plant of corn: Water, Air, and Soil Pollution, v. 209, doi:10.1007/s11270-009-0208-4.

Tabor, N.J., DiMichele, W.A., Montañez, I.P., and Chaney, D.S., 2013, Late Paleozoic continental warming of a cold tropical basin and floristic change in western Pangea: International Journal of Coal Geology, v. 119, doi:10.1016/j.coal.2013.07.009.

Tabor, N.J., and Poulsen, C.J., 2008, Palaeoclimate across the Late Pennsylvanian-Early Permian tropical palaeolatitudes: A review of climate indicators, their distribution, and relation to palaeophysiographic climate factors: Palaeogeography, Palaeoclimatology, Palaeoecology, v. 268, doi:10.1016/j.palaeo.2008.03.052.

Tabor, N.J., and Montanez, I.P., 2004, Morphology and distribution of fossil soils in the Permo-Pennsylvanian Wichita and Bowie Groups, north-central Texas, USA: Implications for western equatorial Pangean palaeoclimate during icehouse-greenhouse transition: Sedimentology, v. 51, p. 851–884, doi:10.1111/j.1365-3091.2004.00655.x.

Tandy, S., Brittain, S.R., Grail, B.M., Mcleod, C.W., Paterson, E., and Tomos, A.D., 2013, Fine scale measurement and mapping of uranium in soil solution in soil and plant-soil microcosms, with special reference to depleted uranium: Plant and Soil, v. 368, doi:10.1007/s11104-012-1526-7.

Tian, H., Fan, M., Valencia, V.A., Chamberlain, K., Waite, L., Stern, R.J., and Loocke, M., 2022, Rapid early Permian tectonic reorganization of Laurentia's plate margins: Evidence from volcanic tuffs in the Permian Basin, USA: Gondwana Research, v. 111, p. 76–94, doi:https://doi.org/10.1016/j.gr.2022.07.003.

Vermeesch, P., 2018, IsoplotR: A free and open toolbox for geochronology: Geoscience Frontiers, v. 9, doi:10.1016/j.gsf.2018.04.001.

Wahlman, G.P., 2019, Pennsylvanian and Lower Permian fusulinid biostratigraphy of the Permian Basin region, southwestern USA, *in* Anatomy of a Paleozoic basin: the Permian Basin, USA, v. 1, p. 167–227.

Wang, X.D., Wang, X.J., Zhang, F., and Zhang, H., 2006, Diversity patterns of Carboniferous and Permia rugose corals in South China: Geological Journal, v. 41, doi:10.1002/gj.1041.

Wardlaw, B.R., 2005, Age assignment of the Pennsylvanian-Early Permian succession of north central Texas: Permophiles, v. 46, p. 21–22.

Wardlaw, B.R., and Nestell, M.K., 2019, Conodont biostratigraphy of Lower Permian (Wolfcampian-Leonardian) stratotype sections of the Glass and Del Norte Mountains, West Texas, USA: Anatomy of a Paleozoic basin: the Permian Basin, USA, v. 1, p. 229–249.

Wardlaw, B., and Nestell, M., 2014, The first appearance of Streptognathodus isolatus in the Permian of Texas: Permophiles, p. 17–20.

Wilde, G.L., 1990, Practical fusulinid zonation the species concept; with Permian Basin emphasis: West Texas Geological Society Bulletin, v. 29.

Wright, V.P., Platt, N.H., Marriott, S.B., and Beck, V.H., 1995, A classification of rhizogenic (root-formed) calcretes, with examples from the Upper Jurassic-Lower Cretaceous of Spain and Upper Cretaceous of southern France: Sedimentary Geology, v. 100, doi:10.1016/0037-0738(95)00105-0.

Zhou, J., and Chafetz, H.S., 2009, The genesis of late Quaternary caliche nodules in Mission Bay, Texas: Stable isotopic compositions and palaeoenvironmental interpretation: Sedimentology, v. 56, doi:10.1111/j.1365-3091.2008.01039.x.

Zhu, L., and Tabor, N.J., 2021, Verification of regional-to-global scale environmental factors in paleosol stable carbon isotope ratios through the lower Permian succession of north-central Texas, U.S.A.: Palaeogeography, Palaeoclimatology, Palaeoecology, v. 582, doi:10.1016/j.palaeo.2021.110646.

Supplementary Material

Publication	Aguirre-Palafox et al. 2025, in prep.
Laboratory & Sample Preparation	
Laboratory name	The University of Kansas, Isotope Geochemistry Laboratories
Sample type/mineral	calcite
Sample preparation	polished thick sections
Imaging	reflected, transmitted light
Laser ablation system	
Make, Model & type	Arf excimer 193 nm, Photon Machines Analyte G2, Atlex300
Ablation cell & volume	Helex 2, two-volume cell
Laser wavelength (nm)	193
Pulse width (ns)	5
Fluence (J.cm-2)	3
Repetition rate (Hz)	10 (85 µm circles) and 12 (65 µm circles)
Spot size (um)	65 and 85 µm circles
Carrier gas	He, 1.1 l/min, Ar, 1.4 l/min
Ablation duration (secs)	30
ICP-MS Instrument	
Make, Model & type	Thermo Element2 magnetic sector field ICP-MS
RF power (W)	1350
Make-up gas flow (l/min)	Ar, 1.35 l/min
sampling depth (z position of torch)	4.8
Detection system	single detector, counting
Masses measured	Pb206, Pb207, Pb208, Th232, U238
Integration time per peak (ms)	Pb206, Pb207, U238: 80 ms; Pb208, Th232: 8 ms
Total method time	46
Gas blank (s)	15
IC Dead time (ns)	8
UO+/U+ (%)	0.2
238+/232Th+	0.8
Data Processing	
Reference Material info	NIST 612 (Jochum et al. 2011), DBTL (Hill et all. 2016)
238U/238U	137.88
Data processing package used / Correction for LIEF	IGOR PRO, Iolite 2.5, U-PbGeochron3 for Pb, in-house Excel for U-Pb
Common-Pb correction, composition, uncertainty	none
Quality control / Validation	WC1 (Roberts et al. 2017)

Table S1. LA-ICP-MS methods data used in the U-Pb analyses of the Eastern Shelf succession carbonate nodules.

Supplementary Material References

Hill, C.A., Polyak, V.J., Asmerom, Y., and P. Provencio, P., 2016, Constraints on a Late Cretaceous uplift, denudation, and incision of the Grand Canyon region, southwestern Colorado Plateau, USA, from U-Pb dating of lacustrine limestone: Tectonics, v. 35, doi:10.1002/2016TC004166.

Jochum, K.P. et al., 2011, Determination of reference values for NIST SRM 610-617 glasses following ISO guidelines: Geostandards and Geoanalytical Research, v. 35, doi:10.1111/j.1751-908X.2011.00120.x.

Roberts, N.M.W., Rasbury, E.T., Parrish, R.R., Smith, C.J., Horstwood, M.S.A., and Condon, D.J., 2017, A calcite reference material for LA-ICP-MS U-Pb geochronology: Geochemistry, Geophysics, Geosystems, v. 18, doi:10.1002/2016GC006784.

Chapter 3: U-Pb dating of vertebrate fossil calcite cements, Ischigualasto Fm, NW Argentina

Abstract

Direct dating of fossil vertebrates is difficult due to complex histories of radiogenic isotope (e.g., uranium) and rare earth element (REE) uptake over time and chemical alteration during fossilization and after burial. A strategy to circumvent these limitations and better approximate the start of the fossilization process is to date material associated with fossil bones from which a meaningful date can be obtained and accurately interpret the date in a geologic context. LA-ICP-MS U-Pb carbonate geochronology has been applied to dating fossils by targeting carbonates precipitated in fossilized material, but results have been inconsistent in part due to limited understanding of the paragenesis of the carbonate precipitates prior to LA-ICP-MS analyses. In this study, we examine the U-Pb systematics and potential for U-Pb dating of calcite cements precipitated both within the primary porosity of fossil bone and fractures that formed during early burial of six bone fossils from the Late Triassic Ischigualasto Fm of northwest Argentina. A cement micro-stratigraphy for each sample guided the LA-ICP-MS U-Pb analyses and further age interpretations. We interpret the U-Pb ages from these cements to estimate the timing of calcite precipitation within the vadose zone before the bone material transitioned into the shallow phreatic zone. Based on depositional rates and a lack of evidence for U-Pb open-system behavior in the analyzed cements, we infer that the timing of calcite precipitation is close to the time of death and burial of the specimens. The U-Pb ages for the calcite cements are comparable to existing radioisotopic ages of volcanic deposits and calcite cements in carbonate nodules from paleosols intercalated within the succession. This study marks the first successful indirect dating of basal Eoraptor and Herrerasaurus dinosaurs from the Ischigualasto Fm.

1. Introduction

Direct dating of fossil vertebrates in deep time is typically challenging due to complex chemical alteration of bone material during burial and complicated histories of radiogenic isotope uptake over time (e.g., Koenig et al., 2009; Herwartz et al., 2011; Grün and Stringer, 2023). In the years to thousands of years after the death of an organism, uranium (U) and other trace elements diffuse into bone and/or are sorbed onto recrystallized hydroxyapatite during the fossilization process (e.g., Millard and Hedges, 1996; Pike et al., 2002). Over thousands to millions of years, most fossilized bone is recrystallized during burial, leading to periods of radiogenic isotope and REE (rare earth element) uptake and open-system behavior that, in turn, have yielded U-Pb and Lu-Hf dates of individual fossil bone samples of a wide range that are considerably younger than anticipated based on known chronostratigraphic ages of the given sedimentary strata hosting the fossil samples (Koenig et al., 2009; Fassett et al., 2011; Herwartz et al., 2011). Without a robust understanding of the trace-element uptake, recrystallization, and chemical alteration histories of individual bone samples, direct dating of fossilized bone remains challenging. Strategies to better approximate the start of the fossilization process after the death of an organism without directly dating the bone material provide the best path forward. First, this requires targeting material associated with fossils from which a meaningful date can be obtained, and secondly, accurately interpreting the date in a geologic context.

Over the past decade, a few studies have focused on applying LA-ICP-MS U-Pb carbonate geochronology to dating fossil specimens in deep time by targeting carbonates precipitated in fossilized material (e.g., cements infilling fossil porosity; Li et al., 2014; Qi et al., 2024; Rochin-Bañaga et al., 2024). One advantage of this strategy is the abundance of carbonate cements

associated with fossilized specimens in the marine and terrestrial records. Another significant advantage of targeting these carbonate cements, instead of the fossilized material itself, is the myriad of studies documenting the successful application of LA-ICP-MS U-Pb carbonate geochronology to constrain the timing of carbonate precipitation and diagenesis in a given stratigraphic succession or sedimentary basin (e.g., Godeau et al., 2018; Rasbury et al., 2021; Gulbranson et al., 2022; Roberts & Holdsworth, 2022). This success is driven by studies that introduced fast and accurate methods for dating carbonates (e.g., Drost et al., 2018), access to a well-calibrated series of reference carbonate standards (e.g., Hill et al., 2016; Roberts et al., 2017; Guillong et al., 2020) and new field and laboratory strategies developed for carbonate-specific samples that increase their successful dating potential (e.g., Guillong et al., 2020; Montano et al., 2021, 2022; Rasbury et al., 2021, 2023; Roberts et al., 2020; Aguirre-Palafox et al., 2024). However, a crucial problem of any U-Pb carbonate geochronology study is accurately interpreting a carbonate date in a geologic context. Li et al. (2014) interpreted the ages for early-diagenetic fringing cements precipitated in the cavities of Mesozoic ammonites to represent late-diagenesis alteration of the early cements given the calculated ages are 10 to 20 Myr younger than expected based on biostratigraphic constraints. The age of a sauropod fossil from South China presented by Qi et al. (2024) was compared with maximum depositional ages of detrital zircons from the host sandstone, leading the authors to conclude that the calcite cements precipitated soon after the death of the sauropod. The next step in accurately interpreting dates in a geologic context is finding dateable carbonate cements that can be characterized within a well-defined diagenetic paragenetic framework, as has been documented for paleosol carbonate nodules (Aguirre-Palafox et al., 2024; 2025, in prep).

In this study, we examine the U-Pb systematics and potential for U-Pb dating of calcite cements precipitated both within the primary porosity of fossil bone and within fractures that formed during early burial of six vertebrate bones. The samples include five dinosaurs and one archosaur collected from the Late Triassic Ischigualasto Fm of northwest Argentina. We compare the carbonate U-Pb chronology to published zircon and sanidine geochronology from volcanic ashes intercalated with the fossil-bearing succession (Rogers et al., 1993; Martínez et al, 2011; Colombi et al., 2021). A cement micro-stratigraphy for each sample guided the LA-ICP-MS U-Pb analyses and further age interpretations. We show that U-Pb isotopic signatures vary across the analyzed generations of carbonate precipitates and document the importance of interpreting the ablation analyses in a paragenetic context. We interpret the U-Pb ages from calcite cements in fossilized bone and fracture porosity to estimate the timing of calcite precipitation within the vadose zone, before the initial transition of the bone material from the vadose into the shallow phreatic zone. We infer that the timing of calcite precipitation is close to the time of death and burial of the specimens, based on depositional rates in this section of the Ischigualasto Fm, and the lack of evidence for U-Pb open-system behavior in the analyzed cements.

The U-Pb ages for the calcite cements precipitated within bone and fracture porosity are comparable to existing radioisotopic ages of volcanic ashes and calcite cements in carbonate nodules from paleosols intercalated within the succession (Aguirre-Palafox et al., 2024). This study marks the first successful indirect dating of basal Dinosauria and Archosauria samples from the Ischigualasto Fm, a key succession for interrogating the origin of the rapid emergence and diversification of early dinosaurs and environmental perturbations in southern Pangea during the Late Triassic.

2. Geologic Setting and Sample Selection

The Ischigualasto Fm of northwestern Argentina is a paleosol and vertebrate-rich succession deposited in a continental rift basin during the late Triassic through Jurassic (Fig. 1). The Ischigualasto Fm consists of 400–700 m of laminated to thinly bedded mudstones and siltstones intercalated with fine- to coarse-grained stratified sandstones and conglomerates (Fig. 2) that are interpreted as floodplain and fluvial channel-filling deposits, respectively. Volcanic ashes are intercalated throughout the succession (Colombi et al., 2017; Currie et al., 2009). Carbonate-bearing paleosols (Tabor et al., 2006) are developed in the lower half of succession along the basin axis and throughout basin margin successions. The Ischigualasto Fm has been the target of many studies given its high fossil preservation and abundance and diversity of tetrapod fossils (with more than 5000 specimens collected to date). These include mammal-like cynodonts, archosauromorphs, non-dinosaur dinosauromorphs, dicynodonts, amphibians and some of the best-known early dinosaurs (e.g., Rogers et al., 1993; Martinez et al., 2011, Desojo et al., 2020), as well as macro and micro paleofloral assemblages (e.g., Artabe et al., 2001; César and Colombi, 2013; Colombi et al., 2017). Additionally, the Ischigualasto Fm is a critical succession for interrogating the origin of the rapid emergence and diversification of early dinosaurs and CO_2- and climate-driven environmental perturbations in southern Pangea during the Late Triassic (e.g., Rogers et al., 1993; Martínez et al., 2011, 2012; Desojo et al., 2020; Colombi et al., 2021; in prep., Mancuso et al., 2022).

For this study, six samples from the La Peña and Canchas de Bochas members (Fig. 2) were selected for study based on their stratigraphic position and proximity to published sanidine and plagioclase $^{40}Ar/^{39}Ar$ and zircon U-Pb ages for intercalated volcanic ashes (Rogers et al., 1993; Martinez et al., 2011, Colombi et al., 2021), and carbonate U-Pb ages of carbonate nodules from

intercalated paleosols. Sanidine and plagioclase $^{40}Ar/^{39}Ar$ ages from Martínez et al. (2011) and Rogers et al. (1993), were calibrated by Martínez et al. (2011) to the $^{40}Ar/^{39}Ar$ geochronology parameters of Renne et al. (2010). The fossil bones samples used in this study(Fig. 2) are bracketed by (a) the "Herr Toba" bentonite 20 m above the base of the Ischigualasto Fm with a calibrated $^{40}Ar/^{39}Ar$ sanidine plateau age of 231.4 ± 0.3 Ma (±2σ; Rogers et al., 1993; Martínez et al., 2011), (b) a dated tuff deposit 310 m above the base of the Ischigualasto Fm with a CA-TIMS U-Pb zircon age of 228.91 ± 0.14 Ma (±2σ; Colombi et al., 2021) and (c) the "Jach Toba" bentonite 630 m above the base of the Ischigualasto Fm with a calibrated $^{40}Ar/^{39}Ar$ plagioclase age of 225.9 ± 0.9 Ma (±2σ; Martínez et al., 2011). The studied samples are further bracketed by (d) a carbonate nodule (ISCH-107) collected from a Calcisol 107 m above the base of the Ischigualasto Fm in the Cancha de Bochas Mbr with a U-Pb carbonate age of 230.5 ± 2.2 Ma (±2σ; Aguirre-Palafox et al., 2024), (e) a carbonate nodule (ISCH-288) collected from a compound paleosol in the Valle de la Luna Mbr 288 m above the base of the Ischigualasto Fm and that yields a U-Pb carbonate age of 233.6 ± 3.9 Ma (±2σ; Aguirre-Palafox et al., 2024), and (f) a carbonate nodule (ISCH-251) collected from a calcic Argillisol 359 m above the base of the Ischigualasto Fm with a U-Pb carbonate age of 228.4 ± 5.0 Ma (±2σ; Aguirre-Palafox et al., 2024).

3. Materials and Methods

3.1 Carbonate petrography

Polished thick sections (~250 μm thick) were made for four samples (Bone # 03, Bone #05, Bone #14, Bone #206) and polished round epoxy mounts were made for the two additional samples (373-Herrerasaurus and 512-Eoraptor). The thick sections and epoxy mounts were studied

petrographically under plane-polarized light and by cathodoluminescence (CL). A cement microstratigraphy (i.e., paragenesis) was developed for each sample based on observed calcite crystal morphologies, cross-cutting relationships, spatial relationships with the vertebrate fossil, and CL zonation.

3.2 U-Pb carbonate geochronology

In situ U-Pb analyses via LA-ICP-MS of the four polished thick sections and two round epoxy mounts were carried out in two sessions at the University of Kansas Isotope Geochemistry Laboratories. Analyses were performed using a Photon Machines Analyte G2 193 nm ArF excimer laser ablation system connected to a Thermo Scientific Element2 ICP-MS. Laser ablation was carried out using a 3.0 J/cm^2 fluency and a 10 Hz repetition rate for 30 seconds, creating circular 85 μm diameter ablation pits. Ablated material was carried to the ICP-MS in helium gas with a 1.1 l/min combined flow rate. Targeted areas of interest in each sample were observed using the laser's built-in camera in transmitted and reflected light and cross-referenced with spatial maps of the calcite cement microstratigraphy of each sample. Downhole fractionation, Pb isotopic fractionation and drift, and uncertainty propagation were corrected by bracketing measurements of unknowns with NIST 612 and NIST 614 glass reference material (Jochum et al., 2011) using Iolite software (Paton et al., 2011). U-Pb fractionation was corrected and analytical scatter propagated into isotopic ratios using an in-house Excel spreadsheet, based on the spreadsheet of Kylander-Clark, pers. comm. 2020. The carbonate reference material DBTL (Hill et al., 2016) was used to calibrate U-Pb ratios, and WC-1 (Roberts et al., 2017) was used as a secondary standard for validation.

The software package IsoplotR (Vermeesch, 2018) was used to visualize U–Pb data and calculate initial ^{234}U and ^{230}Th-disequilibrium-corrected LA-ICPMS U-Pb ages (Vermeesch et al., 2025). A conservative initial $^{234}U/^{238}U$ of 2 ± 2 (2σ) was used based on the average of modern activity ratios from a compilation of shallow-groundwater studies (e.g., Roberts et al., 2020). An initial $^{230}Th/^{238}U$ of 0 was applied because Th is highly insoluble in natural aqueous systems.

4. Results

4.1 Carbonate Paragenesis

The six studied fossil bone samples exhibit multiple generations of calcite cements precipitated within primary bone porosity and coating the outermost surface of the bone material. In a few samples, calcite cements rim clasts of brecciated bone material. Petrographic relationships and cathodoluminescence document three generations of calcite cements that fully occlude voids and early burial fracture porosity. The distribution of cement generations varies within and among the six samples.

Generation 1 calcite cements (Gen 1): Gen 1 cements occur as two morphologies. Gen 1a cements are best developed in Bone #14 and Bone #05 samples (Figs. 3A and 3B) and occur as inclusion-rich equant to bladed calcite (10-90 μm in length) crystals that fully occlude small-scale bone porosity. These cements also occur as irregular to isopachous rimming cements in larger primary pores in the bone (Fig. 3C). Gen 1a cements exhibit well-developed scalenohedral to subrounded terminations that, in cases, pass laterally into cement crystals with irregular to flat terminations (Fig 3C-3F). Microcrystalline Fe-oxides are incorporated in and/or immediately

overlie Gen 1a cements. These cements are initially dully luminescent passing into alternating non- and bright luminescent zonation toward the crystal terminations (Fig. 3D).

Gen 1b calcite cements are best developed in samples of Bone #206, Bone #03, 373-Herrera, and 512-Eoraptor (Figs. 4A-4C). Gen 1b cements occur as equant to prismatic (50-120 μm in length) crystals that evenly to irregularly line primary bone and fracture porosity (Figs. 4D-4G). They also form thin (~ 90 μm) cement crusts on clasts of brecciated bone (Fig. 3b), which is previously cemented by calcite (Figs. 4D and 4E) and on the outermost surface of unbrecciated bone material (Fig. 4D and 4G). Similar to Gen 1a cements, Gen 1b cements display scalenohedral to subrounded and flat terminations. Typically, Gen 1b exhibits zoned dull luminescence, with some cements exhibiting (5 μm) alternating non- and dull luminescent zonation towards crystal terminations (Figs 4C and 4D).

Studies of the fossilization process of bones document extensive microbial activity during the early stages of eogenesis and diagenesis (e.g., Dupraz and Visscher, 2005; Raff et al., 2013; Janssen et al., 2022). Initial organic matter decay by microbial metabolic processes leads to the release of high concentrations of base ions into the immediate environment that, in turn, facilitates the stabilization and preservation of organic material and influences mineralization of organic tissues and precipitation of minerals including carbonates (Sagemann et al., 1999; Plet et al., 2016; Janssen et al., 2022). We interpret Gen 1a cements to have precipitated soon after the death of the organism and within the vadose zone given the following characteristics. First, Gen 1a occurs as the earliest precipitated cements within primary porosity and encrusting mainly the fossil bone. Second, the honey- to gray coloration of Gen 1a cements that reflects their inclusion-rich nature is interpreted to be due to the incorporation of organic colloids and Fe-oxides during their growth, a process typical of surface sediment and soil profile conditions (Courty et al., 1994; Durand et al.,

2010; and discussed in Aguirre-Palafox et al. 2025; in prep.). Third, the irregular distribution and variable crystal termination morphology (i..e, prismatic to subrounded to flat-topped) of Gen 1a cements suggest the formation of dissolution surfaces between periods of cement precipitation in the chemically dynamic vadose environment (Wright and Tucker, 1991; Alonso-Zarza, 2003). Lastly, the presence of later Gen 2 cements that overgrow Gen 1a cements, interpreted to have formed in the shallow phreatic zone (see description and interpretation further below), indicates that Gen 1a precipitated in the vadose zone before deeper burial of the bone material.

Gen 1b cements are interpreted to have formed in the vadose zone during the initial compaction of the bone material at shallow depths. The clear crystal morphology of Gen 1b cements indicates that organics were not a major component as inclusions during their formation compared to Gen 1a cements, suggesting that Gen 1b cements precipitated after the decay of most of the organic matter associated with the death of the specimen. Gen 1b cements line fracture porosity and forms cement crusts on clasts of brecciated bone undergoing initial compaction, further suggesting formation within a few meters from the paleo-surface. Lastly, the scalenohedral to subrounded and flat crystal terminations of Gen 1b cements are interpreted to record episodes of dissolution between precipitation of cements layers, possibly in response to seasonal or longer-term climate functions.

Generation 2 calcite cements (Gen 2): Gen 2 cements overgrow Gen 1 cements as clear medium-crystalline (100 to 200 μm) equant to subrounded calcite crystals. Gen 2 cements occlude remaining porosity in medium- to larger scale pores (Fig. 3E). Gen 2 cements exhibit well-developed CL zonation that is initially nonluminescent passing into thicker (10s μm) bands of dully luminescent orange to brightly luminescent calcite alternating with nonluminescent calcite (Fig. 3F).

The medium-crystalline equant to sub-equant crystal morphologies of Gen 2 cements indicate that these cements precipitated slowly under carbonate-saturated conditions. The alternating nonluminescent with dully to brightly luminescent zonation, typically associated with high Mn2+ but low Fe2+ aqueous concentrations, is interpreted to record formation in the diagenetic realm where pore waters fluctuate between oxidizing (low Mn2+ and Fe2+) and slightly reducing conditions (high Mn2+ but low Fe2+) (Barnaby and Rimstidt, 1989). A similar CL zonation is present in cements precipitated within primary porosity and syndepositional fractures in carbonate nodules from paleosols of the Ischigualasto Fm (Aguirre-Palafox et al., 2024).

Generation 3 calcite cements (Gen 3): Gen 3 cements consist of blocky clear calcite spar with well-developed rhombohedral crystal faces and occludes remaining primary porosity. Gen 3 cements exhibit bright orange to yellow luminescence (Figs 3C-3F).

Gen 3 cements are interpreted to have formed in water-saturated pores of the phreatic zone. The bright luminescence of Gen 3 cements indicates high Mn^{2+} but low Fe2+ concentrations in the crystal lattice, indicative of low Eh conditions typical of the deeper phreatic conditions.

4.2 U-Pb carbonate geochronology

^{234}U- and ^{230}Th-disequilibrium corrected LA-ICP-MS U-Pb data are presented in Figure 6, Table 1, and in the Supporting Information. The U-Pb LA-ICP-MS data is available via geochron.org at https://www.geochron.org/dataset/html/geochron_dataset_2025_03_21_UwQ4w

Uncertainties for the LA-ICP-MS U-Pb carbonate date are reported as ± 2σ and expressed in the format X/Y/Z, where X incorporates analytical uncertainties only, Y additionally includes uncertainty in the age of the primary reference material (here, DBTL; Hill et al., 2016), and Z includes our ± 2% external reproducibility.

The stratigraphically lowest fossil bone sample (Bone #206) was collected from a Dinosauria indeterminate (indet.) species in the La Peña Mbr, near the base of the Ischigualasto Fm (Fig. 2). Based on U-Pb analyses of Gen 1b cements, Bone #206 has an isochron U-Pb age of 231.2 ± 4.1/4.7/6.6 Ma (MSWD = 0.86, n= 24; Fig. 5A)

A second fossil bone sample (Bone #14) was collected from a Dinosauria indet. from the Cementerio de Rinconsaurios locality in the lower Canchas de Bochas Mbr, approximately 63 m from the base of the Ischigualasto Fm (Fig. 2). Based on U-Pb analyses of Gen 1a cements, the fossil Bone #14 sample has an isochron age of 230.8 ± 5.1/5.6/7.3 Ma (MSWD = 1.3, n=40; Fig. 4B).

Four samples of fossil bone (Bone #05, Bone #05, 373-Herrera and 512-Eoraptor) were collected from the middle Cancha de Bochas Mbr, approximately 110 m above the base of the Ischigualasto Fm (Fig. 2). Sample Bone #03 has an isochron age of 230.5 ± 3.7/4.4/6.3 Ma (MSWD = 0.97, n=8; Fig. 4C) based on analysis of Gen 1b cements. Based on U-Pb analyses of Gen 1a cements, sample Bone #05 has an isochron age of 230.1 ± 2.8/3.6/5.9 Ma (MSWD = 0.97, n=40; Fig. 5D). An isochron age of 225.9 ± 2.3/3.2/5.6 Ma (MSWD = 1.7, n=20; Fig. 5E) for Bone #05 was calculated based on analysis of Gen 2 cements.

U-Pb analyses of Gen 1b cements (epoxy mounted samples) associated with two dinosaur bone fragments from the same deposit (373-Herrera, Herrerasaurus genus; 512-Eoraptor, Eoraptor

genus) yield an isochron age of 230.0 ± 4.0/4.6/6.5 Ma (MSWD = 1.6, n= 30; Fig. 4F) and 229.7 ± 4.7/5.2/7.0 Ma (MSWD = 0.9, n=52; Fig. 4E), respectively. Based on U-Pb analyses of Gen 2 cements, 512-Eoraptor has an isochron age of 221.1 ± 2.8/3.6/5.7 Ma (MSWD = 1.6, n= 61; Fig. 4H)

5. Discussion

5.1 Assessment of the Accuracy and Precision of Calcite Cement U-Pb Ages from Vertebrate Bone Fossils of the Ischigualasto Fm.

The U-Pb carbonate ages for the six studied samples overlap within uncertainty with the published single zircon U-Pb and sanidine and plagioclase $^{40}Ar/^{39}Ar$ ages of several intercalated volcanic ashes (±2σ; Rogers et al., 1993; Martínez et al., 2011; Colombi et al., 2021). They further coincide with U-Pb carbonate ages obtained for early diagenetic cements of carbonate nodules from intercalated paleosols in the Ischigualasto Fm. A calcite cement age of 231.2 ± 4.1/4.7/6.6 Ma for the stratigraphically lowermost fossil bone sample (Bone #206), collected near the base of the Ischigualasto Fm, is in agreement with the recalibrated $^{40}Ar/^{39}Ar$ sanidine age of 231.4 ± 0.3 Ma assigned to the "Herr Toba" bentonite 20 m above the Peña conglomerate (Fig. 2).

The remaining vertebrate bone samples that span 63 to 110 m in the Ischigualasto Fm are chronologically in stratigraphic order and consistent with their stratigraphic position between the "Herr Toba" bentonite (231.4 ± 0.3 Ma) and a CA-TIMS U-Pb zircon dated tuff ~310 m above the base of the Ischigualasto Fm (228.91 ± 0.14 Ma; Colombi et al., 2021). The fossil bone sample ~43 m above "Herr Toba" bentonite (Bone #14) has a U-Pb age of 230.8 ± 5.1/5.6/7.3 Ma in agreement with its stratigraphic placement (Fig. 2). The U-Pb carbonate ages for the four fossil

bone samples from ~47 m higher in the stratigraphy (Bone #05, Bone #03, 373-Herrera, and 512-Eoraptor) are 230.1 ± 2.8/3.6/5.9 Ma, 230.5 ± 3.7/4.4/6.3 Ma, 229.7 ± 4.7/5.2/7.0 Ma, and 230.0 ± 4.0/4.6/6.5 Ma, respectively, indistinguishable within uncertainty. They further overlap with and are younger than the U-Pb age of the stratigraphically lower sample (Bone #14; 230.8 ± 5.1/5.6/7.3 Ma) and the 231.4 ± 0.3 Ma age of the "Herr Toba" bentonite 20 m from the base of the Ischigualasto Fm but older than the 228.91 ± 0.14 Ma age of the bentonite near the middle of the Ischigualasto Fm (~310 m). Notably, the U-Pb ages for these four fossil bone samples (Bone #05, Bone #03, 373-Herrera and 512-Eoraptor) overlap within uncertainty with the 230.5 ± 2.2 Ma age for a pedogenic carbonate nodule (ISCH-107) collected from a paleosol 3 m below the vertebrate bone samples (Aguirre-Palafox et al., 2024). The overlap in U-Pb ages obtained from syndepositional and early diagenetic calcite cements within the pedogenic carbonate nodules and vertebrate fossil bones from the Ischigualasto Fm demonstrates the importance of a well-established cement-stratigraphy in guiding LA-ICP-MS U-Pb analyses and for accurate age interpretation of the ablated precipitates. Moreover, the overlap in the ages of two carbonate precipitates with distinctive complex geochemical histories of precipitation and diagenesis further validates the potential of U-Pb carbonate geochronology in dating the terrestrial record, especially in successions with limited to no radioisotope ages due to a paucity of volcanic deposits.

5.2 U-Pb Systematics of Calcite Cements Ages from Vertebrate Fossils in the Ischigualasto Fm.

In this section, we document the distinctive isotopic signatures and U-Pb ratios of the carbonate precipitates in the studied fossilized vertebrate samples and general trends and insights from these analyses and previous pedogenic carbonate studies (Aguirre-Palafox et al., 2024, 2025, in prep).

U-Pb isotopic signatures of Gen 1a and Gen 1b cements show promise for U-Pb dating of carbonate nodules. The isotopic data of Gen 1a cements in the Bone #14 and Bone #05 samples show moderate spread in $^{238}U/^{206}Pb$ clustering between 1 and 20 and U concentrations ranging from 0.8 to 16 ppm by mass. Gen 1b cements in Bone #206, Bone #03, 373-Herrera and 512-Eoraptor have a similar spread in $^{238}U/^{206}Pb$ between 1 and 21 but higher U concentrations ranging from 0.3 to 37 ppm by mass compared to Gen 1a cements. Both Gen 1a and Gen 1b cements.

Gen 1a cements are interpreted as microbially mediated cements that precipitated soon after the death of the organism and within the vadose zone. The U concentrations in Gen 1a cements can be attributed to their association with the decay of organic matter. Previous studies show that organic-rich material (e.g., rhizoliths) and other sedimentary deposits (e.g., black shales, calcretes) are linked to higher U concentrations (e.g., Cumberland et al., 2016; Cuney, 2010; Gauthier-Lafaye et al., 1989; Kelly et al., 2006; Rasbury et al., 1997). A similar U-enrichment mechanism is proposed for syn-pedogenic cements precipitated within primary porosity in carbonate nodules from paleosols of the Ischigualasto Fm (Aguirre-Palafox et al., 2024) and the Eastern Shelf of the Midland Basin (Aguirre-Palafox et al., 2025, in prep). In these studies, the syn-depositional cements are interpreted as microcodium associated with plant roots and as incipient calcretes lining root casts soon after plant root decay, respectively. Gen 1b cements in the studied samples are also interpreted as early cements precipitated within the vadose zone due to the equant to prismatic crystal morphology, occurrence as cements that line primary bone and fracture porosity, and precipitation before Gen 2 cements interpreted to have precipitated in the pore saturated shallow phreatic zone. U-enrichment in Gen 1b cements could be explained by the presence and decay of organic matter associated with the death of the specimen and the fossilization process. Cements of similar morphology are documented in fracture porosity of carbonate nodules from the

Ischigualasto Fm (Aguirre-Palafox et al., 2024). However, these carbonate nodule cements are deemed unsuitable for U-Pb dating due to higher isotopic scatter on T-W plots, higher MSWDs and dates that are considerably older than expected based on higher-precision dating of volcanic deposits.

U-Pb isotopic signatures of Gen 2 cements in Bone #05 and 512-Eoraptor have moderate spreads in $^{238}U/^{206}Pb$ (2 to 30 and 6 to 18, respectively) and adequate U concentrations (2 to 67 ppm by mass and 10 to 28 ppm by mass, respectively) favorable for U-Pb dating. However, the U-Pb dates for these cements are 3 to 6 Myr younger than expected based on the higher-precision ages of the intercalated volcanics (Herr Toba and ~310 m tuff) and the U-Pb carbonate ages for Gen 1 cements within the same fossil bone samples (Fig. 2). Gen 2 cements precipitated in bone porosity in the studied samples are interpreted to have formed in the shallow phreatic zone based on their clear medium-crystalline equant to subrounded crystal morphology and well-developed thick CL zonation (Figs. 3E and 3F) usually documented in the shallow phreatic zone due to fluctuations in redox (Eh) conditions of pore waters (Barnaby and Rimstidt, 1989). The younger ages for Gen 2 cements agree with this interpretation.

U-Pb isotopic signatures of Gen 3 cements indicate that these cements are not suitable for U-Pb dating due to limited spread in $^{238}U/^{206}Pb$ ranging from 0.02 to 0.7 and U concentrations averaging 0.7 ppm by mass. Gen 3 are interpreted as late diagenetic cements that formed in water-saturated pores of the phreatic zone. A similar spread in $^{238}U/^{206}Pb$ and U concentrations are documented in late diagenetic cements that precipitated within and fully occlude primary porosity of carbonate nodules from paleosols in the Ischigualasto Fm (Aguirre-Palafox et al., 2024) and Eastern Shelf of the Midland Basin (Aguirre-Palafox et al., 2025, in prep).

6. Conclusions

The direct dating of fossil vertebrates in deep time is often difficult due to complex histories of radiogenic isotope and rare earth element uptake over time and chemical alteration during fossilization and after burial. U-Pb carbonate LA-ICP-MS geochronology provides a new strategy to indirectly date fossil material by dating calcite cements that precipitate within the primary porosity of fossil bone and early burial fracture porosity, given that a well-characterized paragenetic framework for individual samples is established to guide LA-ICP-MS analyses and help in the accurate interpretation of the calculated dates. In this study, we analyzed cements precipitated in five dinosaur and one archosaur bone samples from the Late Triassic Ischigualasto Fm of northwest Argentina, noting that calcite cements in primary bone porosity and early burial fracture porosity have $^{238}U/^{206}Pb$ and uranium concentrations adequate for precise dating. The U-Pb ages for these cements estimate the timing of calcite precipitation within the vadose zone before the initial transition of the bone material from the vadose into the shallow phreatic zone. Based on depositional rates in this section of the Ischigualasto Fm and the lack of evidence for U-Pb open-system behavior in the analyzed cements, we infer the timing of calcite precipitation is close to the time of death and burial of the specimens. The U-Pb ages for the calcite cements precipitated within bone and fracture porosity are comparable to existing radioisotopic ages of volcanic ashes and calcite cements in carbonate nodules from paleosols intercalated within the succession. The agreement and overlap in ages from carbonate precipitates characterized by distinct geochemical histories of precipitation and diagenesis (cements in fossil bone and carbonate nodules from paleosols) further validates the potential of U-Pb carbonate geochronology in dating the terrestrial record. This dating approach is particularly valuable in stratigraphic successions where radioisotopic ages are scarce or absent due to the limited presence of volcanic deposits. Lastly, this

study marks the first successful indirect dating of basal Herrerasaurus and Eoraptor specimens from the Ischigualasto Fm, a critical succession for examining the origin, rapid emergence and diversification of early dinosaurs during the Late Triassic.

Open Research

The LA-ICPMS U-Pb data used for concordia plots and the $^{238}U/^{206}Pb$ vs U ppm plot in the study are available at Geocrhon.org via https://www.geochron.org/dataset/html/geochron_dataset_2025_03_21_UwQ4w

Figures and Table:

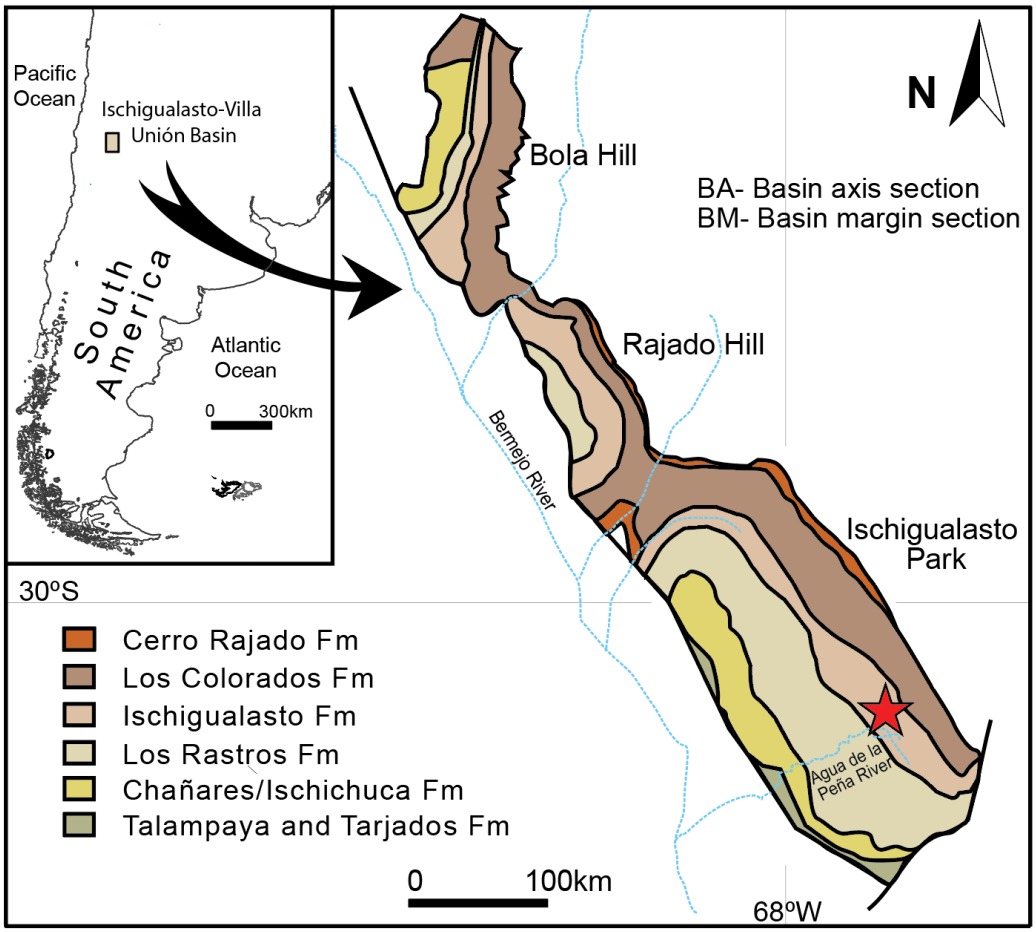

Figure 1. Location and geologic map of the Ischigualasto-Villa Union Basin, Argentina. Permian (Talampaya, Tarjados), Triassic (Chañeres/Ischichuca, Los Rastros, and Ischigualasto fms) through Jurassic (Los Colorados Fm) stratigraphy indicated by colors, with the Late Triassic Ischigualasto Fm in tan. Red star indicate the approximate location of sample localities. Figure adapted from C. Colombi et al. (2021).

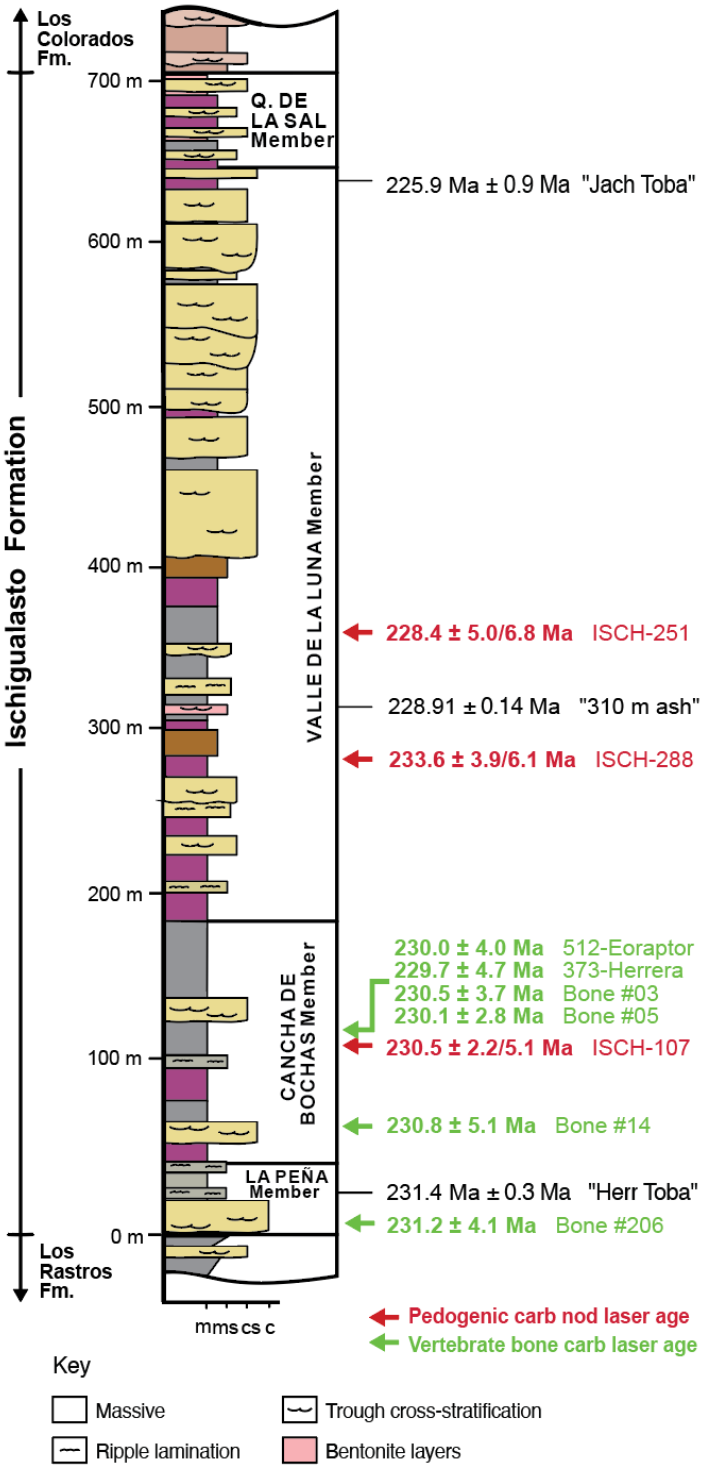

Figure 2. Generalized stratigraphy for the basin axis region of the Ischigualasto Fm was modified after C. Colombi et al., 2021. Stratigraphic position of published zircon U-Pb and sanidine and

plagioclase $^{40}Ar/^{39}Ar$ ages from intercalated volcanic ashes shown by black lines (Roger et al., 1993; Martínez et al., 2011; Colombi et al., 2021) and of the U-Pb carbonate ages of earliest generation calcite cements from carbonate nodules shown by red arrows (Aguirre-Palafox et al., 2024). The U-Pb carbonate ages of earliest generation calcite cements in vertebrate fossil bones shown by green arrows (this study). Colors in the stratigraphic column represent similar colors of rocks as seen in the outcrop. Uncertainties on all ages are ±2σ.

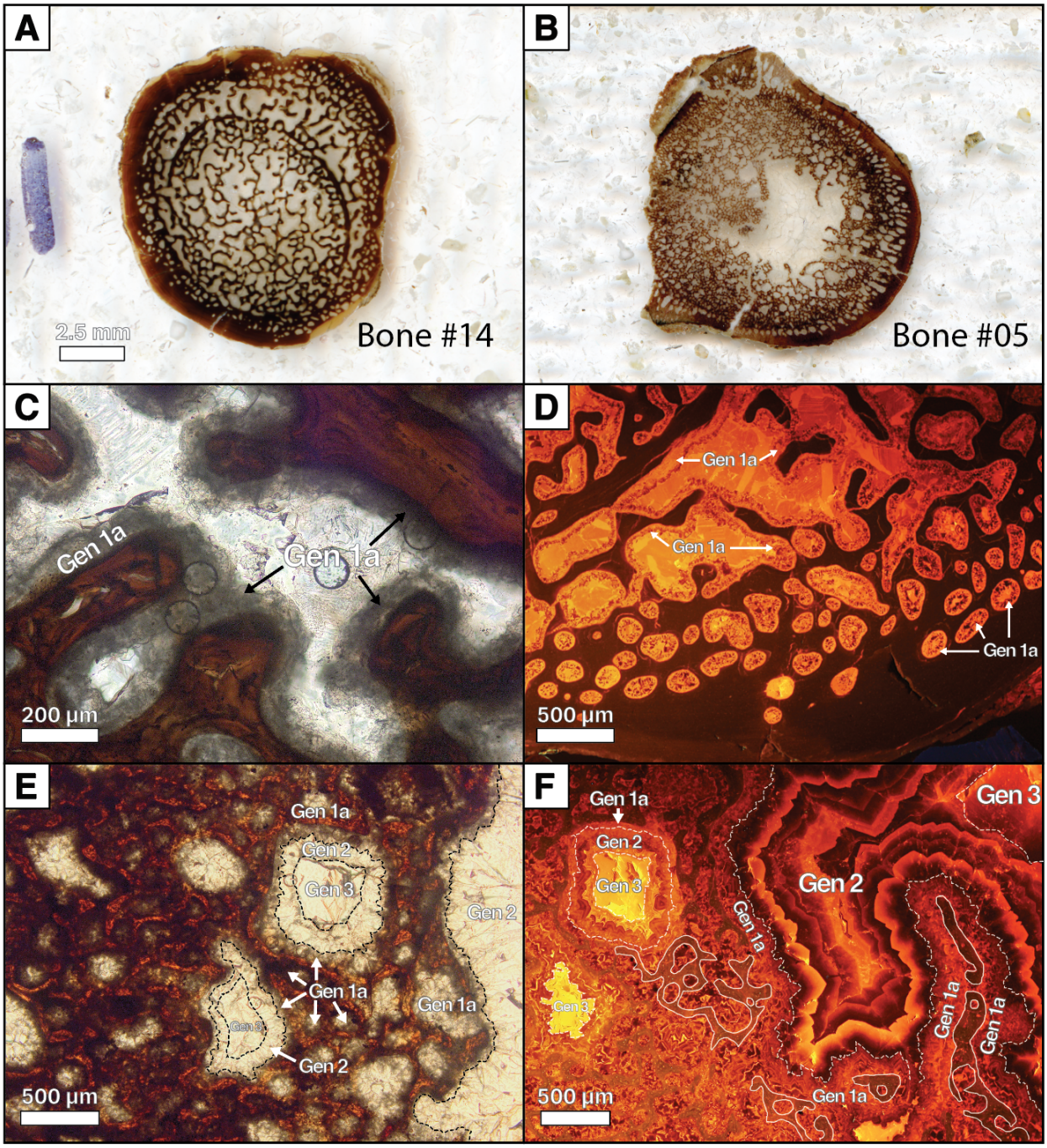

Figure 3. Photomicrographs of generation 1a calcite cements in the Bone #14 and Bone #05 samples. Photographs of Bone #14 (A) and Bone #05 (B) showing small to large-scaled bone and fracture porosity filled by calcite cements. (C) Inclusion-rich equant to bladed (10-90 µm in length) Gen 1a cements irregularly to isopachously line large-scale bone porosity in Bone #14, PPL view.

(D) Lower magnification image of ‘C’ in CL showing Gen 1a cements that are initially dully luminescent passing into nonluminescent zonation toward the crystal terminations. Note the uneven thickness of cements and scalenohedral to flat end terminations of some Gen 1a cements. (E) Inclusion-rich bladed (10-90 μm in length) Gen 1a cements in Bone #05 fully occluding small-scale porosity. These cements irregularly to isopachiously line medium to large-scale bone porosity and are overgrown by clear medium-crystalline (100 to 150 μm) equant to subrounded calcite crystals (Gen 2), PPL view. (F) CL of Gen 1a and Gen 2 cements in Bone #05. Gen 2 exhibit well-developed zonation that is initially nonluminescent passing into a series of (10s μm) bands of dully luminescent orange to brightly luminescent calcite. Some of the bone material is outlined by solid thin white lines. Visible laser ablation pits are 85 μm in diameter.

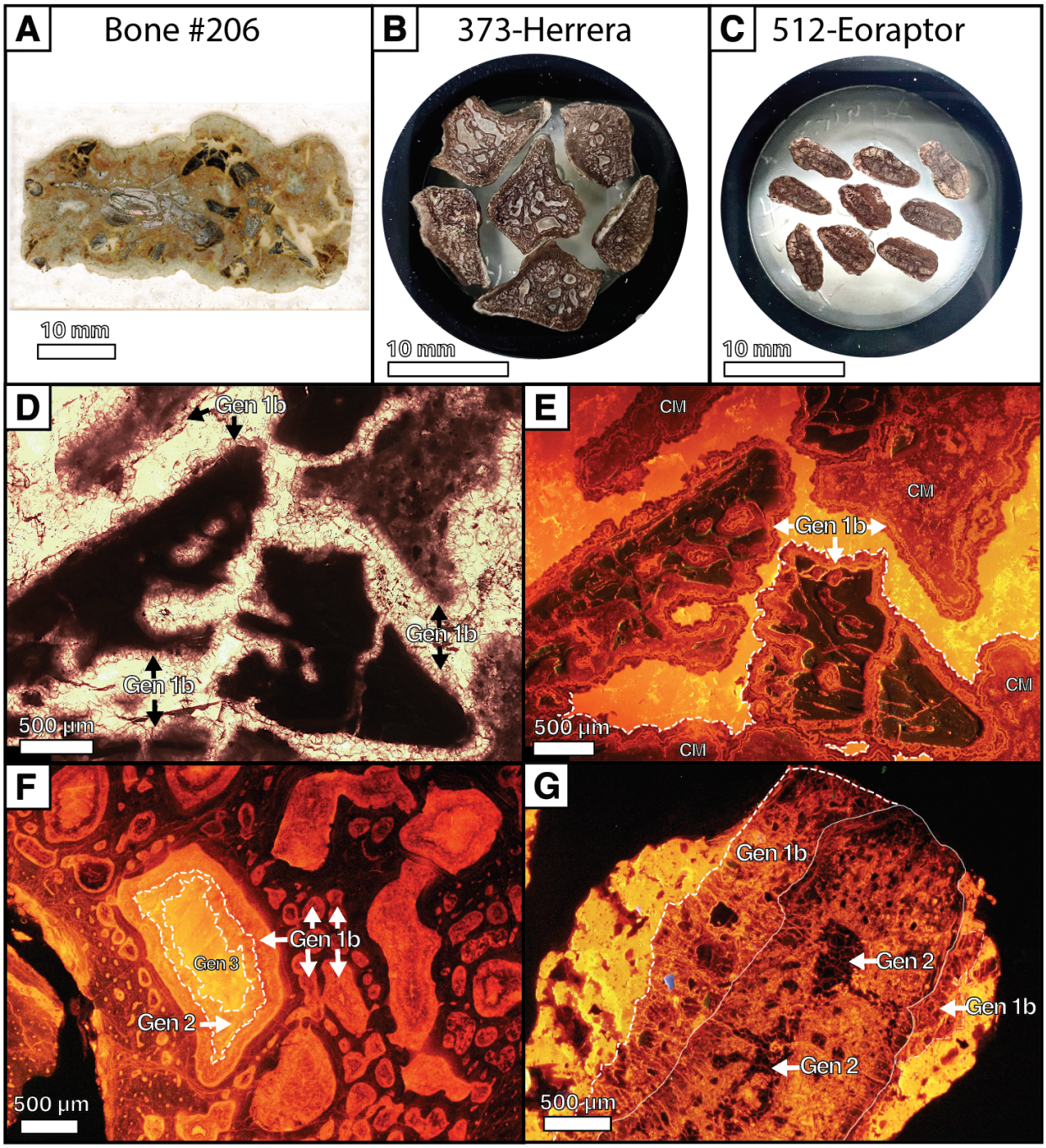

Figure 4. Photomicrographs of generation 1b calcite cements in the Bone #206, 373-Herrera and 512-Eoraptor samples. Photographs of (A) Bone #206 [Dinosauria indeterminate species], (B) 373-Herrera [Herrerasaurus genus], (C) 512-Eoraptor [Eoraptor genus] and showing calcite cements infilling small to large-scaled bone and fracture porosity and the outer surface of the bone

material. (D) Gen 1b cements with scalenohedral to subrounded and flat terminations evenly to irregularly line primary bone, fracture porosity and brecciated carbonate micrite (CM). Note Gen 1b cements fully occluding small-scale primary bone porosity and cementing brecciated bone material, PPL view. (E) Image of 'D' in CL showing the zoned dull luminescence of Gen 1b cements in Bone #206, with some cements exhibiting (5 μm) alternating non- and dull luminescent zonation towards crystal terminations. (F) Gen 1b cements in 373-Herrera mainly line primary bone porosity, where they fully occlude small-scale pores and are the first cements lining medium to large-scale pores, CL view. (G) CL image of Gen 1b in the 512-Eoraptor sample that occur as cements lining the outer surface of the bone material and are dully luminescent. Gen 2 cements that occur as clear medium-crystalline (100 to 200 μm) equant to subrounded calcite crystals that display nonluminescence. Gen 2 cements fully occlude small to large-scale bone porosity. Note that both Gen 1b and Gen 2 cements are highly cross-cut by late diagenetic cements that are brightly luminescent. The bone material is outlined by a solid thin white line.

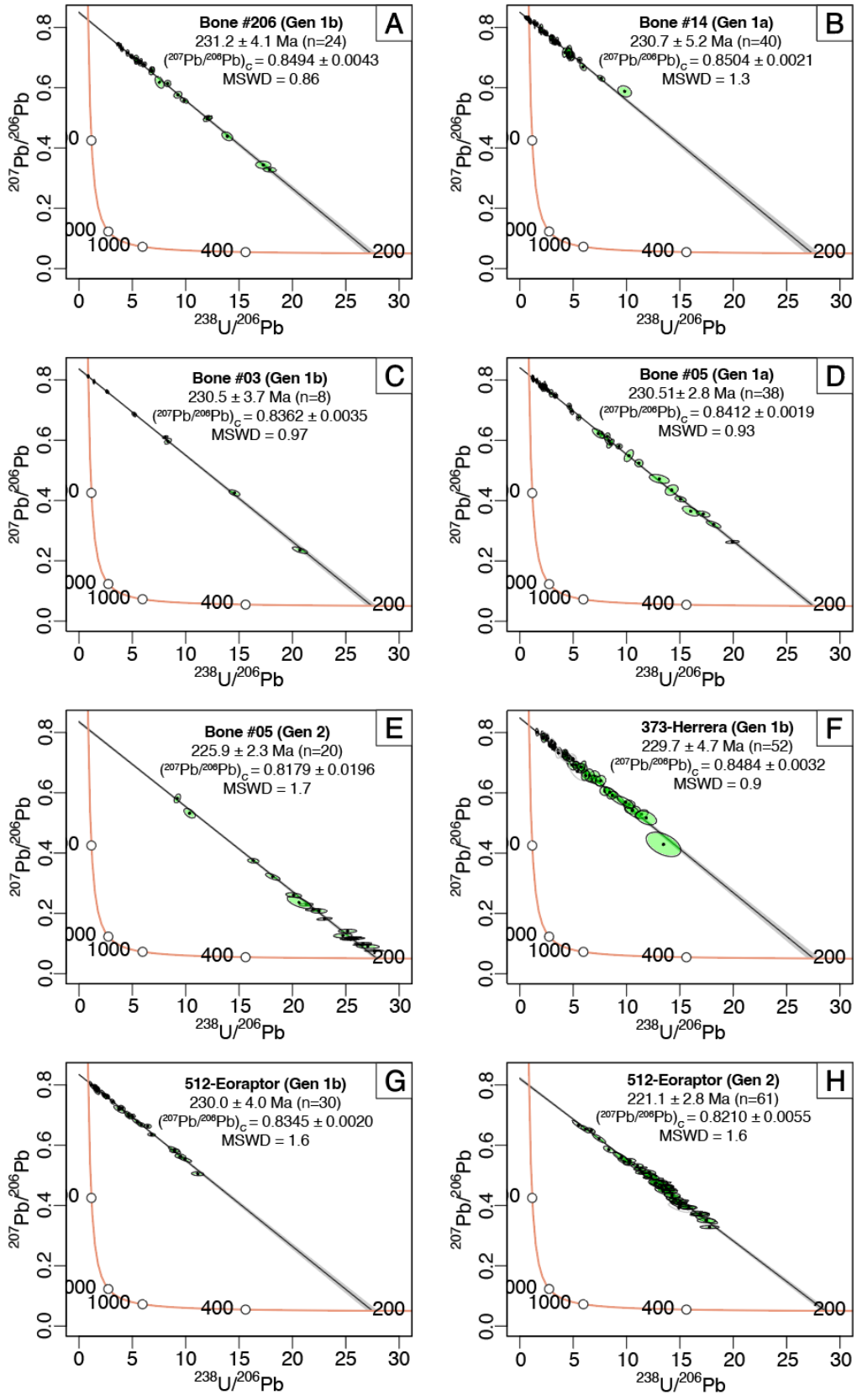
A
Bone #206 (Gen 1b)
231.2 ± 4.1 Ma (n=24)
(207Pb/206Pb)c = 0.8494 ± 0.0043
MSWD = 0.86
B
Bone #14 (Gen 1a)
230.7 ± 5.2 Ma (n=40)
(207Pb/206Pb)c = 0.8504 ± 0.0021
MSWD = 1.3
C
Bone #03 (Gen 1b)
230.5 ± 3.7 Ma (n=8)
(207Pb/206Pb)c = 0.8362 ± 0.0035
MSWD = 0.97
D
Bone #05 (Gen 1a)
230.51± 2.8 Ma (n=38)
(207Pb/206Pb)c = 0.8412 ± 0.0019
MSWD = 0.93
E
Bone #05 (Gen 2)
225.9 ± 2.3 Ma (n=20)
(207Pb/206Pb)c = 0.8179 ± 0.0196
MSWD = 1.7
F
373-Herrera (Gen 1b)
229.7 ± 4.7 Ma (n=52)
(207Pb/206Pb)c = 0.8484 ± 0.0032
MSWD = 0.9
G
512-Eoraptor (Gen 1b)
230.0 ± 4.0 Ma (n=30)
(207Pb/206Pb)c = 0.8345 ± 0.0020
MSWD = 1.6
H
512-Eoraptor (Gen 2)
221.1 ± 2.8 Ma (n=61)
(207Pb/206Pb)c = 0.8210 ± 0.0055
MSWD = 1.6
1000
400
200
207Pb/206Pb
238U/206Pb

Figure 5. Tera-Wasserburg concordia plots of analyzed carbonate precipitates in the studied fossil vertebrate bones. (A) Plotted U-Pb data from Gen 1b cements in Bone #206. (B) Plotted U-Pb data from Gen 1a cements in Bone #14. (C) Plotted U-Pb data from Gen 1b cements in Bone #03. (D) Plotted U-Pb data from Gen 1a cements in Bone #05. (E) Plotted U-Pb data from Gen 2 cements in Bone #05. (F) Plotted U-Pb data from Gen 1b cements in 373-Herrera. (G) Plotted U-Pb data from Gen 1b cements in 512-Eoraptor. (H) Plotted U-Pb data from Gen 2 cements in 512-Eoraptor.

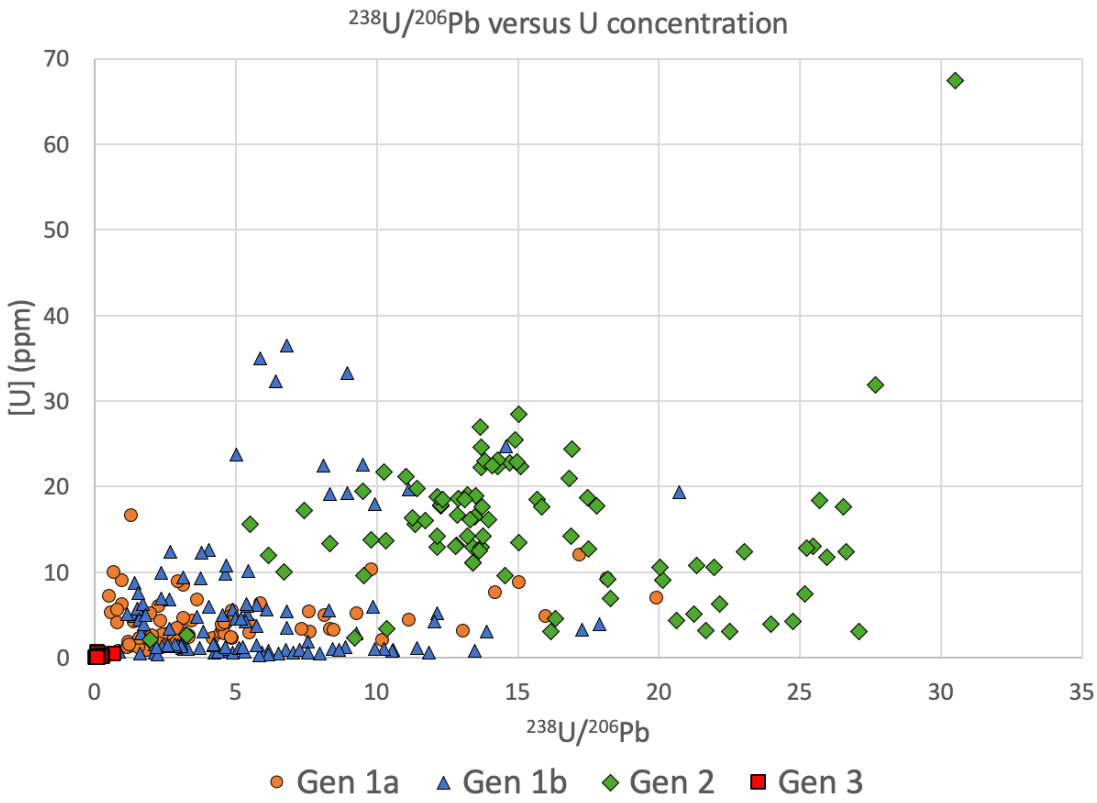

Figure 6. Compilation of U concentration versus $^{238}U/^{206}Pb$ of representative Gen 1a, Gen 1b, Gen 2 and Gen 3 calcite cements in all studied fossil vertebrate bones. Except for Gen 3 cements, all of the other cement generations have U concentrations and adequate spreads in $^{238}U/^{206}Pb$ suitable for precise U-Pb carbonate dating. Gen 1a cements (orange circles) have U concentrations ranging from 0.8 to 17 ppm by mass and a moderate spread in $^{238}U/^{206}Pb$ of 0.5 to 20. Gen 1b cements (blue triangles) have slightly higher U concentrations (0.3 to 37 ppm by mass) but a similar range of $^{238}U/^{206}Pb$ (0.9 to 21) compared to Gen 1a cements. Gen 2 cements (green diamonds) have U concentrations ranging from 2.1 to 67 ppm by mass and the largest spread in $^{238}U/^{206}Pb$ of 2 to 30 of all the studied cements. Gen 3 cements (red squares) have the narrowest range in $^{238}U/^{206}Pb$ (0.02 to 0.68) and the lowest U concentrations (< 0.7 by mass) of all studied carbonate precipitates.

Table 1. LA-ICP-MS U-Pb data and ages of calcite cements in vertebrate fossils from the Ischigualasto Fm

Sample name	Clade/Genus	Stratigraphic level (m)	Average U (ppm)	Average Pb (ppm)	Isochron age (Ma)	MSWD	$^{207}Pb/^{206}Pb$ (Pbc)*	Paragenesis
Bone #206	Dinosauria	Near base of formation	4.7	2.3	231.2 ± 4.1	0.86	0.8494 ± 0.0043	Gen 1b
Bone #14	Dinosauria	63	5.1	20	230.7 ± 5.2	1.3	0.8504 ± 0.0021	Gen 1a
Bone #03	Dinosauria	110	12.3	6.2	230.5 ± 3.7	0.97	0.8362 ± 0.0035	Gen 1b
Bone #05	Archosauria	110	3.4	2.2	230.1 ± 2.8	0.93	0.8412 ± 0.0019	Gen 1a
Bone #05	Archosauria	110	10.5	0.5	225.9 ± 2.3	1.7	0.8179 ± 0.0196	Gen 2
373-Herrera	Herrerasaurus	110	1.0	0.9	229.7 ± 4.7	0.9	0.8484 ± 0.0032	Gen 1b
512-Eoraptor	Eoraptor	110	13.4	10.7	230.0 ± 4.0	1.6	0.8345 ± 0.0020	Gen 1b
512-Eoraptor	Eoraptor	110	17.4	3	221.1 ± 2.8	1.6	0.8210 ± 0.0055	Gen 2

* $^{207}Pb/^{206}Pb$ (Pbc): Initial common lead

References Cited:

Aguirre Palafox, L.E., Möller, A., McLean, N.M., Ludvigson, G.A., Colombi, C.E., and Montañez, I.P., 2024, U-Pb Geochronology of Paleosol Carbonate Cements by LA-ICP-MS: A Proof of Concept and Strategy for Dating the Terrestrial Record: Geochemistry, Geophysics, Geosystems, v. 25, p. e2024GC011488, doi:https://doi.org/10.1029/2024GC011488.

Alonso-Zarza, A.M., 2003, Palaeoenvironmental significance of palustrine carbonates and calcretes in the geological record: Earth-Science Reviews, v. 60, doi:10.1016/S0012-8252(02)00106-X.

Artabe, A., Morel, E., and Spalletti, L., 2001, Paleoecología de las floras triásicas argentinas: El Sistema Triásico en la Argentina, p. 199–225.

Barnaby, R.J., and Rimstidt, J.D., 1989, Redox conditions of calcite cementation interpreted from Mn and Fe contents of authigenic calcites: Geological Society of America Bulletin, v. 101, doi:10.1130/0016-7606(1989)101<0795:RCOCCI>2.3.CO;2.

Césari, S.N., and Colombi, C.E., 2013, A new Late Triasssic phytogeographical scenario in westernmost Gondwana: Nature Communications, v. 4, doi:10.1038/ncomms2917.

Colombi, C.E., Limarino, C.O., and Alcober, O.A., 2017, Allogenic controls on the fluvial architecture and fossil preservation of the Upper Triassic Ischigualasto Formation, NW Argentina: Sedimentary Geology, v. 362, doi:10.1016/j.sedgeo.2017.10.003.

Colombi, C., Martínez, R.N., Césari, S.N., Alcober, O., Limarino, C.O., and Montañez, I., 2021, A high-precision U–Pb zircon age constraints the timing of the faunistic and palynofloristic

events of the Carnian Ischigualasto Formation, San Juan, Argentina: Journal of South American Earth Sciences, v. 111, doi:10.1016/j.jsames.2021.103433.

Courty, M.A., Marlin, C., Dever, L., Tremblay, P., and Vachier, P., 1994, The properties, genesis and environmental significance of calcitic pendents from the High Arctic (Spitsbergen): Geoderma, v. 61, doi:10.1016/0016-7061(94)90012-4.

Cumberland, S.A., Douglas, G., Grice, K., and Moreau, J.W., 2016, Uranium mobility in organic matter-rich sediments: A review of geological and geochemical processes: Earth-Science Reviews, v. 159, doi:10.1016/j.earscirev.2016.05.010.

Cuney, M., 2010, Evolution of uranium fractionation processes through time: Driving the secular variation of uranium deposit types: Economic Geology, v. 105, doi:10.2113/gsecongeo.105.3.553.

Currie, B.S., Colombi, C.E., Tabor, N.J., Shipman, T.C., and Montañez, I.P., 2009, Stratigraphy and architecture of the Upper Triassic Ischigualasto Formation, Ischigualasto Provincial Park, San Juan, Argentina: Journal of South American Earth Sciences, v. 27, doi:10.1016/j.jsames.2008.10.004.

Drost, K., Chew, D., Petrus, J.A., Scholze, F., Woodhead, J.D., Schneider, J.W., and Harper, D.A.T., 2018, An Image Mapping Approach to U-Pb LA-ICP-MS Carbonate Dating and Applications to Direct Dating of Carbonate Sedimentation: Geochemistry, Geophysics, Geosystems, v. 19, doi:10.1029/2018GC007850.

Dupraz, C., and Visscher, P.T., 2005, Microbial lithification in marine stromatolites and hypersaline mats: Trends in Microbiology, v. 13, doi:10.1016/j.tim.2005.07.008.

Durand, N., Monger, H.C., and Canti, M.G., 2010, Calcium Carbonate Features, *in* Stoops, G., Marcelino, V., and Mees, F. eds., Interpretation of Micromorphological Features of Soils and Regoliths, Amsterdam, Elsevier, p. 149–194, doi:https://doi.org/10.1016/B978-0-444-53156-8.00009-X.

Fassett, J.E., Heaman, L.M., and Simonetti, A., 2011, Direct U-Pb dating of Cretaceous and Paleocene dinosaur bones, San Juan Basin, New Mexico: Geology, v. 39, doi:10.1130/G31466.1.

Gauthier-Lafaye, F., Weber, F., and Ohmoto, H., 1989, Natural fission reactors of Oklo: Economic Geology, v. 84, doi:10.2113/gsecongeo.84.8.2286.

Godeau, N., Deschamps, P., Guihou, A., Leonide, P., Tendil, A., Gerdes, A., Hamelin, B., and Girard, J.P., 2018, U-Pb dating of calcite cement and diagenetic history in microporous carbonate reservoirs: Case of the Urgonian Limestone, France: Geology, v. 46, doi:10.1130/G39905.1.

Grün, R., and Stringer, C., 2023, Direct dating of human fossils and the ever-changing story of human evolution: Quaternary Science Reviews, v. 322, doi:10.1016/j.quascirev.2023.108379.

Guillong, M., Wotzlaw, J.F., Looser, N., and Laurent, O., 2020, Evaluating the reliability of U-Pb laser ablation inductively coupled plasma mass spectrometry (LA-ICP-MS) carbonate geochronology: Matrix issues and a potential calcite validation reference material: Geochronology, v. 2, doi:10.5194/gchron-2-155-2020.

Gulbranson, E.L. et al., 2022, U–Pb Geochronology and Stable Isotope Geochemistry of Terrestrial Carbonates, Lower Cretaceous Cedar Mountain Formation, Utah: Implications for Synchronicity of Terrestrial and Marine Carbon Isotope Excursions: Geosciences (Switzerland), v. 12, doi:10.3390/geosciences12090346.

Herwartz, D., Tütken, T., Münker, C., Jochum, K.P., Stoll, B., and Sander, P.M., 2011, Timescales and mechanisms of REE and Hf uptake in fossil bones: Geochimica et Cosmochimica Acta, v. 75, doi:10.1016/j.gca.2010.09.036.

Hill, C.A., Polyak, V.J., Asmerom, Y., and P. Provencio, P., 2016, Constraints on a Late Cretaceous uplift, denudation, and incision of the Grand Canyon region, southwestern Colorado Plateau, USA, from U-Pb dating of lacustrine limestone: Tectonics, v. 35, doi:10.1002/2016TC004166.

Janssen, K., Mähler, B., Rust, J., Bierbaum, G., and McCoy, V.E., 2022, The complex role of microbial metabolic activity in fossilization: Biological Reviews, v. 97, doi:10.1111/brv.12806.

Kelly, S.D., Rasbury, E.T., Chattopadhyay, S., Kropf, A.J., and Kemner, K.M., 2006, Evidence of a stable uranyl site in ancient organic-rich calcite: Environmental Science and Technology, v. 40, doi:10.1021/es051970v.

Koenig, A.E., Lucas, S.G., Neymark, L.A., Heckert, A.B., Sullivan, R.M., Jasinski, S.E., and Fowler, D.W., 2012, Direct U-Pb dating of Cretaceous and Paleocene dinosaur bones, San Juan Basin, New Mexico: Geology, v. 40, doi:10.1130/G32154C.1.

Li, Q., Parrish, R.R., Horstwood, M.S.A., and McArthur, J.M., 2014, U-Pb dating of cements in Mesozoic ammonites: Chemical Geology, v. 376, doi:10.1016/j.chemgeo.2014.03.020.

Mancuso, A.C., Irmis, R.B., Pedernera, T.E., Gaetano, L.C., Benavente, C.A., and Breeden, B.T., 2022, Paleoenvironmental and Biotic Changes in the Late Triassic of Argentina: Testing Hypotheses of Abiotic Forcing at the Basin Scale: Frontiers in Earth Science, v. 10, doi:10.3389/feart.2022.883788.

Martínez, R.N., Apaldetti, C., Alcober, O.A., Colombi, C.E., Sereno, P.C., Fernandez, E., Malnis, P.S., Correa, G.A., and Abelin, D., 2012, Vertebrate succession in the ischigualasto formation: Journal of Vertebrate Paleontology, v. 32, doi:10.1080/02724634.2013.818546.

Martinez, R.N., Sereno, P.C., Alcober, O.A., Colombi, C.E., Renne, P.R., Montañez, I.P., and Currie, B.S., 2011, A basal dinosaur from the dawn of the dinosaur era in southwestern pangaea: Science, v. 331, doi:10.1126/science.1198467.

Millard, A.R., and Hedges, R.E.M., 1996, A diffusion-adsorption model of uranium uptake by archaeological bone: Geochimica et Cosmochimica Acta, v. 60, doi:10.1016/0016-7037(96)00050-6.

Montano, D., Gasparrini, M., Gerdes, A., Della Porta, G., and Albert, R., 2021, In-situ U-Pb dating of Ries Crater lacustrine carbonates (Miocene, South-West Germany): Implications for continental carbonate chronostratigraphy: Earth and Planetary Science Letters, v. 568, doi:10.1016/j.epsl.2021.117011.

Montano, D., Gasparrini, M., Rohais, S., Albert, R., and Gerdes, A., 2022, Depositional age models in lacustrine systems from zircon and carbonate U-Pb geochronology: Sedimentology, v. 69, doi:10.1111/sed.13000.

Pike, A.W.G., Hedges, R.E.M., and Van Calsteren, P., 2002, U- series dating of bone using the diffusion- adsorption model: Geochimica et Cosmochimica Acta, v. 66, doi:10.1016/S0016-7037(02)00997-3.

Plet, C., Grice, K., Pagès, A., Ruebsam, W., Coolen, M.J.L., and Schwark, L., 2016, Microbially-mediated fossil-bearing carbonate concretions and their significance for palaeoenvironmental reconstructions: A multi-proxy organic and inorganic geochemical appraisal: Chemical Geology, v. 426, doi:10.1016/j.chemgeo.2016.01.026.

Qi, L., Hou, M., Mulder, J.A., Cawood, P.A., Guo, Y., Wu, S., Jiao, L., Zhang, X., and Ouyang, H., 2024, In situ U-Pb dating of Jurassic dinosaur bones from Sichuan Basin, South China: Geology, v. 52, doi:10.1130/G51872.1.

Raff, E.C., Andrews, M.E., Turner, F.R., Toh, E., Nelson, D.E., and Raff, R.A., 2013, Contingent interactions among biofilm-forming bacteria determine preservation or decay in the first steps toward fossilization of marine embryos: Evolution and Development, v. 15, doi:10.1111/ede.12028.

Rasbury, E.T., Piccione, G., Holt, W., and Ward, W.B., 2023, Potential for constraining sequence stratigraphy and cycle stratigraphy with U-Pb dating of carbonates: Earth-Science Reviews, v. 243, doi:10.1016/j.earscirev.2023.104495.

Rasbury, E.T., Present, T.M., Northrup, P., Tappero, R. V., Lanzirotti, A., Cole, J.M., Wooton, K.M., and Hatton, K., 2021, Tools for uranium characterization in carbonate samples: Case studies of natural U-Pb geochronology reference materials: Geochronology, v. 3, doi:10.5194/gchron-3-103-2021.

Renne, P.R., Mundil, R., Balco, G., Min, K., and Ludwig, K.R., 2010, Joint determination of 40K decay constants and 40Ar*/40K for the Fish Canyon sanidine standard, and improved

accuracy for 40Ar/39Ar geochronology: Geochimica et Cosmochimica Acta, v. 74, doi:10.1016/j.gca.2010.06.017.

Roberts, N.M.W., and Holdsworth, R.E., 2022, Timescales of faulting through calcite geochronology: A review: Journal of Structural Geology, v. 158, doi:10.1016/j.jsg.2022.104578.

Roberts, N.M.W., Rasbury, E.T., Parrish, R.R., Smith, C.J., Horstwood, M.S.A., and Condon, D.J., 2017, A calcite reference material for LA-ICP-MS U-Pb geochronology: Geochemistry, Geophysics, Geosystems, v. 18, doi:10.1002/2016GC006784.

Rochín-Bañaga, H., Davis, D.W., and Moysiuk, J., 2024, U–Pb dating of belemnites and rugose corals: The potential for absolute dating of calcitic invertebrate fossils: Chemical Geology, v. 644, doi:10.1016/j.chemgeo.2023.121862.

Rogers, R.R., Swisher, C.C., Sereno, P.C., Monetta, A.M., Forster, C.A., and Martínez, R.N., 1993, The Ischigualasto tetrapod assemblage (Late Triassic, Argentina) and 40Ar/39Ar dating of dinosaur origins: Science, v. 260, doi:10.1126/science.260.5109.794.

Sagemann, J., Bale, S.J., Briggs, D.E.G., and Parkes, R.J., 1999, Controls on the formation of authigenic minerals in association with decaying organic matter: An experimental approach: Geochimica et Cosmochimica Acta, v. 63, doi:10.1016/S0016-7037(99)00087-3.

Tabor, N.J., Montañez, I.P., Kelso, K.A., Currie, B., Shipman, T., and Colombi, C., 2006, A Late Triassic soil catena: Landscape and climate controls on paleosol morphology and chemistry across the Carnian-age Ischigualasto-Villa Union basin, northwestern Argentina: Special Paper of the Geological Society of America, v. 416, doi:10.1130/2006.2416(02).

Vermeesch, P., McLean, N., Vaks, A., Golan, T., Breitenbach, S.F.M., and Parris, R., 2025, Broken 206P /238U carbonate chronometers and 207Pb/235U fixes: EGUsphere, v. 2025, p. 1–22, doi:10.5194/egusphere-2025-432.

Vermeesch, P., 2018, IsoplotR: A free and open toolbox for geochronology: Geoscience Frontiers, v. 9, doi:10.1016/j.gsf.2018.04.001.

Wright, V.P., and Tucker, M., 1991, Calcretes: An Introduction: Calcretes, v. 2, p. 1–22, doi:10.1002/9781444304497.ch.

Supplementary Material

Publication	Aguirre-Palafox et al. 2025, in prep
Laboratory & Sample Preparation	
Laboratory name	The University of Kansas, Isotope Geochemistry Laboratories
Sample type/mineral	calcite
Sample preparation	polished thick sections and round epoxy mounts
Imaging	reflected, transmitted light
Laser ablation system	
Make, Model & type	Arf excimer 193 nm, Photon Machines Analyte G2, Atlex300
Ablation cell & volume	Helex 2, two-volume cell
Laser wavelength (nm)	193
Pulse width (ns)	5
Fluence (J.cm-2)	3.3
Repetition rate (Hz)	11
Spot size (um)	85 µm circle
Carrier gas	He, 1.1 l/min, Ar, 1.4 l/min
Ablation duration (secs)	30
ICP-MS Instrument	
Make, Model & type	Thermo Element2 magnetic sector field ICP-MS
RF power (W)	1350
Make-up gas flow (l/min)	Ar, 1.35 l/min
sampling depth (z position of torch)	4.8
Detection system	single detector, counting
Masses measured	Pb206, Pb207, Pb208, Th232, U238
Integration time per peak (ms)	Pb206, Pb207, U238: 80 ms; Pb208, Th232: 8 ms
Total method time	46
Gas blank (s)	15
IC Dead time (ns)	8
UO+/U+ (%)	0.2
238+/232Th+	0.8
Data Processing	
Reference Material info	NIST 612 (Jochum et al. 2011), DBTL (Hill et all. 2016), CS (Tennyson et al. 2017)
238U/238U	137.88
Data processing package used / Correction for LIEF	IGOR PRO, Iolite 2.5, U-PbGeochron3 for Pb, in-house Excel for U-Pb
Common-Pb correction, composition, uncertainty	none
Quality control / Validation	WC1 (Roberts et al. 2017)

Table S1. LA-ICP-MS methods data used in the U-Pb analyses of the Ischigualasto Formation vertebrate fossil bones.

Supplementary Material References

Hill, C.A., Polyak, V.J., Asmerom, Y., and P. Provencio, P., 2016, Constraints on a Late Cretaceous uplift, denudation, and incision of the Grand Canyon region, southwestern Colorado Plateau, USA, from U-Pb dating of lacustrine limestone: Tectonics, v. 35, doi:10.1002/2016TC004166.

Jochum, K.P. et al., 2011, Determination of reference values for NIST SRM 610-617 glasses following ISO guidelines: Geostandards and Geoanalytical Research, v. 35, doi:10.1111/j.1751-908X.2011.00120.x.

Roberts, N.M.W., Rasbury, E.T., Parrish, R.R., Smith, C.J., Horstwood, M.S.A., and Condon, D.J., 2017, A calcite reference material for LA-ICP-MS U-Pb geochronology: Geochemistry, Geophysics, Geosystems, v. 18, doi:10.1002/2016GC006784.

Tennyson, R., Brahana, V., Polyak, V.J., Potra, A., Covington, M., Asmerom, Y., Terry, J., Pollock, E., and Decker, D.D., 2017, Hypogene Speleogenesis in the Southern Ozark Uplands, Mid-Continental United States, *in* Klimchouk, A., N. Palmer, A., De Waele, J., S. Auler, A., and Audra, P. eds., Hypogene Karst Regions and Caves of the World, Cham, Springer International Publishing, p. 663–676, doi:10.1007/978-3-319-53348-3_43.